The Geology of the southern Warmbad Basin Margin

Tephrostratigraphy, Age, Fossil Record and Sedimentary Environment of Carboniferous-Permian Glacigenic Deposits of the Dwyka Group, Zwartbas, southern Namibia

Die Geologie des südlichen Rand des Warmbad Beckens

Tephrostratigraphie, Alter, Fossilien und Ablagerungsraum der karbon-permischen glazigenen Ablagerungen der Dwyka Gruppe, Zwartbas, südliches Namibia

Diplomarbeit

Markus Geiger

Institut für Geologie
Bayerische Julius-Maximilians-Universität Würzburg
Deutschland/Germany
Juli 2000

Geiger M., 2000. The Geology of the southern Warmbad Basin Margin - Tephrostratigraphy, Age, Fossil Record and Sedimentary Environment of Carboniferous-Permian Glacigenic Deposits of the Dwyka Group, Zwartbas, southern Namibia. Diplomarbeit Thesis, Julius-Maximilians-Universität, Würzburg, 1 map, 45 figures and 6 tables, 79 pp.

Abstract

At Zwartbas, about 10 km west of Vioolsdrif, southern Namibia, the Dwyka succession is composed of tillites and distal fossiliferous dropstone-bearing glacio-marine shales. The completely exposed Dwyka succession is interbedded with thin bentonites, altered distal pyroclastic deposits, which were derived from the magmatic arc at the southern rim of Gondwana. Dropstone-bearing and dropstone-free sequences intercalate with four diamictites, of which the two lowest were certainly recognised as tillites. Four events of deglaciation were proven at Zwartbas and thus consist with correlative deposits in southern Africa.

Numerous fossilised fishes, trace fossils, and plant fragments appear frequently within the lower half of the Dwyka succession whereas trace fossils were principally found in the complete succession. Although the environmental determination is quite problematic, the fossil assemblage rather implies proximal, shallow water conditions with temporary restricted oxygenation. The hinterland was covered with considerable vegetation, which points to a moderate climate. Water salinity determinations based on shale geochemistry rectify contrary palaeontological results and point to rather brackish or non-marine conditions in comparison to present-day salinites.

Geochemical analyses of the bentonites relate the pyroclastic deposits with acid to intermediate source magmas, as they are known from the magmatic arc in present-day Patagonia. Tectono-magmatic comparisons furthermore emphasise a syn-collision or volcanic-arc situation of the magma source. However, significant cyclicity in the production of the pyroclastic deposits was not observed. Radiometric age determinations of two tuff beds clearly date the onset of glacial activity into the Late Carboniferous.

Acknowledgements

I am indebted to a number of people who have contributed to the successful completion of this study with their help, advice and encouragement.

First of all I would like to thank my supervisor Volker Lorenz (Institut für Geologie, Würzburg) for giving me the possibility of carrying out this study and introducing me to the field, and for his support through the work. The guidance, profitable discussion, and advice offered by Berthold Bangert to this study were paramount. Special thanks to him for the introduction to methods and analytics as well as for providing me with geochemical data.

Rainer Klemd and Rosemarie Baur (both Institut für Mineralogie, Würzburg) are appreciated for carrying out X-Ray Fluorescence analyses and their introduction to sample preparation techniques. Klaudia Hradil (Institut für Mineralogie, Würzburg) is thanked for her introduction and help in performing X-Ray Diffractometry at the Institut für Mineralogie, Würzburg. I'm grateful to Michael Schlirf for his help to determine the fossil findings. Special thanks to Frank Holzförster, Doris Maicher, Michael Hautmann, Christine Gans, David Mackintosh and my father for doing the hard job of reviewing the manuscripts of individual chapters of this thesis. I would also like to thank my friends and colleagues Mario Werner, Martin Kinne and Ansgar Wanke for profitable discussions and helpful comments.

My parents are acknowledged for their support in bringing me to the present level of education and for their financial support during the field study. Last but not least I want to mention Carlos Peres, Maecenas and the King of the Orange, who provided board and lodging. Trevallyan Cumming, Malcom Eisele and other river-guides are also thanked for their hospitable company during the fieldwork.

Content

Chapter 1 Introduction

1.1 Geological overview

Widespread deposits of the Late Palaeozoic to Early Jurassic Karoo Supergroup and equivalents occur in many parts of Gondwana: South America, Africa, Antarctica, the Falkland Islands, India and Australia (Visser, 1997). In southern Africa these deposits are mainly preserved in the Main Karoo Basin in South Africa, the Warmbad (or Karasburg) Basin in Namibia and the Aranos (or Kalahari Basins) in Namibia and Botswana (Figure 1, see also Figure 4). The basin development was controlled by the tectonic activity of the Cape Fold Belt at the southern Kalahari Craton margin and eventually influenced by the Southern Trans-African shear system at the northern craton boundary (Visser, 1992), which can be related to the initial break-up of Gondwana and the opening of the southern Atlantic (Stollhofen, 1999). At their maximum extent during the Early Permian, Karoo associated basins covered some 4.5 Mio. km^2 world-wide, of which 300 000 km^2 are still preserved in southern Africa (Smith et al., 1993).

Karoo outcrops in Namibia are more spatially distributed and often inaccessibly covered by post-Karoo deposits. The Warmbad Basin, however, provides well-developed successions. It was probably connected with both the Aranos Basin in the north and the Main Karoo Basin in the south, but became isolated by warping and erosion (Martin, 1981a). Mainly subhorizontal Late Precambrian to Early Cambrian sediments of the Nama Group represent the basin floor and the adjacent elevations (see Figure 2). The oldest sediments in the Karoo aged basins are Late Carboniferous glacigenic deposits of the Dwyka Group, which were derived from a major ice sheet on Gondwana during the migration of the supercontinent over the Carboniferous South Pole. Succeeding marine deposits belong to the Ecca Group. Volcanism at the active plate margins originated interbedded ash-layers, from which reliable chronological information and the capability for a tephrostratigraphy were derived.

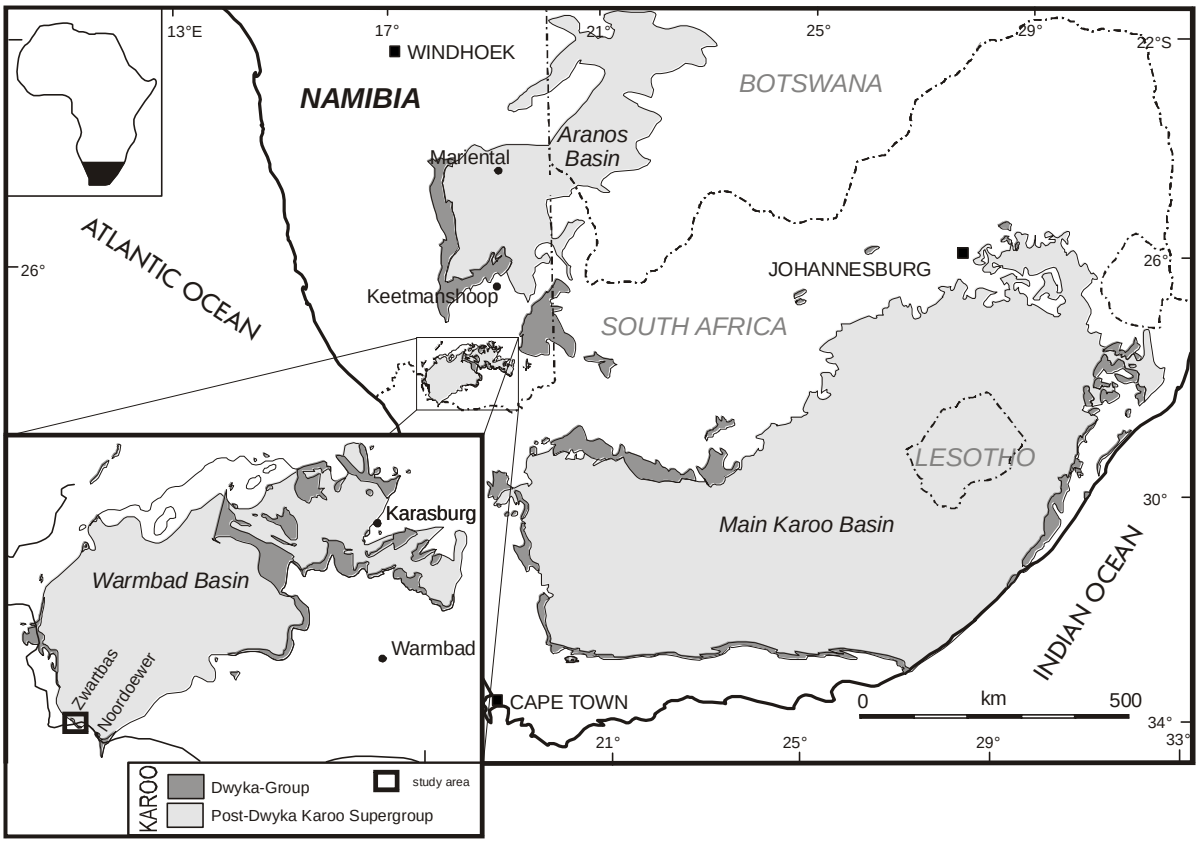

Figure 1: Karoo deposits of the Main Karoo, Warmbad and Aranos Basins are widely exposed in Namiba, Botswana and South Africa. (Compiled from Martin (1981a), Visser (1983a) and Bangert et al. (1998))

1.2 Location of the study area

The settlement and Namibian border post of Noordoewer is located in the Karasburg District (Karas Region), which is the most south-easterly administrative district of Namibia. Situated along the northern banks of the deeply incised Orange River, Noordoewer is tucked away in the surrounding highlands of the Tandjieskoppe Mountains west of the National Road B1. At the opposite side of the river Vioolsdrif acts as the South African border post. The South African territory west of the Orange River is formed by the undulating and mountainous country of the northern Namaqualand south of the mountainous Richtersveld. The study area is located about 10 km west of Noordoewer (Figure 2). The area south of the road D 212 from Noordoewer to Rosh Pinah is private property and belongs to different farms, whereas the area north of the road is state land. This work focuses on an area marked off in the east by E 17° 35.332' and in the west by E 17° 32.263'. The northern boundary comprises the 28° 38.925'th latitude, while the Orange River restricts it to the south. Although the locality name 'Zwartbas' (or 'Swartbas') as used by several authors (e.g. McLachlan and Anderson (1973), Schreuder and Genis (1974) and Pickford (1995)) was adopted from a little village on the South African side of the Orange River, it will also be used henceforth for the nearby locality on the Namibia side.

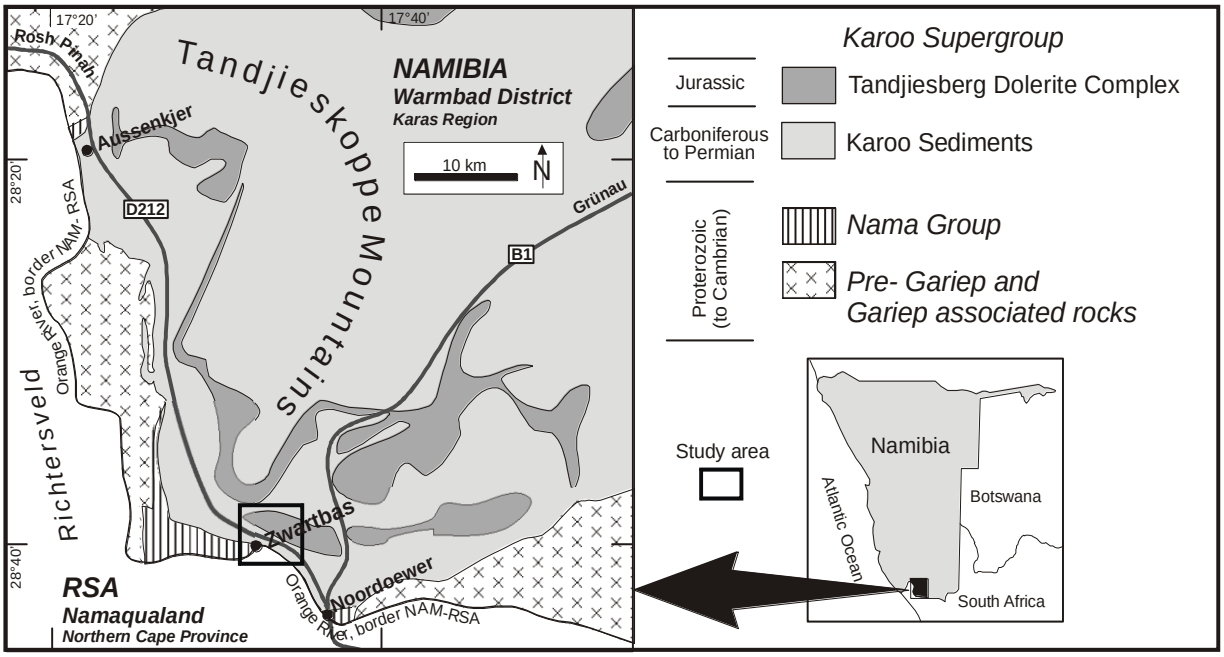

Figure 2: Geographical position of the Zwartbas vicinity and the regional geology (Compiled from Haughton and Frommurze (1936) and Gresse and Scheepers (1993)).

1.3 Previous studies and objectives of this study

The term "Karoo" was first introduced by Bain in 1856 (in SACS, 1980), who described "Reptiliferous series" excluding the basal tillites of the modern Dwyka-Group. In 1867 Jones (in SACS, 1980) included the basal conglomerate in the Ecca beds and 1875 Dunn (in SACS, 1980) introduced the name Dwyka Conglomerate. Only a few years later, in 1888, Schenk (in SACS, 1980) took it out of the Ecca beds again, until in 1903 it constituted a subdivision in Roger's newly established "Karoo System" (Dwyka, Ecca, Beaufort and Stromberg formational subdivisions), which is still in use (in SACS, 1980). In southern Namibia the Karoo has been studied since the beginning of the last century (Haughton and Frommurze, 1928 and 1936). Later studies mainly by Martin and Wilczewsky (1970), McLachlan and Anderson (1973), Schreuder and Genis (1974), Martin (1981a and 1981b), Visser (1983a) and Pickford (1995) concentrated on the glacigenic part, while Kingsley (1985 and 1990) investigated the non-glacial Ecca Group. Recent studies in northern Namibia made an

effort to correlate the strata with the equivalents in South America and South Africa (Ledendecker, 1992). Stollhofen (1999) used the Karoo sediments of Namibia to develop a model of intracontinental rifting on a passive continental margin. Most recent studies of the Dwyka and Ecca Groups in the Huab and Waterberg areas have been carried out by Wanke et al. (2000) and Holzförster et al. (1999). Grill (1997) worked on aspects of sedimentary facies and sequence stratigraphy of the Karoo in the Aranos Basin. Bangert et al. (1998, 1999) used ash-layers to establish a detailed tephrostratigraphy in the Ganigobis Shale Member of the Dwyka Group in the Aranos Basin and juvenile zircons for age determination. Furthermore, he has been working on a correlation of the Ganigobis Shale Member and the basal Dwyka Group at Zwartbas (Bangert et al., 2000).

In this study, a descriptive tephrostratigraphy of the lower Dwyka Group is combined with fossil records and geochemistry in order to compose a comprehensive facies description of the basal Dwyka Group at Zwartbas. Eventually the development of a suitable model for the depositional environment is aspired. Petrographical and geochemical studies of 65 recognised tuff beds allow the discrimination and determination of the ash sources. Additionally radiometric dating of two tuff beds within the succession enables chronostratigraphic classification and correlation with other Carboniferous-Permian basins.

1.4 Fieldwork

This study is based on a combined field work for a diploma mapping project (finished 1999 by this author) and the fieldwork for this diploma thesis. The field work comprised (re)mapping of a 25 km^2 area, logging and sampling. Thereby the *geological map 1:10 000 of the Namibian borderland along the Orange River at Zwartbas* was compiled of which a 1:25 000 b/w reprint is attached to this thesis. The most detailed already existing geological map of this region was published by Haughton and Frommurze (1936): geological sheet Amib (H-33-F) 1:25 000. Grain size grading used for sediment classifications during the fieldwork was based on the size class scale of Wentworth (1922).

Important outcrop locality names were taken from Geiger (1999). GPS coordinates are given in Table 1, the geographical context shows Figure 3.

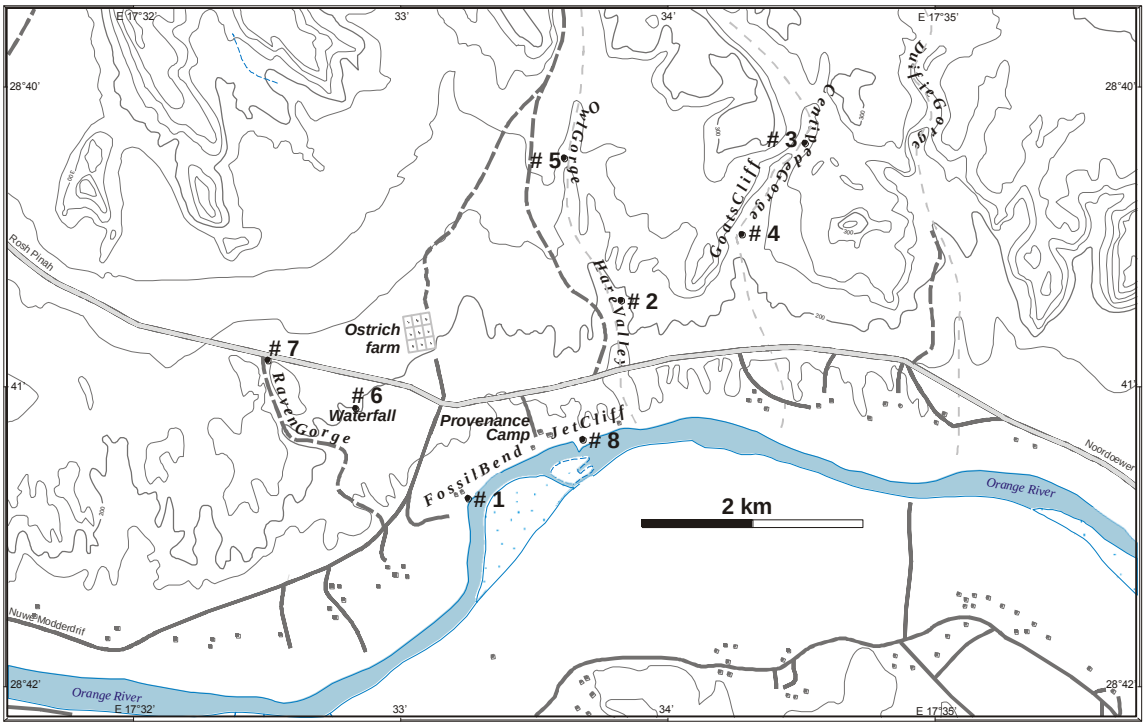

Figure 3: Overview of the outcrop localities. Abbreviations refer to the outcrop ID in Table 1.

Outcrop ID / given names	Description	Coordinates
# 1 Fossil Bend	Banks and cliffs	S 28° 41.432'/E 017° 33.256'
# 2 Center of Hare Valley	River cut	S 28° 40.682'/E 017° 33.763'
# 3 Centipede Gorge	Cliffs of a gorge	S 28° 40.891'/E 017° 34.272'
# 4 Centre of Goats Cliff	Under-cut slope	S 28° 40.490'/E 017° 34.223'
# 5 Owl Gorge	Walls of a dried-up broad gorge	S 28° 39.945'/E 017° 33.574'
# 6 Waterfall	Dried-up waterfall and subsequent river course	S 28° 40.971'/E 017° 32.649'
# 7 Head of Raven Gorge	River bed	S 28° 40.927'/E 017° 32.380'
# 8 Jet Cliff	Cliff and land indentation in the Orange River	S 28° 41.191'/E 017° 33.620'

Table 1: Description and localisation of the investigated outcrops and typical localities. Important localities and their contiguous vicinity, such as extensive walls or cliffs, were designated with particular names.

1.5 Laboratory work

Laboratory studies on bentonites comprise thin-sections, grain mounts of heavy minerals, X-ray diffraction (XRD), X-ray fluorescence (XRF), inductively coupled plasma-mass spectrometry (ICP-MS), spectrum analyses and radiometric dating (SHRIMP).

Thin-section preparations, such as sawing and polishing of rock chips, gravity separation and the production of grain mounts of heavy minerals were performed by the author in the laboratories of the Institut für Geologie of the Universität Würzburg. XRD powder analyses were measured by the author at the Institut für Mineralogie of the Universität Würzburg. XRF measurements of major and trace elements on mudstones and complementary measurements on bentonites were also carried out there. Element concentration determinations of the tuff beds including rare earth elements were carried out at the Institut für Geologie und Dynamik der Lithosphäre of the Universität Göttingen in association with B. Bangert (Dr. rer. nat. student at the Institut für Geologie of the Universität Würzburg). Further co-operations with him provided total organic carbon (TOC) and nitrogen concentration measurements on the mudstones, which were carried out at the Institut für Geologie und Paläontologie of the Universität Tübingen, and radiometric dating of zircons by SHRIMP at the Research School of Earth Science of the Australian National University in Canberra. Explicit preparative and analytical descriptions are listed in Chapter 6.

Chapter 2 Warmbad Basin History and Stratigraphy

The inception of a widespread basin development during Karoo time in southern Gondwana was induced by two major forces. Initial palaeorelief-influenced (glacial) erosion and isostatic depression was commonly continued in intracratonic riftsystems (e.g. Warmbad and Aranos Basin) or, in the case of the Main Karoo Basin, by the formation of an early back-arc/foreland basin.

2.1 The Late Palaeozoic and Early Mesozoic basin development in southern Africa

The Carboniferous to Permian tectonic setting of the Warmbad Basin must be placed in context with the tectonic evolution of western Gondwana. Gondwana supercontinent assembled approximately in the latest Proterozoic and lasted until the Late Palaeozoic, when it became part of Pangea (de Wit and Ransome, 1992). The African segment was dominated by the large Congo and the smaller Kalahari Cratons which were separated by the Damara Mobile Belt in the Late Proterozoic and Early Cambrian (Germs, 1995). A period of erosion followed in the interior of southern Gondwana until the Late Palaeozoic, with some exceptions at its very southern margin. Sedimentation restarted in the (Late) Carboniferous to the Early Jurassic, when several basins of different geometries and time scales and basin floors of Precambrian basement or Mid-Palaeozoic strata formed on the supercontinent (Visser, 1987). During the Late Palaeozoic to the Jurassic a northwest-directed subduction at the Samfrau subduction zone along the palaeo-Pacific margin resulted in the formation of the Gondwana fold belt by north-south shortening associated with transpressive strike-slip (back-arc/foreland) basin development and regional uplift within the interior (Figure 4). In contrast, basin formation in the interior was controlled partly by reactivated mega-shear systems (Daly et al., 1989) with extensional strike-slip basin development (Ring, 1995). Discontinuous spreading along the rift axis was compensated by large transform faults forming transpressive ridges which separated former contiguous sedimentary environments. The Karasburg Ridge for instance could have divided the Warmbad from the Aranos Basin. Isostatic depression due to the ice load during the Carboniferous to Permian glaciation was probably an optional initial force for the formation of depositories especially along the coast (Crowell and Frakes, 1972).

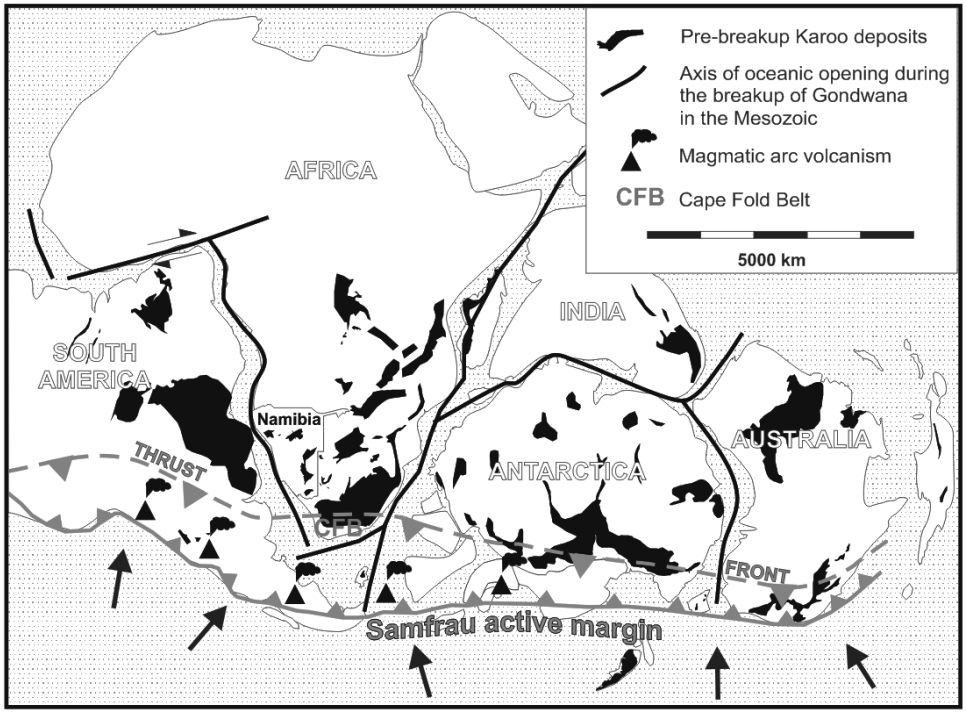

Figure 4: Gondwana in the Late Palaeozoic was tectonically controlled by the Samfrau subduction zone at its very southern margin. Arc volcanism and foreland tectonism resulted from an oblique subducting Palaeopacific plate. Preserved outcrops of Early-Karoo deposits show a Gondwana-wide distribution. (from Stollhofen (1999))

2.2 Warmbad Basin evolution - initial Karoo basin development in southwestern Africa

The palaeogeography of the preglacial landscape at the end of the Carboniferous consisted of an extensive continental highland surrounded by mountainous regions along the Namibian coast and in the northern half of South Africa. River systems dissected this upland called Cargonian Highland (name derived from ***Car***boniferous and ***Gon***dwan***ian***) and drained to the south and west. At the western slopes of the highland the drainage was probably caught by a shallow linear marine seaway, which occupied a drowned failed rift on the western craton margin (Visser and Praekelt, 1996). Today any evidence for its existence and extent is missing, but it is implied by palaeo-slope and palaeo-ice flow directions. Crowell and Frakes (1972) furthermore stated the necessity of open water to provide the moisture for the growth of the ice sheet. Beside this, a marine incursion between the Palaeo-Pacific Ocean and Namibia is required to account for marine fossils in the Aranos and Warmbad Basin (Martin and Wilczewsky, 1970; McLachlan and Anderson, 1973; Pickford, 1995). The same fossils in Argentina and corresponding glacial marks emphasise this assumption (Santos et al., 1996). The southern rim of the highland was a steep escarpment with walls standing 500 m above the sea level (Crowell and Frakes, 1972). In this time a 3000 m thick ice cover expanded from the major ice spreading centre in the continental interior with a main ice flow direction towards the west. Off the west coast of southern Africa the marine sea arm acted as a sediment trap. Sea level rises and isostatic depression due to an increased ice sheet as well as sediment load resulted in expanding shorelines and inundation, while the depocentre became distal. Thus the initial 'Proto-Warmbad Basin' rather represented a large erosional structure with a broadening inlet towards the 'ocean' in the south-west, than a tectonically subsided basin. Glacial erosion on the highland rim may have overdeepened the depository ('Proto-Warmbad Basin') to more than 1000 m (Crowell and Frakes, 1972). By deglaciation in the Early Permian the Aranos and 'Proto-Warmbad Basin' were inundated and became subject to tectonically controlled basin depression. The present-day basin geometry, where the depocentre lies at the west-southwestern margin of the preserved Karoo outcrop (Schreuder and Genis, 1974) and the sediment cover wedges out to the east-southeast, comports with the presumed basin structure of the depocentre progressively subsiding towards the seaway in the west. From when and to what extent tectonic activity was responsible for the basin formation has not been studied sufficiently yet, but the preserved structural pattern may be related to older fault patterns. The NNW-SSE to NW-SE striking structural boundary between Noordoewer and Zwartbas along the Orange River, which separates Karoo rocks at the northern shore from Nama rocks at the southern shore and structural investigations on Pre-Karoo rocks at Zwartbas (Geiger, 1999), suggest the influence of the older anisotropies. A possible connection may be to the WSW-ENE trending Karasburg-Orange fault zone (Karasburg Ridge), which propagates from the offshore Salado-Orange Transform (Stollhofen, 1999; Dingle and Scrutton, 1974) to the ENE. The fault pattern for southern Namibia published by Visser (1983a, Figure 1), however, largely coincides with anisotropies associated with the Gariep Mobile Belt (Daly et al., 1989; Gresse and Germs, 1993), and thus also implies reactivated Proterozoic structures.

The formation of these Carboniferous-Permian to Jurassic depositories is recorded in several parts of Gondwana by sediments of the Karoo Supergroup. Although in most of the basins, which were active during the Karoo time, deposition started with glacigenic deposits of the Dwyka Group, the age and thus the onset of the deposition of Karoo strata is not clear. Palynological studies from the northern Main Karoo Basin (Anderson, 1977) suggested a Late Carboniferous to Early Permian age and were confirmed by marine macrofossil studies by McLachlan and Anderson (1973). Von Brunn and Stratten (1981) noted that in the northern Main Karoo Basin, where most palynological studies were carried out, the sediment thickness is generally reduced, implying that the earliest sediments were eroded during succeeding ice advances. They thus assume, supported by biostratigraphic constraints from Dwyka-equivalent fossil plants, that an initial deposition already commenced in the Early Carboniferous. The period of glacial deposition in southern Namibia was supposed to last from

Late Carboniferous to Early Permian (Martin and Wilczewsky, 1970). Recently determined radiometric ages from ash-fall tuffs in the southern Namibian Aranos Basin (Tses area) confirmed the Late Carboniferous onset of Dwyka deposition with ages of about 300 Ma BP (Bangert et al., 1999).

2.3 Palaeoice flow trends

Directions of Late Palaeozoic ice flow in southern Africa are frequently recorded by glacial striae and grooves on ice-polished floors, boulder pavements, boulder lithology and the trend of glacial valleys. Lithological comparison of the diamictite clasts indicate, that the ice centre lay in the northern Transvaal, Zimbabwe, Zambia and Mozambique (Crowell and Frakes, 1972; Visser, 1983a and 1983b). Considerations on ice-scour trends are especially made at the former ice sheet margins in the periphery of the Dwyka outcrops, where glacial floors are found, which were probably obtained by the first or at least second glaciation of a total sequence of four deglaciation sequences (see Chapter 3.4). Although the directional evidence of most of them is excellent, the generalisation to major ice flow trends resulted in contrary points of view. While Crowell and Frakes (1972) attributed the N-S trending glacial marks on the pre-glacial floor to a southward movement of the ice at the present-day south-west African coast, Visser (1987 and 1997) assumes a general westward movement. Stollhofen et al. (2000) ascribes the southward redirection of the westward advancing ice lobes with an eastward inclining rift shoulder, which flanked the Early Dwyka abortive rift (Chapter 2.2). Similar but opposite orientated (east- to southeastward) ice flow directions were observed on the western side of the rift depression in South America (Santos et al., 1996). Moreover in southern Namibia and South Africa, southward ice flows are attested on the western Karoo outcrop margins, whereas Karoo deposits pinch out farther west. Since only glacial pavements and basal glacigenic deposits are preserved towards the west, deposition took place later on (Visser, 1983a), but sediments were subsequently removed again by a subsequent relative rise of the craton margin. A connection to the ocean in the west, however, is demanded by the marine fossil record (Chapter 5).

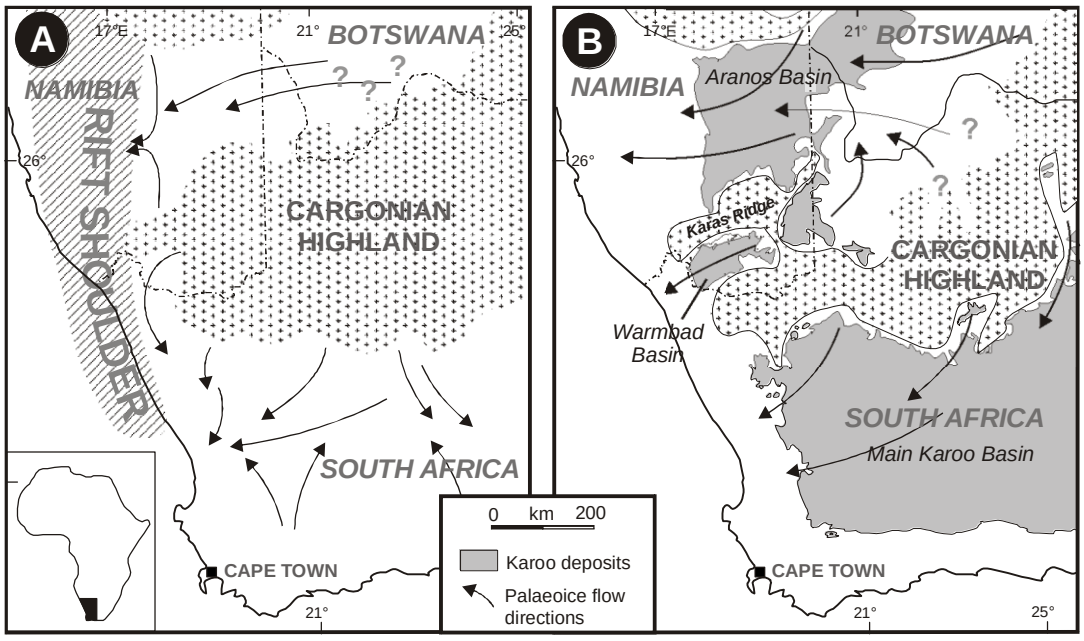

Figure 5: Palaeoice flow directions and uplands during the early Karoo glaciation. (A) Westward palaeoice flows are controlled by a rift shoulder uplift due to the initial South Atlantic rift activity at the very beginning of the glaciation. (B) Palaeoice flow directions, uplands and the distribution of present-day Karoo deposits (compiled from Bangert et al. (1998), Crowell and Frakes (1972), Veevers et al. (1994) and Visser (1983a)).

2.4 Stratigraphy of the Warmbad Basin

The basin floor of the Warmbad Basin is underlain by Late Precambrian and Cambrian sediments of the Nama Group (Martin, 1981a) and possibly older rocks (Geiger, 1999). The floor surface was commonly formed by a glacial abrasion surface, which documents a period of glacial erosion. This erosional event completed a period of erosion and non-deposition, which produced a hiatus from at least the Late Proterozoic to the Late Carboniferous. Grooves and scars have N-S trend and indicate the palaeoice flow. During the Late Carboniferous to probably Late Permian the basin was filled with glacial, glacio-marine and marine deposits of the Dwyka Group and the Prince Albert Formation, the Whitehill Formation, the Aussenkjer Formation and the Amibberg Formation of the Ecca Group. The stratigraphic position of the latter two formations is not yet sufficiently understood.

Overlying Karoo deposits of the Warmbad Basin have only been poorly investigated previously. The pioneers (Haughton and Frommurze, 1928 and 1936) introduced the Dwyka Series with Dwyka Tillite and the Dwyka Shale and the Ecca Series. Schreuder and Genis (1974) adopted this stratigraphy and, although the succession of Warmbad Basin was completed with the Aussenkjer Shale Formation and the overlying Amibberg Formation at its top (SACS, 1980), Martin (1981a) still described the formerly applied stratigraphy. Miller (1992) correlates the Aussenkjer and Amibberg Formation with the Fort Brown and Waterford Formation in the Main Karoo Basin, but Veevers et al. (1994) introduced their correlation with the Collingham and Ripon Formation. Smith et al. (1993) also correlated the Aussenkjer Formation with the Collingham Formation, but equated the Amibberg Formation to both Fort Brown and Waterford Formation. Moreover, he considered the Amibberg Formation to reach into the Beaufort Group. Another optional correlation of Johnson et al. (1996) puts the Aussenkjer and Amibberg Formations at the same stratigraphic position as the Tierberg and the Waterford Formation respectively. Figure 6 depicts a generalised profile of the Warmbad Basin with attributions to different time scales and recent correlative assignments. Although all these attributions describe variable formation names, their stratigraphic position is always the same.

Chronostratigraphic investigations provide an up-to-date chronological correlation. Radiometric ages from the Dwyka Group at Zwartbas (Chapter 9) and correlatives of the Prince Albert Formation (Bangert et al., 1999) and the Collingham Formation (de Wit, cited in Turner (1999)) in the Main Karoo Basin of South Africa provide a suitable subdivision (see Figure 6). With the age of 265±2.5 Ma from the Gai-As Formation in northern Namibia (Holzförster and Stollhofen, 2000), which correlates to the Abrahamskraal Formation, overlying the Waterford Formation in the Main Karoo Basin, the Amibberg Formation as the probable correlative to the Waterford Formation has to be considered younger than this age. Thus the known Karoo succession in the Warmbad Basin is constrained to a time from the Late Kasimov to the Capitanian or even younger, when referring to the time scale of Menning (1997) and Menning and Jin (1998).

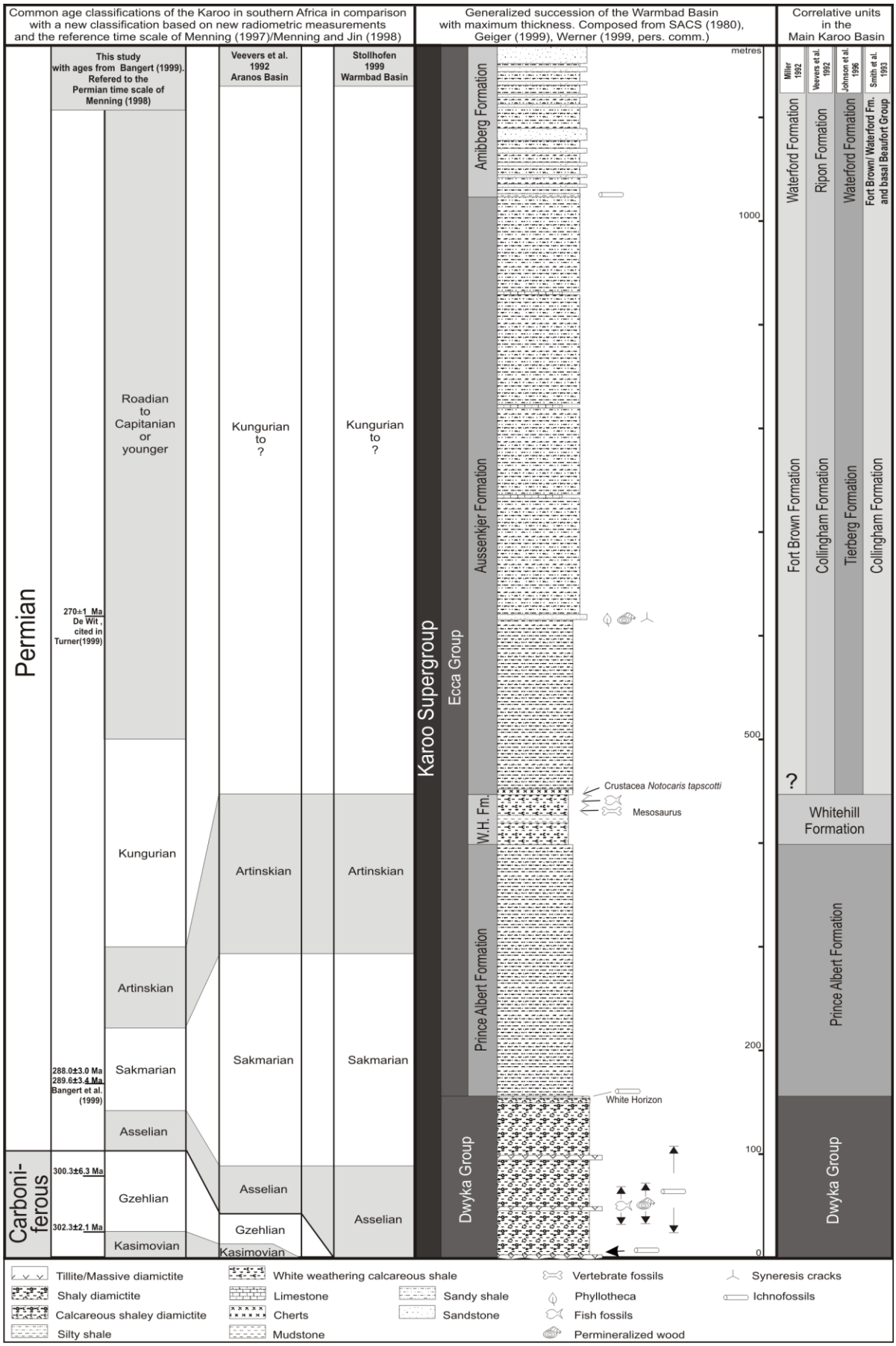

Figure 6: Profile of the Karoo succession in the Warmbad Basin. Comparison of earlier chronostratigraphic classifications are revised with new age determinations on zircons (left columns). Differing correlation results are given in the right columns.

Chapter 3 Lithostratigraphic Description of the Dwyka Group at Zwartbas

At Zwartbas Dwyka deposits rest on a clear unconformity, a glacial floor, which separates the folded Nama rocks (Vendian) or Gariep associated rocks with a hiatus nearly throughout the entire Palaeozoic from the overlying even-bedded to slightly N-NE dipping Carboniferous-Permian Karoo deposits. There the Karoo starts with a 145 m thick Dwyka succession of glacio-marine shales intercalated with diamictite layers and 65 distinct ash-fall derived bentonite beds, which will be treated in detail in Chapter 4. In the following, a brief facies description is given. Detailed petrographical information about the shale is provided in Chapter 7 and about the tuff beds in Chapter 8.

3.1 Facies associations forming the Dwyka Group at Zwartbas

Three major facies associations compose the Dwyka Group at Zwartbas (Figure 8): (1) Massive diamictites with a marly matrix and diverse clasts, interpreted as tillites, represent a subglacial facies association. (2) Dropstone-bearing shales inferring a glacio-marine respectively glacio-limnic environment along with cross-bedded channel-fill sandstones suggesting a fluvio-glacial environment was subsumed in the proglacial facies association. Eventually, (3) a dropstone-free shale constitutes an interglacial-marine facies association.

3.1.1 Subglacial facies association

The subglacial facies association comprises a glacial floor which is mainly overlain by at least one, but probably two tillites. Sometimes the existence of a second tillite was presumed, though two overlying tillites were never observed. At the head of the rapids at Jet Cliff (# 8; for locality information see Table 1 and Figure 3) dropstone-bearing shales were found to be interbedded between the glacial floor and the tillite. This implies that between the scouring of the bedrock and the deposition of the tillite the deposition of argillaceous material was enabled. An explanation gives a temporary retreat or up-float of the ice at a dynamic ice margin on a highly undulating palaeorelief (Geiger, 1999).

3.1.1.1 The glacial floor

The onset of Dwyka deposition in the Late Carboniferous was preceded by at least one event of glacial erosion which left a scratched, striated and polished pavement, predominantly of Nama rocks or Gariep associated rocks (e.g. at Fossil Bend, # 1 and on the plain north of Waterfall, # 7). In consistence with Haughton and Frommurze (1936) and Martin and Wilczewsky (1970), N-S striking striations and grooves devoid of exact polarity determinations were reported by Geiger (1999), who estimated a southward inclining palaeorelief from sedimentary features of a fluvio-glacial sandstone, which infer a corresponding palaeodrainage direction.

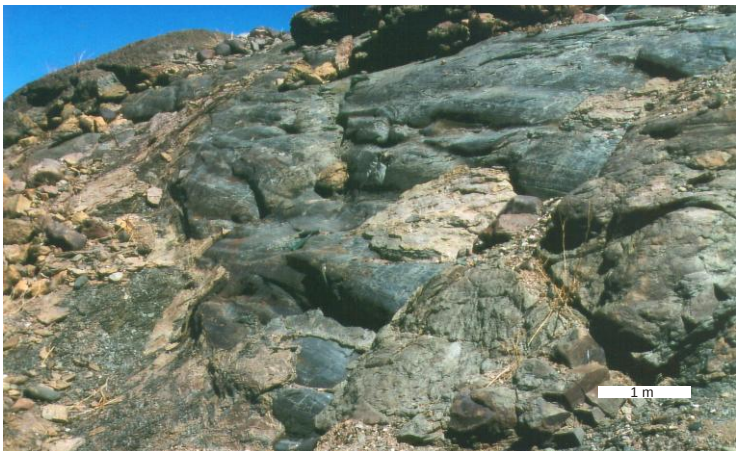

Figure 7: Scoured Pre-Karoo rocks (quarzite) are overlain patchily by Dwyka tillite (Fossil Bend, # 1). Tillite patches are indicated by pointers and confined by the dashed line.

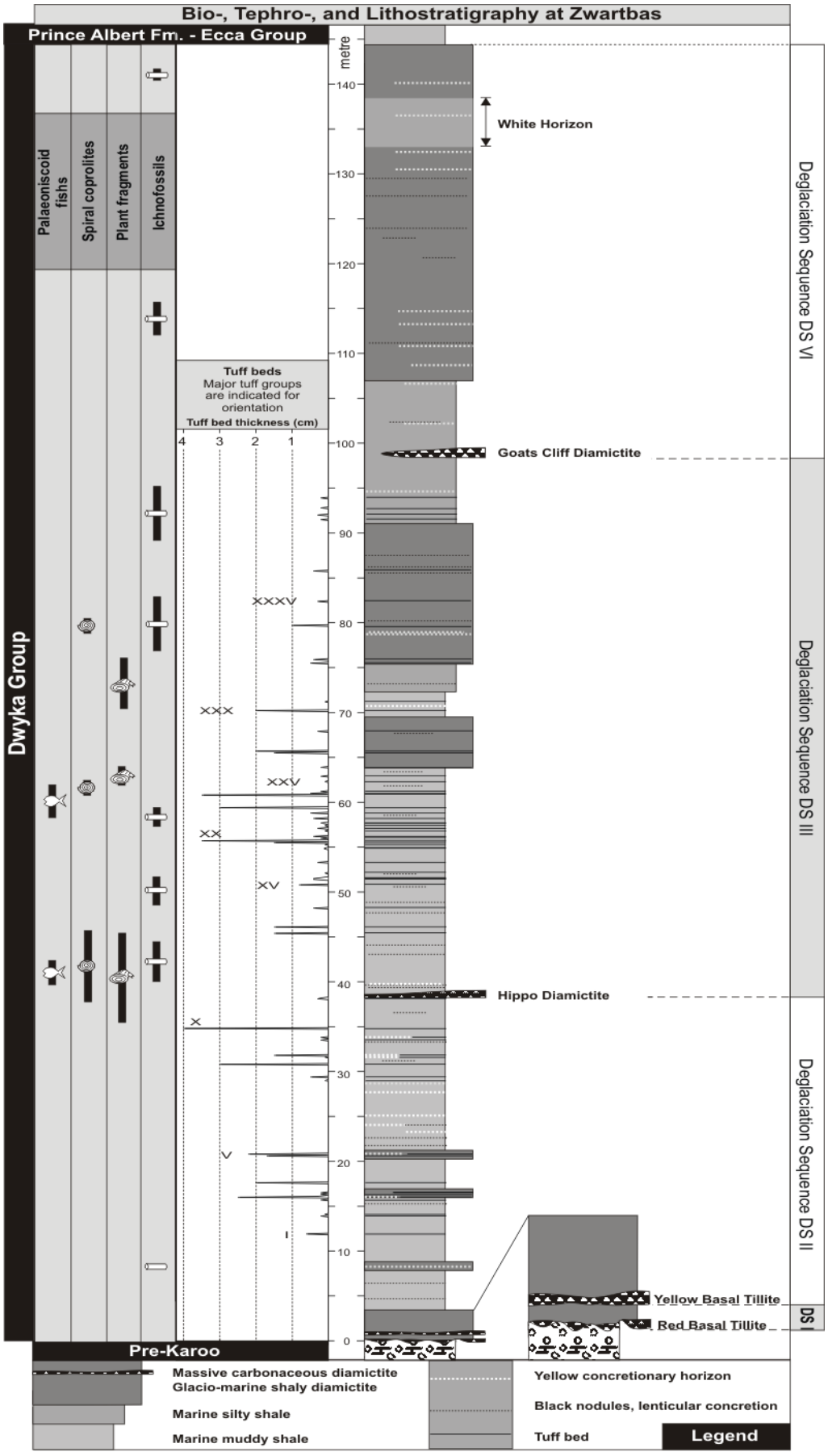

Figure 8: Profile of the glacio-marine basal Dwyka deposits at Zwartbas. Within a distinct lithofacies several biostratigraphic horizons and 65 individual ash-fall tuff beds (thickness spectrum) were recognised. Overall, four coarsening upward sequences reflect the four deglaciation sequences of southern Africa (Theron and Blignault, 1975).

3.1.1.2 Massive marly diamictite facies

At the very base of the succession, just above the glacial striated and polished basin floor, often a tillite veneer was found, which was distinguished into two types. Although they hardly differ in the lithofacies, they do in colour and stratigraphic position. The lower Red Basal Tillite (Head of Raven Gorge, # 7), up to 20 cm thick, appears red and is only sparsely preserved. The stratigraphicallly higher Yellow Basal Tillite (Figure 9B) appears yellow-ocher in colour and drapes the glacial floor as a several centimetres thick veneer (e.g. at Fossil Bend, # 1 and on the plain north of Waterfall, # 7). Generally, the tillites are matrix supported marlstones with subrounded clasts commonly 1 to 5 cm, sometimes up to 10 cm large and predominantly consisting of gneiss, granite, pegmatite, schist, quartzite and sporadically carbonate, chert and jasper. Striations on the top surface of the Red Basal Tillite (Figure 9A) suggest that a subsequent ice advance, which perhaps relates to the deposition of the Yellow Basal Tillite, overrode the Red Basal Tillite. The stacking of the two tillites can be explained by repetative ice advances and thus a migration of the buoyancy line (Heinrich, 1991). Temporarily, glaciomarine sedimentation below the floating ice shelf produced the shaly diamictite between the two tillites (lodgement tills). Frequently associated are intraformational erosional surfaces.

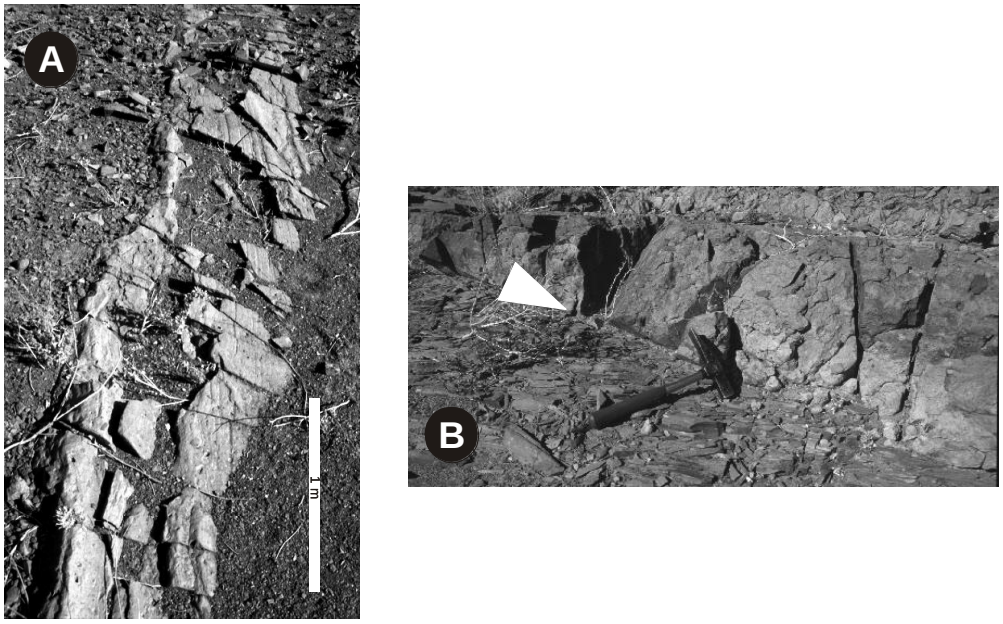

Figure 9: The basal Dwyka tillites at Zwartbas. (A) The lower Red Basal Tillite with scours and striae on its top surface (Head of Raven Gorge, # 7). (B) Lower Yellow Basal Tillite overlies a quarzitic Pre-Karoo bedrock (150 m SSE of Waterfall, # 6). The white pointer indicates the erosional contact. See hammer for scale.

In the overlying shale succession two other diamictites appear. About 40 m above the basin floor a (1) massive, 35 to 80 cm thick, brownish-grey diamictite, the Hippo Diamictite, with a high carbonate content interrupts the shaly succession (e.g. Fossil Bend, # 1). Abundant angular clasts ranging characteristically from 10 to 20 cm in diameter may suggest an interpretation as tillite, but certain sedimentary clues are lacking. (2) Another convolute bedded marly diamictite, the Goats Cliff Diamictite (Figure 10A), which turns up about 100 m above the base of the Dwyka Group, is convolute bedded, blueish-grey in colour, and resembles rather the appearance of the basal tillites (Centre of Goats Cliff, # 4). The clasts are mainly 4 to 6 cm in diameter and less abundant than in the other massive diamictites.

3.1.2 Proglacial facies association

According to Geiger (1999) the proglacial facies association shows two entirely different depositional environments by their opposing lithofacies. Whereas (1) a trough cross-bedded sandstone lens, maximum 65 cm thick and laterally some metres wide, was interpreted as subaerial fluvio-glacial tunnel mouth deposit, the approximately 150 m thick (2) shaly diamictite and shale facies was deposited in a glacio-marine environment, whose location became successively more distal.

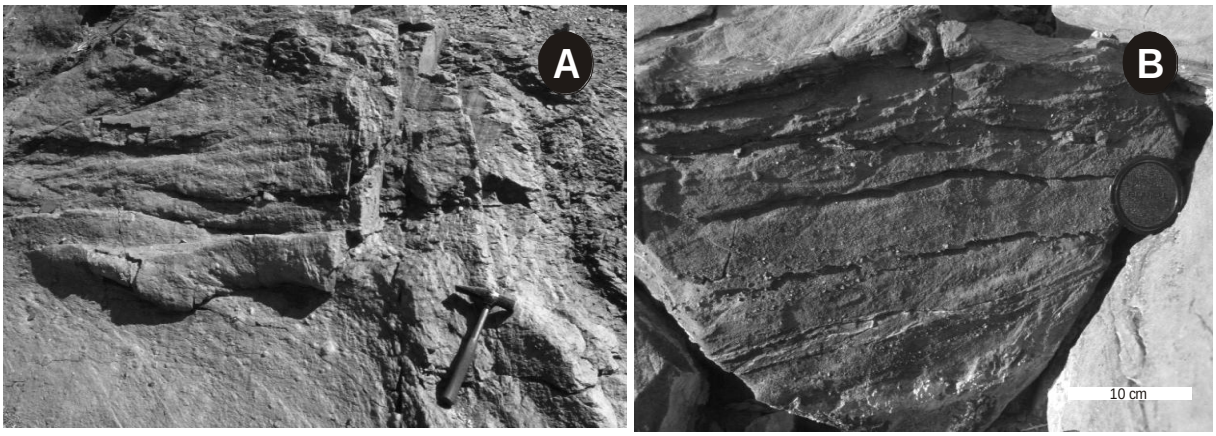

Figure 10: (A) View on the top surface of the Goats Cliff Diamictite, a massive convolute bedded marly diamictite (Centre of goats Cliff, # 4). See hammer for scale (B) Fluvio-glacial channel sandstone indicates sub- or proglacial drainage (Head of Raven Gorge, # 7).

3.1.2.1 Fluvio-glacial trough cross-bedded gravelly sandstone facies

An isolated channel sandstone with a preserved lateral extend of only about 20 m at the head of Raven Gorge, # 7 comprises a red moderately sorted, normal graded and grain-supported fine- to medium-grained sandstone with a red clay matrix. The preserved thickness of the sandstone lens is up to 65 cm and the lateral extent approximates 10 m. Sporadically sub-angular to sub-rounded quartzite and carbonate lithoclasts, normally 1 to 10 cm, sometimes up to 50 cm, float within the sandstone and are predominantly aligned along the bedding planes (Figure 10B). Trough cross-beds of the sandstone as well as the orientation and inclination of the palaeovalley, which is occupied by the sandstone, shows a palaeodrainage towards the south. The occurrence of the sandstone is associated with the Red Basal Tillite, whereas the tillite may also occur solely but not vice versa. Geiger (1999) considered the common occurrence of the red oxidation colour in both the sandstone and the Red Basal Tillite as well as the situation of these facies types on a palaeorelief high as evidence for subaerial deposition. Such glacial sandstones are typical for the proximal outwash fan at an ice margin (Heinrich, 1991).

3.1.2.2 Glacio-marine shaly diamictite and marine shale facies

The deposition of a dropstone-bearing black shale (cf. Chapter 7.4.1) generally commenced after the deposition of the subglacial tillite. The shale facies can be distinguished from the shaly diamictitic layers by the presence of dropstone. Since the finding of dropstones is accidental, shales apparently devoid of dropstones may be wrongly classified as marine shale. Together in turn both facies build up a sequence of dropstone-bearing and dropstone-free shale layers representing glacial, transitional and interglacial periods (Heinrich, 1991). Heinrich (1991) relates fine grained clastic sediments and diamictites to the distal outwash fan of an ice margin.

Between 80 to 95 m from the base, several up to 20 cm thick layers with 1 to 2 cm large angular clasts of reworked mudstone occur, while the shale is frequently coarsening to silt grain size. Laminated diamictite layers at the base and at the top of the succession imply a sedimentation rate of about 5 mm post-diagenetic per year. Laminated diamictites are characteristically found within 0.5 to

1 km of the grounding line and indicate a proximal situation to the ice margin, particularly along with subglacial sandstones (Heinrich, 1991). Wetzel (1991) outlines that sequences of laminae document short-term variations within a black shale environment and are usually preserved due to low oxygen levels, preventing bioturbation.

Dropstones comprise quartzite, vein quartz, granites, gneiss, volcanic rock and carbonate and usually range from 3 to 8 cm in diameter but larger clasts, exceeding 1.5 m across, concentrate between 75 and 80 m above the Dwyka base, on the plain east of Hare Valley, # 2.

3.2 Concretions

Several types of concretions and concretionary beds and horizons are displayed in the shale succession. Oval *black nodules* and sinuously rounded and laterally connected *lenticular concretions* with irregular swelling and pinching, occasionally fossil-bearing, are frequently found. The nodules occur either isolated or are enriched in distinct horizons. Their size varies from 5 to 20 cm in horizontal diameter and from 10 to 40 cm vertically. Largely similar but more pervasive bodies of black concretions are locally up to 30 cm thick and extend laterally over several metres. McLachlan and Anderson (1973) explain the origin of such black nodules under calcium carbonate saturated conditions by the precipitation of carbonate - induced by pH-decrease - around a nucleus, preferentially a fossil fragment. Bangert et al. (2000) noted the participation of phosphate. Ricken and Eder (1991) give further considerations on nodule formation. They note that nodule formation by concretionary cementation through calcite, ankerite, siderite, or dolomite takes place in sediments with a dominant proportion of the non-carbonate material but organic carbon enrichment. Consequently they are mainly found in shales, black shales and marls, where the decay of organic matter promotes carbonate precipitation. Apart from high organic carbon content in the former sediment, intense sulphate reduction, closely tied to anoxic and epiclastic events, is important for the formation of the concretions. Stratiform horizons indicate the breakdown of large quantities of organic matter (anoxic events) related to rapid sulphate reduction. Succeeding methane production can lead to localised carbonate precipitation in the sediment, because both processes are associated with the release of HCO_3^- in the pore waters. Moreover, from the shape of nodules the diagenetic history can be concluded (Ricken and Eder, 1991). Oval shapes with almost equidistant diameter indicate near-surface burial, while shallow burial results in smaller concretions with horizontal elongation due to compaction caused by overburden. Since in Zwartbas both types coincide close together, near-surface to shallow burial has probably taken place.

Additionally, *ocher laterally persistent concretionary layers* up to 60 cm in thickness are spread across the shales. Often they show a typical brownish ferric weathering colour. Since they sometimes pass into tuff beds, it is possible that they have developed from altered ash layers. Cone-in-cone structures and XRD measurements point to an almost pure $CaCO_3$ content. Increased growth of calcareous plankton in interglacial periods may have provided the carbonate (Heinrich, 1991). Eventually a porous *dark brown crust* either covers yellow concretions or forms concretionary interlayers in highly weathered tuff beds. These crusts occasionally show fibrous structures possibly of gypsum.

3.3 The Dwyka-Ecca boundary

With the definition of the Dwyka-Ecca boundary as the transition of a glacial facies into a non-glacial facies (SACS, 1980), this boundary is generally considered to have a diffuse and diachronic character. Concerning this, it is very difficult to determine an exact regional differentiation criterion, but in marine and limnic environments the presence of dropstones is a suitable criterion, though they appear only sporadically. At Zwartbas, at the southern rim of the Warmbad Basin, this theoretical boundary can be correlated with an 11 m thick marker horizon of three subsequent white-weathering

shale layers, the White Horizon (Centipede Gorge, # 3 and Owl Gorge, # 5), which lies just below the Dwyka-Ecca boundary (Geiger, 1999). Its relevance for interbasinal correlation is apparent on aerial photographs, where the horizon can be traced over several kilometres. From the Lainsburg area Visser (1991) reports of an equivalent approximately 10 m thick horizon, the Pseudo White Band, which he classified there as the very base of the Ecca Group. Thus this white weathering shale seems to provide a useful interbasinal correlation horizon for the approximate Dwyka-Ecca boundary. Significantly, the nodules, concretions and concretionary horizons suspiciously diminish at this boundary. Thus it can be related to a ceasing input of terrestrial carbonate, whilst the glacial erosion died (Geiger, 1999).

3.4 Deglaciation sequences – principle framework in southern Namibia and facies correlation

Deglaciation events by means of ice margin fluctuations commonly produce an enormous sediment discharge due to excessive iceberg drifts as well as increased fluvio-glacial discharge. Typically, a sharp boundary overlain by a sequence of massive diamictites (tillites), debris rain-out diamictites and shales, sometimes along with sediment-gravity flows and fluvio-glacial outwash built up one deglaciation cycle. Theron and Blignault (1975) first discovered the cyclic facies change, which subdivides the glacial Dwyka Group into four deglaciation sequences: DS I-IV (Visser, 1997). Cyclic facies changes in the Aranos Basin (Namibia) enabled an effectual interbasinal correlation with the Main Karoo Basin in South Africa (Bangert et al., 1999 and 2000; Stollhofen et al., 2000).

Taking into account the observations of Visser (1997) and Bangert et al. (2000), at Zwartbas DS I and II seem to be preserved in the two basal tillites (Figure 8). The condensed stacking of the basal massive diamictites of DS I and II was also observed by Bangert et al. (1999) in correlative strata in the Aranos Basin. Trying to subdivide the overlying succession in accordance with the four-cycle model, the two massive diamictites, the Hippo and the Goats Cliff Diamictite, offer the most likely clues. Considering the observations of Heinrich (1991) on recent ice shelf margins in the North Atlantic, the upper two diamictites, the Hippo and the Goats Cliff Diamictite, along with the adjacent shales devoid of ice rafted debris, can be related to glacial periods with stable ice margins. Conclusively DS III and DS IV were considered to begin with the Hippo Diamictite and the Goats Cliff Diamictite respectively.

Moreover, the schematic model of deglaciation sequences caused by sea-level fluctuations of Visser (1997) and a temporal classification therewith infers that the dated tuff beds with ages of about 302 and 300 Ma BP rather belong to DS II. This is still true, although Bangert et al. (1999) revised the time frame of Visser's model.

Chapter 4 Bentonites – altered pyroclastic deposits

Volcanic eruptions are daily events since the formation of earth. Almost every depositional system contains volcaniclastic interlayers or at least some reworked pyroclastic components (Einsele, 1992). Now and then volcanoes produce successive deposits of fall-derived material, so called pyroclastic deposits (Schmid, 1981), which were formed by some process of fragmentation, then became widely dispersed by different kinds of transportation and finally deposited in almost every environment. In geological terms, their contemporaneous deposition over extensive areas makes pyroclastic rocks excellent isochronous, datable markers of individual eruptions or eruption phases. The sheet-like distribution with an extent partly up to some thousand kilometres from their source has stratigraphic significance for correlation. Petrographical differences between volcaniclastic and siliciclastic deposits support explicit recognition and discrimination. Layers of pyroclastic deposits are the only sediments that can form in marine and terrestrial environment and can thus provide stratigraphic markers on a very large regional scale (Schmincke and Bogaard, 1991). Bentonites are very useful to support and verify correlation aspects obtained from stratigraphic, palaeontological, palaeomagnetic, radiometric, petrographical and geochemical data.

4.1 Distribution and deposition of ash fall layers

Explosive volcanic (plinian) eruptions produce pyroclastic material with a wide range in grain size, but only the fine-grained proportion may disperse laterally over large areas by wind drift. The continuity in production and dispersal results in fall-out deposits with spatial persistence, relatively constant thickness over large areas, comparatively high sedimentation rates and a primary distribution covering various landscapes independent of the environmental setting (Königer, 1999). Dispersal distance and sedimentation rate depend on the eruption type of the volcano and climatic variables (Fischer and Schmincke, 1984).

Facies changes are recognised on grain-size and deposition type changes. Whereas the proximal facies is dominated by coarse-grained ballistic fallout and pyroclastic flow deposits within a few km from the vent, the medial facies comprises flow and fallout deposits of ash to lapilli grain size interbedded with siliciclastic units. The distal facies far away from the vent fallout deposits consists of fine-ash to sub-micron size ash.

In respect of facies changes the aeolian fractionation constitutes an important aspect of distal fallout deposits. Downwind of a vent ash clouds change their chemical and mineralogical composition. Fischer and Schmincke (1984) considered three factors to be significant for aeolian fractionation: (1) magma chamber variables, (2) eruption column variables and (3) transfer system variables. An independent but highly interfering variable is an additional primary compositional zonation within the magma chamber, which leads to succesive compositionally heterogeneous deposits. Dynamic processes within the eruption column may also have an influence. Within the drifting ash cloud, fractionation is realised by different settling velocities of particles diverse in density and shape. Denser crystals like heavy minerals settle earlier than less dense rock fragments, pumice, light-weight minerals and silicic glass shards. Moreover, hydraulic floatation of crystals with disproportional shapes (e.g. biotite) enables the carriage in the atmosphere as far as much smaller particles and decreases the settling velocity in water.

Frequently reported post-depositional remobilization by wind in terrestrial environments can be precluded under the marine conditions of the Dwyka age in the study area, whereas gravitational and biological reworking in water is common.

4.2 Terminology and classification

Several textbooks and publications on volcanology and sedimentology (e.g. Fischer and Schmincke (1984)) discuss the aspects of pyroclastic rocks.

Schmid (1981) established a comprehensive terminology about pyroclastic deposits concerning size, stage of consolidation and manner of transport. The investigated thin, laterally persistent clay-rich pyroclastic layers interbedded with shales consist of altered fine-grained volcanic ash. Ash designates any kind of unconsolidated pyroclastic deposits with grain sizes smaller than 2 mm. Tuff is the consolidated equivalent of ash with a possible subdivision according to the depositional environment, manner of transport and petrographical composition. Pyroclastic-epiclastic mixtures with 25 to 75 % pyroclasts are tuffites or tuffaceous deposits. As objects of alteration tuffs transform into clay-dominated beds. The former name tonstein for such clay-rich persistent layers which turned out to be of volcanic origin was replaced with the term bentonite (Fischer and Schmincke, 1984). Tonstein is still frequently used to describe clay-rich beds with a major content of kaolinite in coal bearing strata (Spears et al. (1999), Bohor and Triplehorn (1993)). Fischer and Schmincke (1984) specified distinct bentonite types by their dominant clay minerals: smectite(S)-bentonite, illite(I)-bentonite or kaolinite(K)-bentonite. In contrast, metabentonite or K-bentonite is used in literature (e.g. Huff et al. (1997), Bangert et al. (1999), Spears et al. (1999)) for potassium-rich bentonites with K_2O concentrations of more than 3 to 4 wt% due to low-grade metamorphism. A gradual change into mixed-layer illite/smectite clays results from mainly vitric pyroclastic deposits (Bohor and Triplehorn, 1993). Microphenocrysts of accessory minerals trapped in the grains of ash often survive the alteration process and occur as microscopic euhedral crystals within the clay matrix. If the crystals in the ash grains constituted detrital grains, they would show signs of abrasion. In this study, the following terms mainly apply: A potassium-rich K-bentonite is an altered marine ash tuff (tephra) derived from a primary vitric fallout ash. The term tuff will be used though to perceive their origin.

4.3 Distal ash tuffs – characteristics and geological relevance

Ancient volcaniclastics are often difficult to deal with since layers alter to zeolites and clays. This process obliterates rock classifications, provenance determinations and genetic interpretations. With the geological age of ash tuffs, juvenile volcanogenic components – especially volcanic glass and mafic minerals – disappear gradually due to instability and high decomposability (Zimmerle and Gaida, 1980). Thus original volcanogenic characteristics are erased, especially in tuffaceous material. Present criteria to identify tuffs are volcanogenic structure and texture, diagnostic mineral constituents (primary components, relicts of primary components and typical secondary components formed during diagenesis) and geochemical parameters (element ratios) (Königer, 1999).

Additionally, minor thickness and indistinct appearance in distal settings make tuff layers difficult to recognise. Often only lighter colouring than that of the background sedimentation indicates primary volcanic deposits. Generally, good sorting, small grain sizes and distinctive euhedral, angular and shard-like grain shapes of volcanic fragments are typical characteristics (Fischer and Schmincke, 1984). Zimmerle and Gaida (1980) describe ancient tuffs to be partly of clammy consistence and waxy translucence, but diagenetic process (e.g. silicification) can even indurate tuffs enormously. They also point out that alteration effects, especially on major elements only, do not result in reliable chemical criteria. In contrast composite major and trace element ratios as well as rare-earth element ratios produce usable characteristics for discrimination.

Bentonites in particular are mostly interlayered with marine sediments. Interpretation of their volcanic origin is based on (1) thinness of beds (generally <10 cm), (2) wide areal distribution, (3) vitroclastic textures, (4) abundance of euhedral (phenocrystic) quartz, sanidine, plagioclase, amphibole, pyroxene, biotite, or zircon, (5) expandable sheet silicate minerals or zeolites derived from altered volcanic glass and (6) geochemical indicators (see 0) such as high concentrations of immobile incompatible elements, e.g. REE and Zr (felsic, especially alkali-rhyolitic ash), and characteristic element ratios indicative of igneous derivation (Schmincke and Bogaard, 1991)

In respect of stratigraphic appearance, volcanic ash is usually deposited very rapidly – in a geological instant – and will frequently tend to be preserved as relatively thin beds with sharp contacts above and below (Stollhofen, 1999). Ash layers deposited in subaqueous settings are more continuous over large areas and show more typical depositional structure and texture due to a high preservation potential. In contrast subaerial deposits are subject to bioturbation, reworking, secondary transport and redeposition.

Tuffs experienced a growing importance in intra- and interbasinal stratigraphic correlation as they overcome typical correlation limits such as the discontinuity of outcrops as well as the diachroneity and breaks in the fossil record. Additionally, primary components are radiometrically datable (Chapter 9). Therefore ash tuffs can be used as isochronous markers in chronostratigraphic classification of regional stratigraphic successions. Moreover, tuffs may possess an economic significance in exploration and exploitation of coal, oil and gas as well as being an important clay resource for the ceramic industry.

4.4 Stratigraphic nomenclature of the tuff beds at Zwartbas

During a mapping project, 65 distinct ash fall-derived volcanic tuff beds were logged within the basal 95 m of the lower part of the Dwyka Group outcrops at Zwartbas (Geiger, 1999). Although literature was available dealing with this locality, pyroclastic layers had not been recognised before. Further investigations required a nomenclature which regards the importance (thickness and thus assumed higher lateral extension potential) and indicates the stratigraphic position: During the logging several tuff beds have been combined to tuff groups, which are classified by **Roman numerals**. The classification primarily combines individual tuff beds, which are closely spaced. A second criterion was the particular thickness of the layers. Thick ash layers were preferentially ascribed to a particular group of ash layers, while thinner ash layers in the neighbourhood were included into the group. Particular tuff beds are marked by an attached **letter**. Both countings proceed successively upwards. This results in a classification identity (ID) made up at least by a Roman numeral and occasionally a letter. Thus, for example, the fourth tuff bed in the third tuff group is marked by the abbreviation IIId. Eventually 38 tuff groups were established to develop a tephrostratigraphic characterisation (Table 2).

4.4.1 Occurrence and macroscopic appearance of the tuff beds at Zwartbas

The exposed succession comprising tuff beds is predominantly restricted to the cliffs along the northern shore of the Orange River (Jet Cliff, # 8 to Fossil Bend, # 1). Studies on their lateral extent in a regional context could not be carried out because of the limited spatial coverage of this investigation. In any case, their very distal setting and the relatively undisturbed depositional environment suggest a continuous extension within considerable distance, at least for tuff layers thicker than 2 mm. Because of their small thickness they neither appear on a map nor have been studied yet (Figure 11A,B).

Upper and lower contacts of the laterally continuous tuff beds are planar and sharp. Local thickening of the tuff beds is due to secondary gypsum admixture, which colours these sections greyish to whitish. Commonly the tuffs are yellow-brownish coloured, which is due to their intensive alteration. In some cases the tuff beds pass laterally into up to 15 cm thick orange-yellowish carbonate concretionary beds and horizons. Normally their thickness varies from less than 1 mm to a few millimetres, particular layers are up to about 4 cm thick. They reach the highest density within the siliciclastic succession about 50 m to 70 m from the base of the Dwyka Group, where 30 ash layers were found within 20 m (see Figure 8). Best preserved and least altered tuffs are exposed at the cliff along the Orange River. The tuffs appear clammy and waxy, especially when the material is wet, and the tuff disintegrates easily by hand. Almost all tuff beds do not contain considerable proportions of epiclastic material, which is a sign of rapid deposition and lack of intense reworking. Only tuff beds III b and c are separated by a bright grey tuffaceous bed. Moreover, bioturbation of the tuffs is rather

rare. The tuff beds are – within the outcrop limits of the study area – laterally continuous and excellently traceable.

Tuff ID	Thickness	Colour	Diagenetic and alteration effects	Stratigraphic significance
I	5-6	brownish-yellow	Lateral transition into concretionary horizon possible	Medium
II a	2	brownish-yellow		Low
II b	1	brownish-yellow		
III a	1-2	brownish-yellow		Insignificant
III b	20-25	whitish-yellow with	Lateral transition into concretionary horizons proven.	High/Dating
III c	2-3	bright grey interlayer	Radiometric age of IIIb: 302.7±2.2 Ma (Chapter 9)	
III d	2	brownish-yellow		Insignificant
III e	0-2	brownish-yellow	Lateral discontinuous	Insignificant
IV	15-20	whitish-yellow		Low
V a	15-17	bright greyish-yellow		High
V b	20-22	whitish yellow		
VI a	1	brownish-yellow		Insignificant
VI b	4-5	brownish-yellow		Insignificant
VII	30	yellowish-white		High
VIII a	1	greyish-yellow	Lateral transition into concretionary horizon proven	Insignificant
VIII b	15	greyish-yellow	Lateral transition into concretionary horizon proven	Insignificant
IX a	1-2	yellow		Insignificant
IX b	1-2	brown	Lateral transition into concretionary horizon proven	Insignificant
X	30-40	whitish-yellow	Lateral transition into concretionary horizon proven	High
XI a	3	brownish-yellow		Low
XI b	2	brownish-yellow		
XII	5-15	greenish-yellow		Medium-High
XIII	5-15	greenish-white		Medium-High
XIV	3-4	yellowish-orange		Low
XV	8	yellowish-orange		Low
XVI a	2-4	yellowish-white		Medium
XVI b	2-4	yellowish-white		
XVI c	1-2	yellowish-white		
XVI d	1	yellowish-orange		Insignificant
XVII	1-3	reddish-brown		Low
XVIII a	1	orange		Insignificant
XVIII b	1	brownish-orange		Insignificant
XVIII c	1	brownish-orange		Insignificant
XVIII d	15	yellowish-orange		Medium
XIX	35	whitish-yellow		High
XX a	2	brownish-yellow		Insignificant
XX b	3-4	yellowish-white	gypsum formation	Insignificant
XXI a	1	greyish-yellow		Insignificant
XXI b	3	whitish-yellow		Insignificant
XXI c	1	whitish-yellow		Insignificant
XXI d	1	brownish-orange		Low
XXI e	2	brown		
XXII	3-4	reddish-brown		Insignificant
XXIII a	4-5	brownish-orange		Insignificant
XXIII b	30	whitish-yellow		Low
XXIV a	35	whitish-yellow		Low
XXIV b	5	yellowish-orange		Insignificant
XXIV c	2	yellowish-orange		Insignificant
XXV	<1	brownish-orange		Insignificant
XXVI	1-2	greyish-white	gypsum formation	Insignificant
XXVII	1-2	greyish-white		Insignificant
XXVIII a	15	greyish-yellow		High
XXVIII b	20	greyish-yellow		
XXIX	3	whitish-yellow		Insignificant
XXX	20	yellowish-grey		High
XXXI	1	whitish-grey		Insignificant
XXXII	4-5	whitish-grey		Insignificant
XXXIII	3-4	yellowish-grey		Insignificant
XXXIV	10	whitish-yellow	Radiometric age: 307.1±6.2 Ma (Chapter 9)	High/Dating
XXXV	3	greyish-yellow		Insignificant
XXXVI	3-4	whitish-orange		Insignificant
XXXVII a	1-2	whitish-orange		Insignificant
XXXVII b	2-3	brownish-orange		Insignificant
XXXVII c	1-2	brownish-orange		Insignificant
XXXVIII	1-2	greyish-yellow	uncertain lateral persistence	Insignificant

Table 2: Characteristics of individual ash tuff beds recognised at the cliff outcrops along the Orange River and the incoming dry river channels. Tuff bed ID is taken from Geiger (1999). The thickness is given in millimetres. Important tuff beds are highlighted.

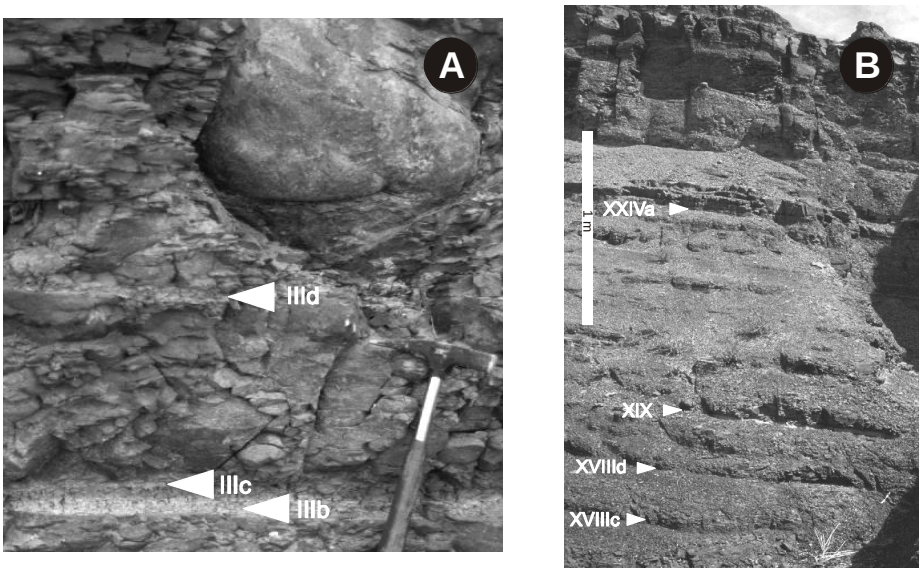

Figure 11: Shale succession with interbedded thin bentonite beds. (A) Jet Cliff (# 8) at the Orange River documents the sequential ash tuff deposition. Marker beds are indicated. (B) The close-up of tuff bed IIIb, IIIc and IIId shows the clear optical distinction from the surrounding shale. Between IIIb and IIIc tuffaceous material (shale admixed with ash tuff material) is grey coloured (Fossil Bend, # 1). See hammer for scale.

4.5 Frequency of ash fall events

Volcanic eruptions may take place in rhythmic sequences because of the interaction of magma reservoir refill and reservoir pressure-loss by eruption. Volcanoes are commonly fed by magma chambers at some depth. The magma chamber itself is fed by vents from deeper sources. Whilst up-flowing magma presumably refills the chamber discontinuously, the pressure in the confined reservoir of the still inactive volcano increases. Since volcanoes are normally situated at tectonically active areas, seismic pulses trigger the over-pressured magma chamber to ascend. Predefined fault zones often give way to the rising magma which eventually erupts through vents on the surface. As a result of the discharge, reservoir pressure drops, discharge diminishes and the vents are plugged, a caldera may form and finally the pressure may rise again. Proposing constant conditions, eruptions may occur in a cyclic manner and so ash-falls do.

4.5.1 The Fast Fourier Transformation (FFT)

A useful tool for examinations on cyclicity within time series is the Fourier Transformation for periodic functions analysis (cf. Schönwiese (1985)). All periodic waves can be generated by combining sine and cosine waves of different frequencies. If the number of frequencies is *infinite*, the Fourier Transformation can be employed to decompose a periodic wave into its component frequencies. A practical algorithm for *finite* (discrete) time series is the Fast Fourier Transformation (a discrete Fourier Transformation), which uses the terms of a Fourier series to find a function that approximates periodic data within a periodic wave. Further mathematic explanations are given in Schönwiese (1985). In this study the Fast Finite (discrete) Fourier Transformation of the MATLAB software package was applied on an artificial frequency of tuff bed occurrences. Schönwiese (1985) notes that results may vary up to 10 % within different software packages caused by modifications, e.g. the window functions, and elucidates that the results are more likely estimations which need interpretation.

4.5.1.1 Data preparation

To transform the stratigraphic data into a usable frequency, the lithology was taken as function of tuff bed occurrence with the value of its thickness (amplitude). The value for shale was set as y=0.

Thus a frequency was obtained with a normal function value '0' for shale and occasionally peaks comprising tuff beds with an amplitude corresponding to the bed thickness. Eventually, a data range was selected that comprised 1024 data points to fulfil the required sample numbers of a power-of-two ($n = x^2$, with x = 1,2,3...). For temporal reference the stratigraphic thickness was transferred into an equidistant time series using a much generalised sedimentation rate of 5 mm per year (Chapter 3.1.2.2). This inaccurate distance-time transformation especially results in an inaccurate temporal reference of the result.

4.5.1.2 Calculation and interpretation

The MATLAB Fast Fourier Transformation is based on a Radix-2 Fast Fourier Transformation algorithm. After the application of the FFT algorithm, the results were visualised in a power spectrum (analysis of variance) by power vs. frequency.

A first glance at the power spectrum reveals no extraordinary peak and thus no superior cyclicity (Figure 12). All peaks are very sharp, which demands exact periodic functions as their origin (Schönwiese, 1985). Because of their abundant occurrence in respect to the small data number, they are considered as background-noise-like frequency without any expressivity. From this background frequency only two very sharp peaks outstand. Since they do not differ much in power from the background frequency, their statistic relevance is little. Taking into account the previously mentioned methodical uncertainty, especially the uncertain temporal reference attained by the laminites, the result is at least an estimation of cyclicity. Since the calculated cyclic functions coincide with the high frequency of tuff bed occurrence concentrated in the central fossiliferous and lithologically homogeneous section between tuff horizon VI and XXVIII, a constant sedimentation rate was presumed even if not proven. The apparent continuity of the sample conditions corroborates the expressivity of the high-frequence cyclicity, and, disregarding the inaccuracy of the distance-time transformation (Chapter 4.5.1.1), thus the analysis presents cyclic functions with periods of about 6.7 and 48.7 years.

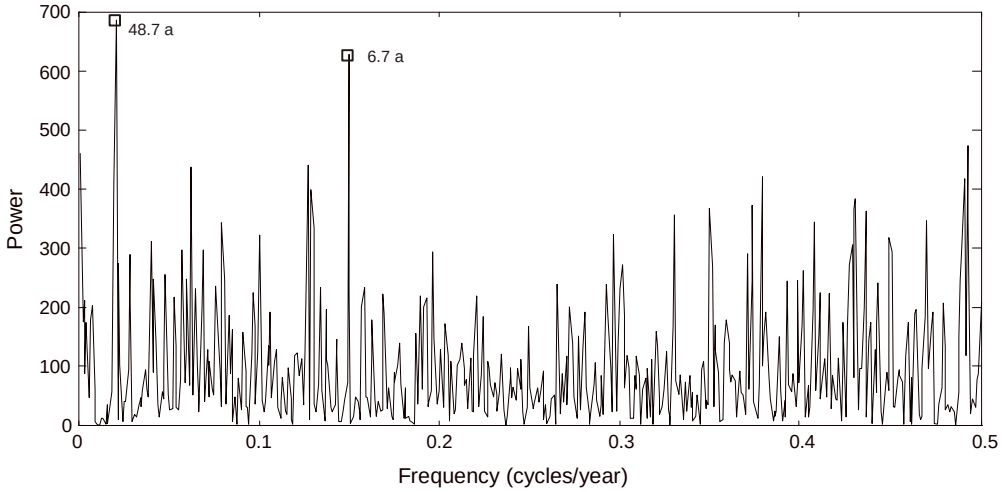

Figure 12: Power spectrum of the tuff bed time series. Abnormal high peaks at 6.7 and 48.7 years may point to cyclicity of pronounced volcanic activity.

Several control analyses of tuff bed time series were carried out with methodical modifications. For example, calculations were made with variable sample numbers (not a power of two: $n \neq x^2$, with x = 1,2,3,...) to force MATLAB to employ its alternative non-power-of-two algorithm. Further the data set was prepared different using variable sedimentation rates and a single standardised tuff bed thickness. All optional calculations turned out to be less meaningful.

4.5.2 Distribution histogram analysis

A mathematically more simplified method to find a dominant thickness of shale between subsequent tuff beds is the application of a histogram, a simple frequency distribution of bedding thickness of shale layers between two confining tephra layers (Schwarzacher and Fischer, 1982). The width of the histogram bars represents class intervals (thickness) and the areas are proportional to the frequency of a distinct class interval. Thus, the longer the bar of an particular interval is, the more frequent are shale units of the thickness, specific for this interval.

The shale units were classified due to their thickness in intervals with

$$I_n = [>(n \cdot 5); \leq((n+1) \cdot 5)] \text{ and } n = 0, 1, 2, 3, \ldots \quad [\text{cm}]$$

Figure 13 shows the most prominent frequency for the >20 to ≤25 cm interval and the second highest frequency for the >5 to ≤10 cm interval. Accounting the sedimentation rate in Chapter 3.1.2 the highest bar of the interval of >20 to ≤25 cm equals about 40 to 50 years and approximates at its upper interval limit the dominant frequency of about 49 years in the FFT power spectrum (Chapter 4.5.1.2).

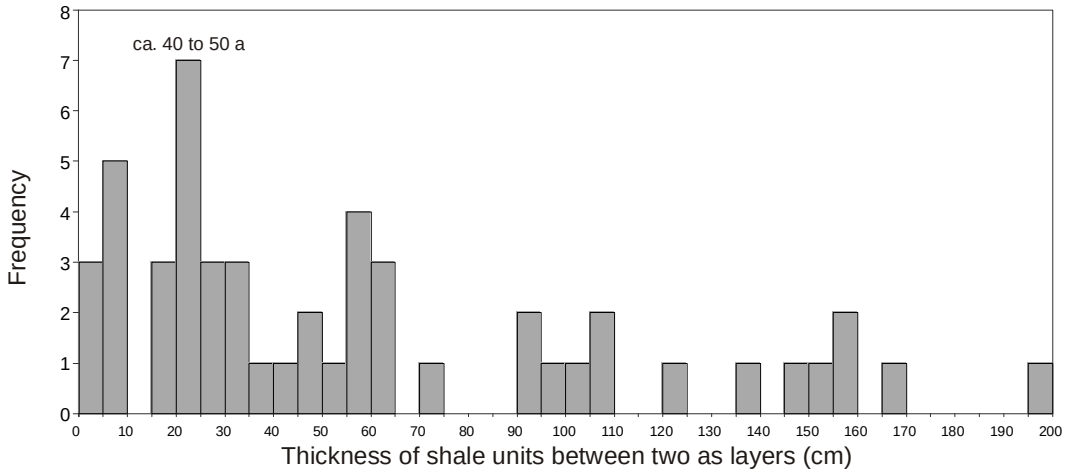

Figure 13: Histogram of shale units of similar thickness (interval) between two ash layers versus their frequency (bar height). Intervals were defined as [>(n·5); ≤((n+1)·5)] and n=0, 1, 2, 3, ... [cm].

4.6 Potential influences of ash falls on life

The deposition of large quantities of volcanic ash can produce significant effects on biological and hydrological regimes. Onshore impacts can influence plant growth, soil nutrient concentrations and surficial drainage (Bohor and Triplehorn (1993). But it may need ash layer thicknesses of several decimetres to attain sustained changes. Similar properties can be expected for a subaqueous environment by an increased input of chloride and sulphate into a marine environment, which would be analogically fatal for life. Moreover, acid ashes in particular may change the chemistry of water bodies by developing low pH-values. The resulting lethal conditions for organisms may effect a higher mortality and therefore fossil preservation in sediments that were deposited immediately after the ash settled (Königer, 1999). Frommherz (1998) pointed out that the impact of thin ash layers in the Carboniferous-Permian Saar-Nahe Basin (SW Germany) had no constant effects on swamp area vegetation. Similar observations were made on thick Ordovician bentonites in North America and Europe (Huff et al., 1992). Nevertheless, Grill (1997) considered such thin ash layers, which were deposited into a glacio-marine environment as being capable of killing-off algal-serpulid bioherms.

At Zwartbas the appearance of fossilised organisms coincides with an increased frequency of ash-fall-events (Figure 8). A significant correlation, however, of an ash-fall-caused eutrophication and the abundance of organisms cannot be confirmed.

An additional aspect of environmental changes by volcanic activity is the global effects attained by volcanic dust, ash and gas from large explosive eruptions. They may still effect environments far from the eruption site. In some historical events a global cooling was confirmed (Königer, 1999).

The development of models for the influence of ash falls on life becomes increasingly difficult in a glacio-marine setting. The enormous fresh water influx by the glacier and potentially a coherent nutrients input from ash-falls on the glaciers may shift acidity and concentrations of nutrients in an unpredictable manner. Salinity contrasts between distal marine and proximal fresh water may also lead to a circulation within the water body, which improves the exchange of chemical components and heat. Furthermore, the high effective heat capacity of water compensates rather easily short-term atmospheric temperature changes.

Chapter 5 Fossil Record

The glaciogenic Dwyka Group in Namibia only recently became known for its fossil abundance. In the Mariental area numerous petrified wood and plant remains, fishes, coprolites, gastropods, bivalves, trace fossils, microbial bioherms, conulariida, porifera and crinoid columns were discovered (Grill, H., 1997; Bangert et al., 2000). Earlier works reported findings of a cephalopod (Du Toit, 1916), a goniatite (Martin et al., 1970), radiolaria and foraminifera (Martin, 1981a). McLachlan and Anderson (1973) and Pickford (1995) give helpful information about individual fossil findings and fossil distribution in Karoo deposits in southern Africa. Findings at Zwartbas, already briefly described by Geiger (1999), were restricted to fish, plant and wood remains, coprolites and numerous species of invertebrate ichnogenera. One gastropod shell could not be determined in detail, while another probable shell-fossil could not be determined at all. Findings were generally made at the cliffs along the Orange River from Jet Cliff (# 8) to Fossil Bend (# 1).

5.1 Palaeoniscoid fishs

Scales, bones, fins, skull fragments and jaws, or corresponding partly carbonised moulds of disarticulated palaeoniscoid fish remains (order: Palaeoniscoidea; family: Acrolepidae) were discovered in numerous oval-shaped phosphatic-siliceous concretions. The fish fossils comprise either the skull or the torso and are generally preserved dorsoventral within the bedding. One mould yielded a contiguous surface with abundant scales bordering to a well preserved mould of fin rays with several about 2 mm thick and up to 4 cm long spines (Figure 14A). All findings were concentrated between tuff beds VI and IX, including 4 cm long jaw bones bearing isolated sharp teeth, which are maximum 0.5 mm thick and 1.5 mm long (Figure 14B). As the fossilised bones of the fishes are mostly disrupted, generic classifications are mainly based on structure and arrangement analyses of the coherently preserved scales (Bangert et al., 2000). The new findings were determined as *Namaichthys schroederi* Gürich, 1923 by their rhombic to rectangular 3 to 5 by 2 to 3 mm large scales, which are not imbricated and show slight or no ornamentation and are often draped with a bluish enamel.

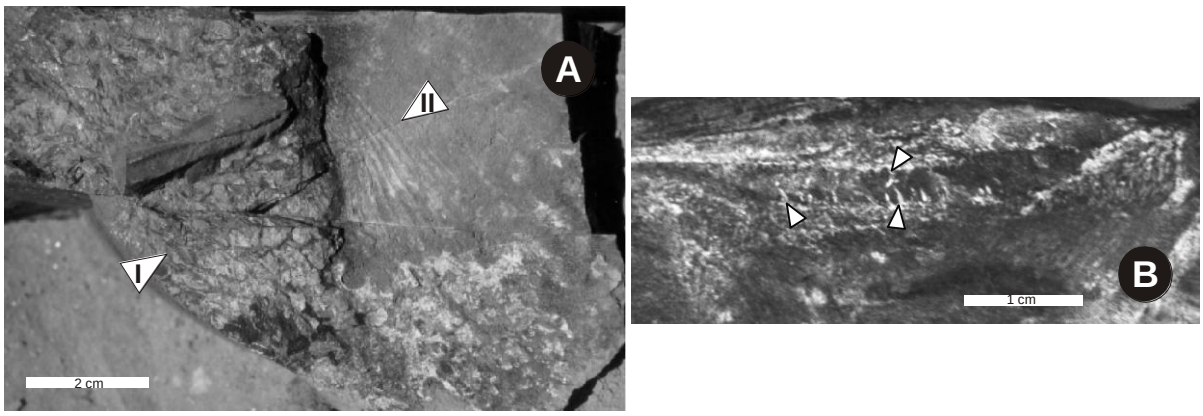

Figure 14: Views on fracture planes through nodules parallel to bedding. (A) Accumulated rhombic scales with bluish enamel (pointer I) bordering the mould of a fin outlined by spine rays (pointer II). (B) Jaw bones with isolated sharp teeth indicated by the pointers.

5.2 Spiral Coprolites

The most frequent fossils besides the ichnofossils are the spiral coprolites, which occur at the stratigraphic position of tuff groups VI to XI, XV to XVI and around XXIX. These commonly up to 10 cm long straight vermicular fossilised feces with a radial diameter of about 2 cm consist of a coiled 2 to 3 mm thick excrement layer with up to 5 windings (Figure 15). Sharks with an intestinal spiral valve were supposed to be the producers of these structures (McLachlan and Anderson, 1973).

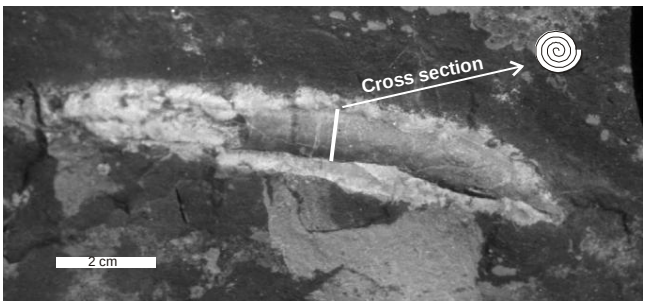

Figure 15: View on a fracture plane through a nodule showing the side view of a spiral coprolite. The common coiled internal structure depicts the schematic illustration in the upper right corner.

5.3 Calcite filled spheres

Small 0.5 to 1.0 mm large calcite filled spheres were macroscopically recognised only in nodules between tuff groups VI and XXV, where they are aligned within the bedding (Figure 16). Wheter they are of biogenic origin could not be confirmed without doubt, so a detailed microscopic inspection is given with the petrography in Chapter 7.1. Considering their appearance and earlier reports of radiolaria in Dwyka rocks (Martin and Wilczewsky, 1970; McLachlan and Anderson, 1973), a corresponding interpretation is acceptable. Radiolaria, however, are pelagic organism, which is contradictory to the coherent presence of wood and plant fragments indicating rather proximal marine conditions. Grill (1997) describes similar calcite filled spheres, but with an internal concentric structure and considers them as algal layers of Dasycladacea, which are tubular organism. However, since no tubular but only spheric sections were found, this interpretation is unlikely.

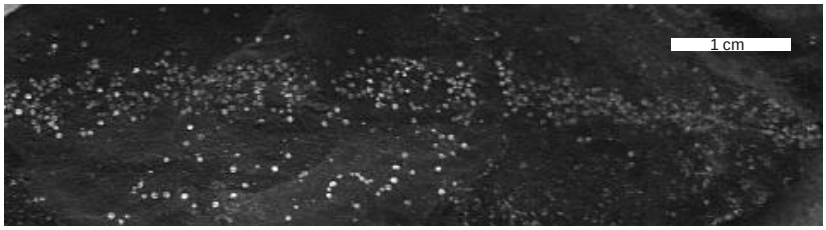

Figure 16: View on a fracture plane perpendicular to bedding. The calcite filled spheres, 0.5 to 1.0 mm in diameter, are aligned in layers parallel to bedding.

5.4 Permineralised wood and plants

Fragments of permineralised wood have been frequently observed between tuff groups VI and X, XV and XVII and between XXIII and XXVIII. Small branches with diameters of only 2 or 3 cm appear along with wooden logs up to 30 cm in diameter (Figure 17A). The frequently vertically flattened logs are found either enclosed in concretions or isolated and are coalified or silicified. Growth rings are usually well preserved and vary from 2 to 10 mm in thickness. Along these growth rings and also along vessels of coalified wood, pyritic bands sometimes occur.

Associated with the logs are nodules containing several 2 to 4 cm long parallel, ferric-brown coloured fibres, each less than 1 mm thick, and 1 to 1.5 mm thick hollow vessels filled with calcite. These potential leaves occur along with more or less concentric finer filaments, which could be remains of bast fibre or cones (Figure 17B).

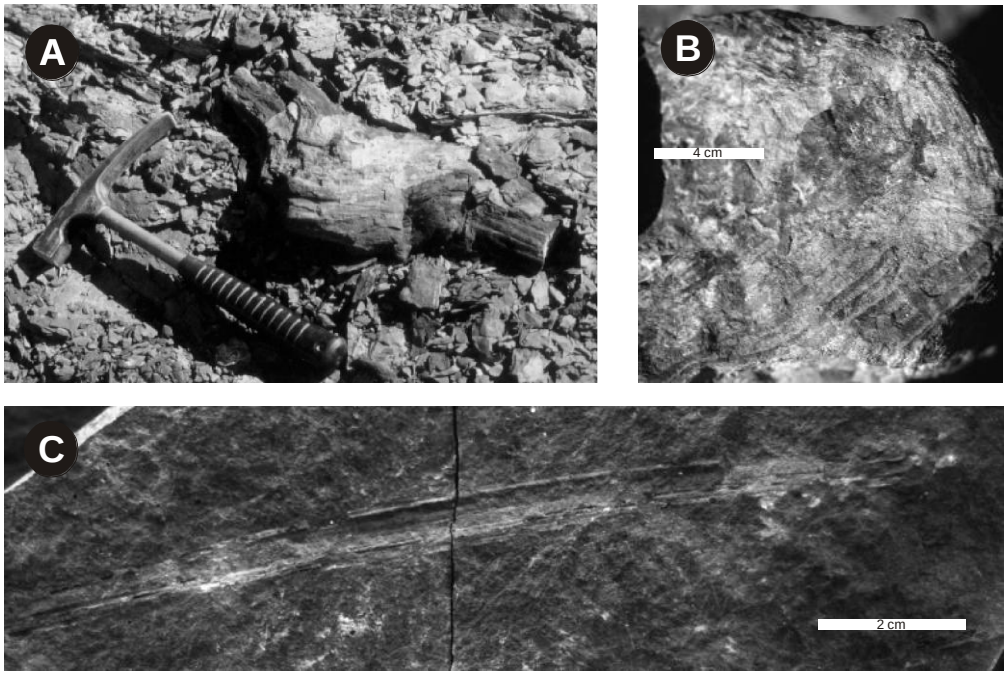

Figure 17: Photographs of fossilised plant fragments. (A) Permineralised wood fragments reach some tens of centimetre in length and up to 20 cm in diameter. (B) Permineralised log with thick growth rings. (C) Fossilised plant fragments, probably from a leaf or cone.

5.5 Invertebrates

Between tuff horizon IX and X an external mould of a yet undetermined shell was found. Probably one valve or at least a part of one valve could be excavated. The shell is crescent shaped with a bending ridge extending from the umbo to the convex body. Ramified crests of the size of a fraction of a millimetre, similar to the pattern of the skin of the human hand, cover the shell. The longer wing next to the umbo shows a 3 cm long, 0.5 mm wide and at least 0.5 mm deep recess. McLachlan and Anderson (1973) report of a Lamellibranch classified as Phestia sp., whose shape approaches the new finding. A similar fossil was found by B. Bangert (1999, pers. comm.) near Tses in the Aranos Basin, but could not determined either.

Between tuff group XXIV and XXV, a isolated white spiral gastropod shell was found. The 0.6 cm long, evolute trochospiral shell, however, could not be specified accurately.

5.6 Invertebrate ichnogenera

Numerous invertebrate ichnogenera, e.g. domichnia, fodinichnia and pascichnia, were recognised within the complete section. Only about 1.5 m above the basal tillite, a competent varved layer bears the lowermost fossil observed at Zwartbas. Upon a bedding plane an one-order-meandering structure with 1 to 2.5 cm wide lobes of a 3 to 4 mm wide and 1 mm deep grove (Figure 18) were interpreted as pascichnia of *Helminthopsis* isp. These tracks may correspond to the invertebrate tracks discovered by Haughton and Frommurze (1928).

In the succeeding stratigraphy numerous burrows were encountered, some of which could be clearly determined. Black nodules in the stratigraphic levels of tuff groups X, 2 m to 3 m above XI, between VII and XV and sporadically 4 m to 6 m above the Goats Cliff Diamictite are covered with 3 to 5 cm wide, several cm long vermicular burrows, which form a smooth, convex semi-relief on the surface of the nodules (Figure 19A). Fracture surfaces show meandering, cylindrical, unlined, endichnial burrows, which are lighter-coloured than the surrounding sediment. They cross the rock horizontally or obliquely to the bedding. Especially the meniscate backfills with less than 1 mm thick menisci lying

relatively constant 2 to 3 cm apart, point to *Taenidium serpentinum* Heer, 1877, which is an indicator for low-energy oxygen-limited environments of a storm-dominated inner shelf (Bromley, 1996).

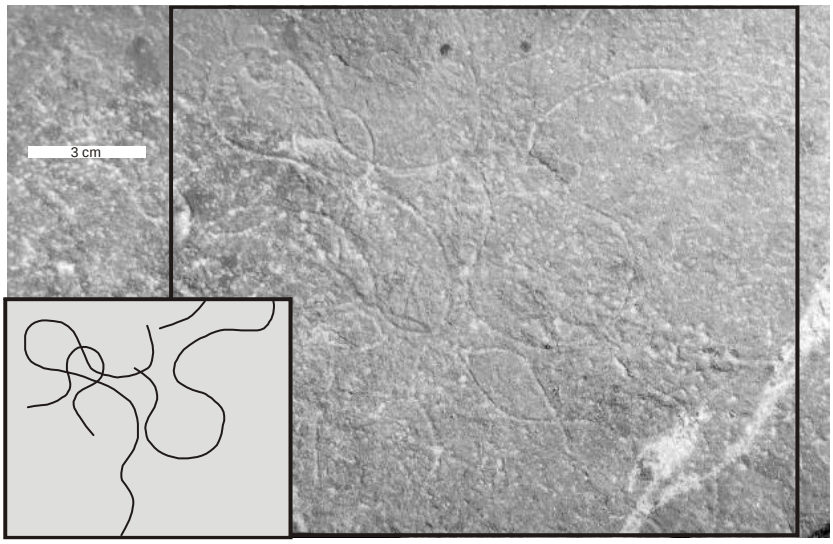

Figure 18: Bedding plane view of the one-order-meandering feeding trace of *Helminthopsis* isp.

A system of 1 to 2 mm thick tree-like branched, downward penetrating intrafaunal burrows, which were commonly found within sandy beds between tuff group IX and 3 m above tuff group XI, are regarded as *Chondrites intricatus* Brongniart, 1823. The branches form sharp angles, the burrows are filled with lighter material than the host rock. *Chondrites* suggests marine conditions and is often associated with low-oxygen substrates (Bromley, 1996).

The layers of tuff group IX also contain a branching 0.5 to 1.5 cm thick burrow with Y- or X-shaped branches of *Thalassinoides* isp. which produce a horizontal to oblique box-like network with enlargement at their junctions (Figure 19B). On weathered surface the burrows remain as smooth, convex semi-relief. *Thalassinoides* commonly appears on silt or fine sand layers.

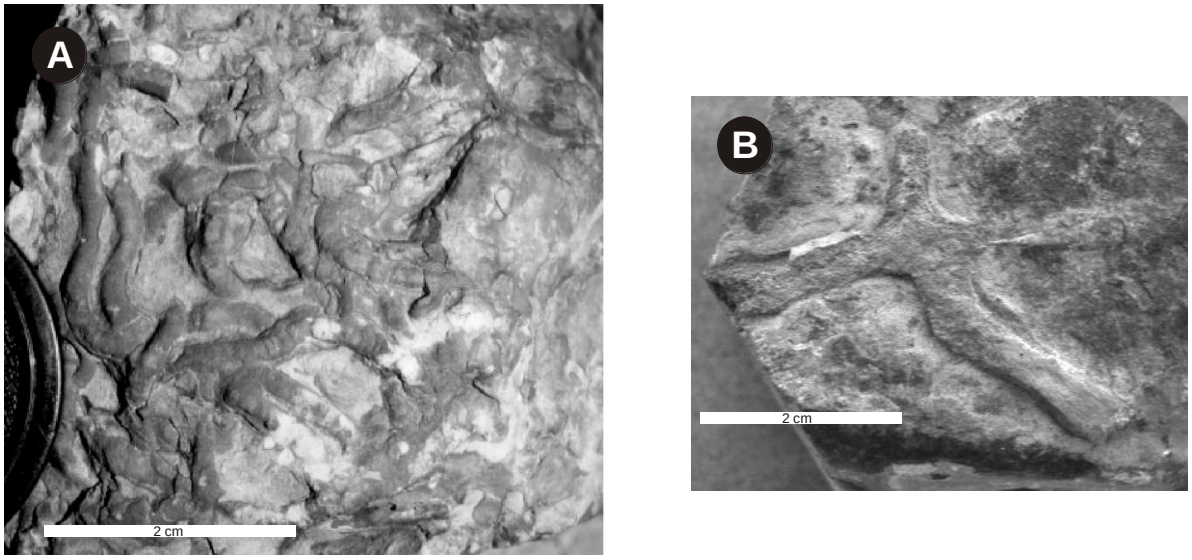

Figure 19: (A) View of the surface of a nodule bearing contours of *Taenidium serpentinum.* (B) View of the surface of fine-sandy bed showing the semi-relief of *Thalassinoides.*

Between tuff groups XI and XIII several of the brown concretions have two cylindrical hollows, which are 1 to 3 cm across and reach 2 to 3 cm vertically into the top surface (Figure 20A). Tubes always appear in pairs, which are 1 to 4 cm apart from each other. Similar, but horizontally lying

structures, which are enveloped in tubular black concretionary nodules, occur from tuff groups XXVII to XXXI (Figure 20B). There are normally two, but occasionally three, 1 to 2 cm wide, 30 to 40 cm long tubular burrows together in one concretion. Both tubes narrow to their one end and approach each other, but they have not been observed to merge. These burrows were considered to be *Tisoa* isp., which were probably recognised already by Haughton and Frommurze (1928), who suggested a relation to *Tisoa siphonalis* in the Upper Charmouthian, France.

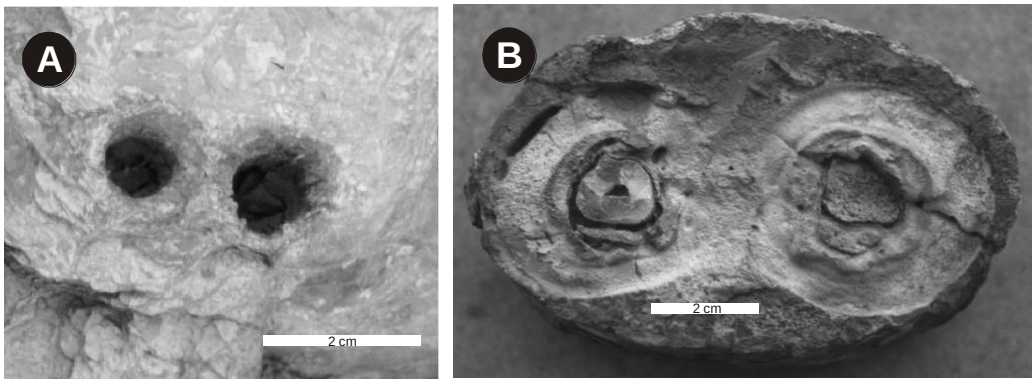

Figure 20: (A) Pairs of tubes of *Tisoa* isp. recede vertically from the surface of a brown concretion just above tuff group XI. (B) Cross section through a flat lying tubular concretion containing *Tisoa* isp. Chalcedony lines the left burrow, leaving a central tubular cavity. The right burrow is completely filled with sediment.

A simple, tube-like up to 3 cm long and up to 0.8 cm wide, vertically oriented unbranched burrow, which typically shows a much greater length versus width, is the stratigraphically most abundant and pervasive fossil. Slightly distinct, smooth burrow walls line an unstructured fill. Such tubes, determined as *Skolithos* isp., appear from tuff groups II to XXX with only few interruptions. *Skolithos* occurs mostly in various shallow-marine environments with full oxygenation (Bromley, 1996).

The stratigraphically uppermost fossil, *Palaeophycus* isp., was discovered only 4 m above the White Horizon, thus close to the Dwyka-Ecca boundary. It appears as a 2 to 3 mm thick cylindrical occasionally branching burrow, which contains a typically structureless filling of the same lithology as the hostrock and is oriented horizontally or obliquely to bedding. *Palaeophycus* is related to a shelf environment (Bromley, 1996).

5.7 Environmental perceptions at Zwartbas by means of palaeontology

Apart from the lithofacies, fossils are another practicable indicator for palaeoenvironmental modelling. Considering the fauna at Zwartbas, none of the recognised and confidentially identified fossils indicate without doubts marine conditions in the sense of present-day marine salinity. *Skolithos*, *Chondrites* and *Thalassinoides*, however, are forms typical for offshore marine conditions, whereas *Palaeophycus* colonises typically during marine incursions and *Taenidium* in non-marine environments (Bromley, 1996). Estimations about the water depth, however, can be obtained from the fossilised fauna, because most forms (e.g. *Skolithos*, *Thalassinoides*) indicate shallow water, commonly shelf environment. Correspondence with the presumption of an epicontinental incursion is thus achieved. Moreover, *Helminthopsis* and *Chondrites* indicate at least partially a relative oxygen depletion, which may also be responsible for the good preservation of abundant fossils.

Abundant large plant remains also infer a proximal situation to the shore and ample vegetation at the coast and/or the proximal hinterland. Lager trees preserved as permineralised logs, up to 30 cm in diameter and growth rings about 1 cm thick, indicate a suitable climate, which is also inferred by temperature estimations of the source area from geochemical analyses on the shales (Chapter 7.5).

Chapter 6 Petrographical and geochemical analytics

Petrographical analyses aspire to elucidate the textural and structural grain features and the determination of the mineralogical composition of both tuff and shale. Geochemical analyses deliver chemical compositions by which diverse classification can be obtained. Thus tectonic settings of the sediment source and palaeoenvironmental conditions for shale deposition and classifications of the parental melt from which the tuffs derived, and their tectono-magmatic setting can be determined. The co-operation of petrographical and geochemical analyses complements and verifies working hypotheses gained by regional context and correlation, palaeontological findings and sedimentology.

6.1 Sample selection

All samples were taken from the relatively fresh outcrop along the Orange River (Jet Cliff, # 8 to Fossil Bend, # 1), where steep cliffs and walls provided the least altered rocks.

6.1.1 Shale

Based on field observations and studies of hand specimen, 16 shale samples were selected. About every second metre a sample of almost unweathered shale was taken from the cliff, thus the complete sampled succession reached 62 m above the Dwyka base. Stratigraphic horizons containing bentonites were avoided and consequently the sampling distance was varied a little to prevent analytical interference by tuffaceous material. Lateral sampling was disregarded due to the small lateral outcrop extent.

6.1.2 Bentonites

All ash fall deposits were pre-selected in respect to their purity to avoid considerable interference with epiclastic material. Nevertheless, some samples might have been admixed with detritus and thus represent tuffaceous deposits. Sampling of the just 0.5 to 2.5 cm thick bentonites was accomplished by delving with a trowel and gathering the scooped out fragments of bentonite, up to 3 to 4 cm large and 1 to 5 millimetre thick. Samples derived mainly from tuff beds IIIb (3 samples), VII (2) and XXIVa (4). Multiple samples were collected 20 to 50 m laterally apart. Single samples were taken from tuff beds VIIIb (thin-section), X, XIII, XVIIId, XIX, XXIc and XXXIV due to their small thickness.

6.2 X-Ray Diffractometry (XRD)

Larger tuff and shale fragments were crushed with a hammer. From the sample material, 150 to 200 g of fresh material were hand-picked and pulverised (grain size <40µm) by the author using a swing mill with an agate grinding vessel. A complete homogenisation was aspired.

X-ray diffraction analyses performed on sample powder provide the bulk mineralogy of nine sampled tuff horizons, since thin-section analyses were hampered by their microscopic to sub-microscopic appearance. A detailed identification of expandable clay minerals is usually carried out on control samples after a treatment with organic reagents (glycolation). The reagents expand the lattice along the clay layers in accordance to the mineral constitution and thus shift the peaks characteristically. The most commonly used solvents are ethylene glycol and glycerol. In this study glycolation was disregarded because of the very protractive preparation and even the untreated samples delivered useful results.

For the same reason and because of the relatively pure clay samples, certain pre-treatments were renounced, which are normally required to remove undesirable coatings and cements, either to improve the diffraction characteristics of the sample or to promote dispersion during size fractionation.

XRD analyses were also performed on 7 shale samples, 2 samples of concretionary horizons and 3 diamictite/tillite samples. The XRD measurements were carried out at the Institut für Mineralogie of the Universität Würzburg with a PHILLIPS PW 1800 goniometer supplied with monochromatic Cu-

Kα radiation at an acceleration voltage of 40 kV and a heat current of 40 mA. The powder diffractometer was configured in a Bragg-Brentano-geometry, which is a focussed geometry. Within the detection range of 4.00 to 80.00 °2θ the intensity was detected by steps of 0.02 °2θ at a step time of 1 s. Finally the measurements were automatically compared with X-ray data of the Powder Diffraction File Database (PDF-2) published by the ICDD (International Centre for Diffraction Data) and, especially the clay minerals, manually verified with assistance of data from Heim (1990).

6.3 Thin-section analysis

A few useful thin-sections of tuff beds and shale were kindly provided by B. Bangert, who obtained them from the technical laboratory at the Institut für Geologie of the Universität Würzburg. The fissile tuff beds were previously consolidated with epoxy resin. Thin-section studies were carried out with a LEITZ Laborlux 12 Pol S polarisation microscope.

6.4 Heavy minerals – grain mount analysis

Each sampled bentonite was disaggregated in a water-filled beaker by adding detergent, which reduced the surface tension of the water (Huff et al., 1997). This surfactant promoted decomposition of the clay material. One hour of moderate stirring with a magnetic bar mixer disaggregated the material almost completely. Then the suspension was wet-sieved in an ultrasonic bath to obtain minerals ranging from 45 to 200 μm. Residue in the 200 μm sieve comprised only detritus. The 90 μm sieve caught the important fraction of preserved minerals, while the totally altered fraction was rinsed out as fine clay suspension. After drying, sample material with a conspicuous proportion of opaque minerals (predominantly relatively heavy ore minerals) was separated after magnetism with a FRANTZ magnetic barrier laboratory separator, model LB-1 at a solenoidal power of 0.4 A DC and a chute inclination of 20°. Chute vibration frequency and feeder vibration frequency was permanently readjusted. Consequently, ilmenite, chromite and haematite were extracted (Ney, 1986).

Eventually, the non-magnetic fractions were separated with Sodiumpolytungstate-gravity solution ($3Na_2$-$Wo_4{\cdot}9Wo_2{\cdot}H_2O$, density 2.90 ± 0.02 g/cm^3 at 20 °C) within separator funnels over four hours. The isolated minerals were washed, dried and embedded into the permanent mount BUEHLER LAKESIDE 70C (n=1.54) thermoplastic cement on object carriers for optical identification. Optical studies were carried out with a LEITZ LABORLUX 12 Pol S polarisation microscope.

6.5 X-Ray Fluorescence (XRF)

X-ray Fluorescence measurements were taken at least from one sample of each tuff bed. Samples X, XXI and XVIIId only provide XRF but no ICP-MS data, whereas rare-element analyses were not carried out.

6.5.1 Preparation

Sample powder for the production of fusion discs was either taken from the XRD sample collection or was prepared similarly to that for XRD measurements (Chapter 6.2).

6.5.2 Loss On Ignition (LOI)

Loss On Ignition (LOI) was determined for each sample. The sample powder was dried at 105 °C for 10 hours. After cooling 1 g of powder was weighed in a porcelain beaker and heated at 1000 °C for 4 hours. After another cooling LOI was calculated from the weight difference of the dried and heated sample.

6.5.3 Whole-rock analysis of major and trace elements

Measurements of major and trace elements were taken on fusion discs by XRF-spectrometry at the Institut für Mineralogie of the Universität Würzburg. Exact 0.6 g of dried sample powder was mixed

with 3.6 g of lithium tetraborate and lithium metaborate (MERCK SPEKTROMELT A 12). Total iron was determined as total Fe_2O_3 by a total conversion of Fe^{2+} to Fe^{3+} with additionally 1.5 g of ammonium nitrate (NH_4NO_3). The mixture was melted in a platinum crucible in four steps to finally 1000 °C, decanted into a platinum disk mould and cooled in an air stream. The disks were analysed in a PHILIPS PW 1480 XRF spectrometer with a Rh target tube, and achieved data were processed with the measuring program GEO-1 of the PHILIPS X 40 software package. Corrections were based on calibration by international rock standards: GSS-1 (soil) and GSS-6 (soil), NIM-L (lujavrite), MAG-1 (marine mud) and GH (granite). The analytical error of major elements varies - dependent on the proximity of detection limits – between 1 and 3 %. Detection limits of trace elements range from 5 to 10 ppm. Close to the limits the precision errors of trace elements increase commonly from 10 % to 50 %.

XRF measurements of major and trace elements of some samples were taken together with the ICP-MS measurements at the Institut für Geologie und Dynamik der Lithosphäre of the Universität Göttingen. A deviation diagram of samples measured both in Göttingen and Würzburg points to inconsiderable discrepancies between both laboratories (Figure 21).

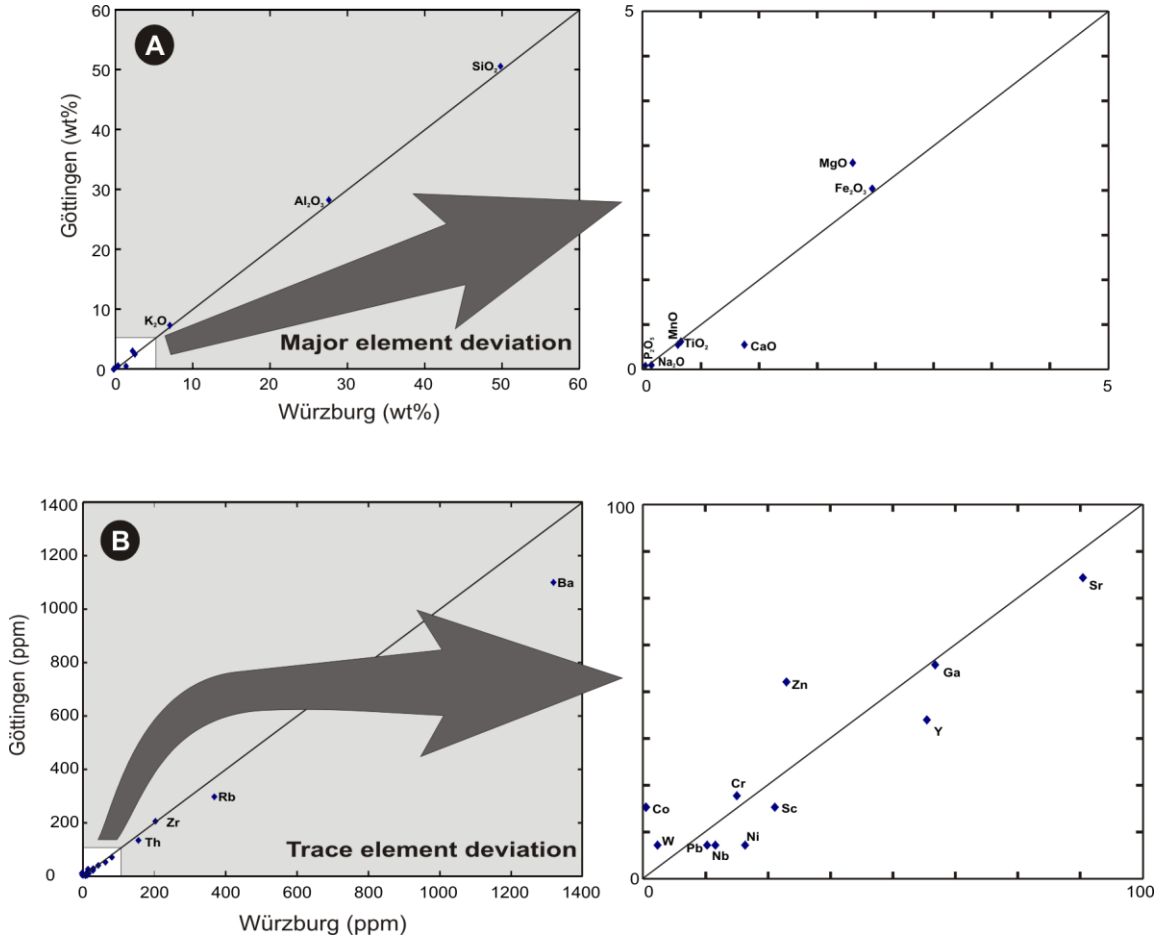

Figure 21: (A) Major and (B) trace element concentrations of tuff sample IIIb-2 analysed with XRF and ICP-MS (value selection is explained in Chapter 6.6.2) at the Institut für Geologie und Dynamik der Lithosphäre of the Universität Göttingen and compared to XRF determinations from the Institut für Mineralogie of the Universität Würzburg.

6.6 Inductively Coupled Plasma – Mass Spectrometry (ICP-MS)

From all sampled tuff beds, seven well preserved samples were chosen to carry out ICP-MS measurements additionally to the XRF analysis to obtain supplementary rare-earth element and more exact trace element concentrations.

6.6.1 Preparation

Sample powder for the ICP-MS was either taken from the XRD sample collection or was prepared in a similar manner to that for XRD measurements (Chapter 6.2).

6.6.2 Whole-rock analysis of trace and rare-earth elements

Measurements of rare-earth (and complementarily of some trace) elements were solely carried out at the Institut für Geologie und Dynamik der Lithosphäre of the Universität Göttingen by ICP-MS. For double-measured trace elements XRF values were used for Zr, Sr, Ba, Rb. ICP-MS values were used for Nb and Pb, when values exceeded 50 ppm, as well as for Y, when values were smaller than 50 ppm (Ruppert, written comm., 1999). Sample preparation was done as follows.

About 100 mg dried sample powder was disintegrated under pressure by 4 ml HF (48 %) and 4 ml $HClO_4$ (70 %) and left in a polytetrafluorethylen (PTFE) crucible at 160 °C. Arising vapours were subtracted. Residues were mixed with 4 ml HNO_3 (65 %) and 1.2 ml 6n HCl and filled up with H_2O to 200 ml. The solutions were clear and without any residue. Determinations were carried out on a FISONS ICP-MS PQ2+ with an internal standard of 20 µm/l Indium. International rock standards for calibration were BB46 (mafic) and DR-N (diorite). Considerably above the already small detection limit, the analytical error is less than 5 %.

6.7 Element Analysis of Total Organic Carbon and Nitrogen

Carbon (C) and nitrogen (N) measurements were performed by the laboratory of the Institut für Geologie und Paläontologie of the Universität Tübingen. Sample S7 was excluded to avoid circumstantial decarbonisation, because XRF results suggested a carbonate gain, which may cause damage to the instrument. Measurements were performed on an element analyser ELEMENTAR VARIO EL in the CN mode to detect C and N.

Sample powder from the XRD was weighed in small tin boats. Sample loading of the analyser worked automatically. Inside the analyser samples combust explosively in an oxygen enriched helium atmosphere. The analysis substance was disintegrated oxidatively at 950 °C. During combustion the elements C, N, molecular N, S and H were oxidized to CO_2, H_2O, NO, NO_2, SO_2, SO_3 and volatile halogen compounds. Nitrogen oxides and SO_3 were reduced to molecular N and SO_2 in a Cu filled reduction pipe at 850 °C. H_2O was removed in a contiguous dry pipe. Interfering halogen compounds are absorbed by silver wool and extracted from the gas current. Thus only H, CO_2, SO_2 and N_2 reach the succeeding separation and analysing system. Gaschromatographic separation columns separate the individual components, which are then subsequently analysed in the heated columns with a heat conduction detector.

The total carbon content (TC) of a rock comprises the total organic carbon fraction (TOC) and total inorganic carbon fraction (TIC). All samples are predominantly made up of quartz and clay, probably devoid of considerable TIC, except sample S7. Moreover, no carbonate was detected to be significant for further calculations. Thus decarbonisation was not implemented and TC measurements were considered to reflect the TOC content of the sampled shale in sufficient accuracy.

Chapter 7 Petrography and geochemistry of the glacio-marine Dwyka shale

Petrographical and geochemical examinations of siliciclastic sediments support the development of a palaeoecological model. Subsequently, data from microscopy, XRD and XRF are used to obtain information about the mineralogical constituents and the conditions during deposition.

7.1 Microscopy

Microscopic to sub-microscopic mineral appearance within the very fine-grained shale samples also hampered satisfying microscopic analyses, so that a concretionary nodule between tuff horizon VI and VII provided best results. This exemplary thin-section (Figure 22) shows microscopic grains of less than 5 µm and classifies it structurally as pelite. Poorly rounded grains, up to 15 µm in diameter, with straight grain boundaries show uniform extinction with typical quartz interference colours. Some shale layers contain layers of calcite filled spheres, a few mm thick and up to 500 µm across, boundaries of which are sutured. The polycrystalline calcite filling shows high-order pink and green interference colours and is devoid of preferential internal structures. The origin of these calcite-filled spheres is not yet understood. Often, about 10 µm opaque minerals, which were determined to be pyrite based on microscopic observations, accompany the calcite filled spheres or even replace the calcite almost completely. They are connected to lath-shaped and cuspate opaque minerals, up to 150 µm long but only about 10 µm wide, which disseminate throughout the shale matrix.

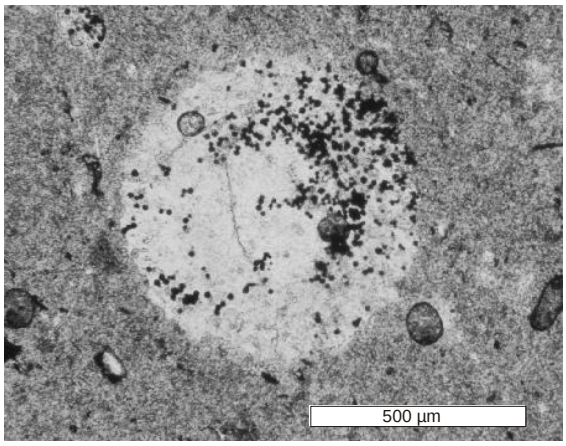

Figure 22: Photomicrograph of a thin-section of a concretionary nodule from the Dwyka shale at Zwartbas (tuff beds VI to VII). A calcite filled sphere with disseminated ore spots is surrounded by clay minerals.

7.2 XRD analysis of the basal shale

A stratigraphic series of XRD-measurements of the lower section of the Dwyka Group shows a relatively continuous petrographical composition, which mainly follows the typical shale mineralogy with illite (hydro-muscovite), chlorite, quartz, feldspar and sporadically sulphide (Bucher and Frey, 1994). Chapter 8.2.2 informs about mineral recognition by XRD in a more detailed way.

The measured sample series with the stratigraphic sample distance of about 8 m is the basis for the diagrams of Figure 23. The most dominant peak-set belongs to the quartz reflection, along with well developed illite and feldspar (albite) peaks. The K-mica illite is a significant rock-forming mineral being a main component of shales and other argillaceous rocks. Minor peaks at low degrees infer the presence of chlorite. According to Heinrich (1991), illite and chlorite constituting the main clay fraction, concomitant with the sporadic occurrence of ice rafted debris, are typical indicators for a transitional facies between a glacial and an interglacial period. An obvious discrepancy between distinct tuff beds solely appears as different chlorite intensities, with a considerable intensity loss in samples S09, S17, S21 and S29. Sample S25 probably comprises a supplementary content of smectite. Due to the smectite proportion in sample S25, the onset of a glacial period can be considered

(Heinrich, 1991). Generally the slight differences in clay mineral abundance can be caused by the additional deposition of other primary minerals, such as K-feldspar, or by different decomposition during diagenesis and alteration.

For its extraordinary consistency known from the XRF measurements, sample S7 was analysed although it was not part of the selected sample series. The XRD reconfirmed the presence of carbonate but specified dolomite. Due to the unique occurrence of dolomite there, along with other calcite-rich layers (especially the diamictites), a late-diagenetic formation was declined. On the contrary, carbonate deposition and early-diagenetic dolomitisation implies an increased salinity, which is also suggested by the Rb/K ratio (Chapter 7.5).

7.3 XRF analysis of the basal shale

The chemistry of sediments is not only dependent on the source rock but is widely influenced by the sedimentary environment (Schmid-Röhl, 1999). Together with the element analysis (Chapter 7.4), the XRF analyses give a wide range of chemical data, which allow a conclusion on the palaeo-sedimentary environment.

7.3.1 Major elements

The major element concentrations are more or less constant throughout the sampled glacio-marine shale succession (Table 3) and correspond with the geochemical fingerprint of pelites (pelagic clays), in accordance with Carmichael (1989). Based on his classification, only sample S7 is an exception for platform shales because of a LOI (loss on ignition) of more than 10 wt%, along with a loss of SiO_2 and a synchronous gain of CaO and MnO. Further, sample S7 has the highest concentrations of almost all other major elements. Interesting deviations in major element concentrations are found in the tillite samples of the Yellow Basal Tillite (DA and DB) and from the Goats Cliff Diamictite (DC). While all other major elements are equal or depleted relative to the shale mean, CaO, MnO and P_2O_5 concentrations are highly increased.

7.3.2 Trace elements

Trace element concentrations within individual samples of the glacio-marine shale are commonly consistent with one another. Only sample S7 differs from the mean with considerable high concentrations of almost all trace elements (see Table 3). Suspicious deviations are shown in the tillite samples DA, DB and DC, as theses samples show a loss in V, Zn, Rb, Nb, Th and Zr but a gain in Sr. Furthermore, the tillites are low in Ba, except in sample DC, and rich in U, except in sample DA. The anomalous trace element behaviour of the diamictites reflects their extraordinary stratigraphic status and distinguishes them from the common shales.

7.4 Element analysis

Element analyses of several shale samples produced a continuous sample log of total organic carbon (TOC) and nitrogen from the base of the Dwyka Group to the top of the highly fossiliferous lower half of the examined succession. Together with sulphur concentrations from XRF measurements, these elements offer useful information about the palaeoecology. The following interpretation of these measurements are based on Schmid-Röhl (1999) and references therein.

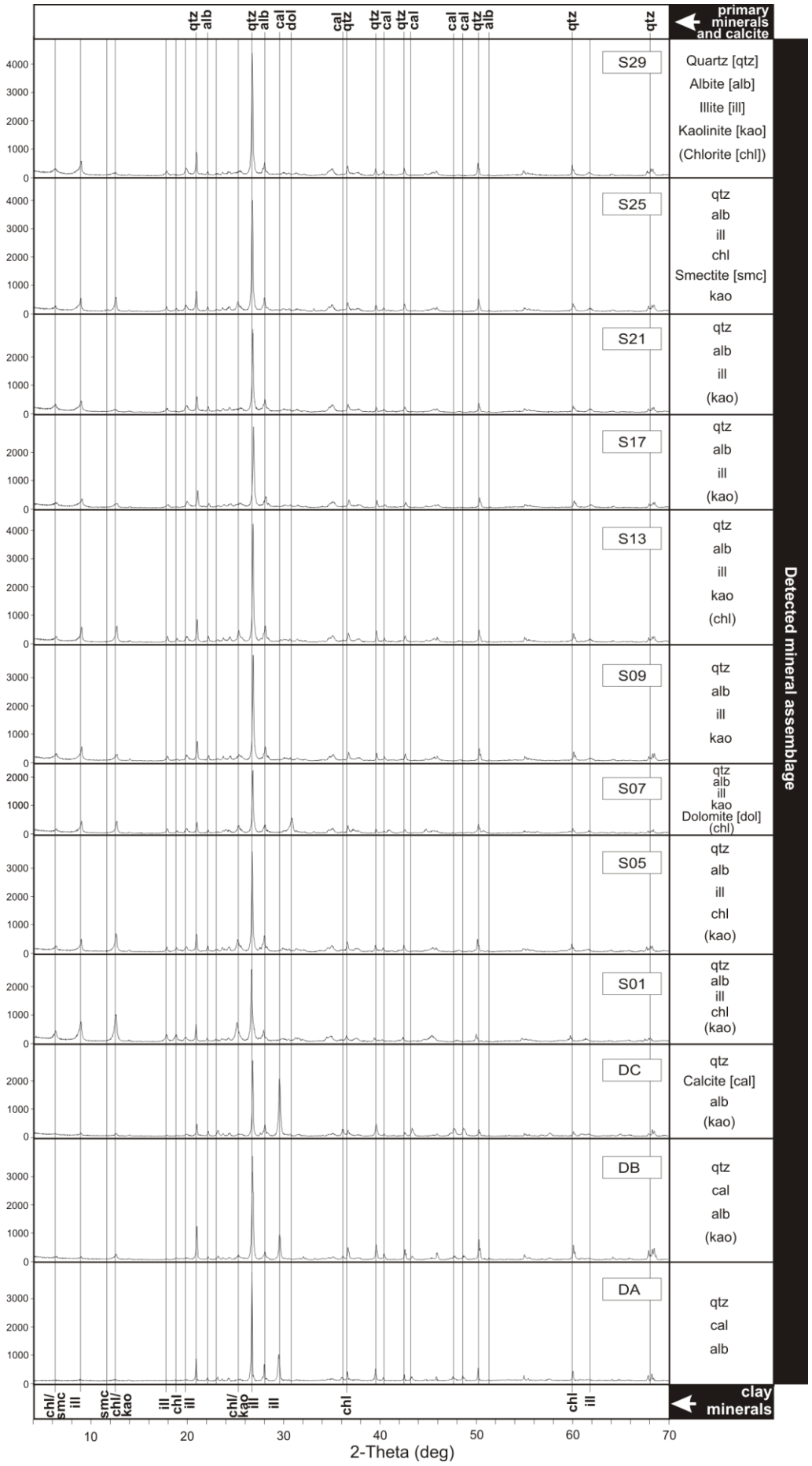

Figure 23: XRD diagrams of representative samples series of the basal Dwyka shale at Zwartbas show overall similar petrographical composition. For further explanation see text.

7.4.1 Carbon

Two processes lead to increased TOC concentrations in subaqueous sediments: (1) Increased primary production and subsequently (2) oxygen deficiency in the water column and at the bottom. This 'anoxia versus productivity'-problem is frequently debated (cf. Wetzel (1991)). Earlier considerations suggested that in stagnant water bodies, apart from anoxic bottom conditions, primary production is limited by nutrient loss due to the failed circulation. Recent studies, however, showed that phosphor can be recycled much more effectively under anoxic conditions than under oxic ones, because under anoxic conditions bacteria store P in a very restricted manner. Thus, a coexistence of anoxia and at least a restricted primary production in a stagnating basin may be possible. Moreover, nutrients may be brought in during a transgression or by rivers.

	S1	S3	S5	S7	S9	S11	S13	S15	S17	S19	S21	S23	S25	S27	S29	S31	DA	DB	DC
SiO_2	58.68	72.16	60.73	47.22	62.57	62.41	62.89	62.16	60.72	62.93	58.51	59.58	61.41	64.29	64.65	60.57	53.89	64.61	37.62
TiO_2	0.91	0.65	0.81	0.68	0.79	0.76	0.73	0.71	0.76	0.68	0.77	0.66	0.68	0.70	0.71	0.68	0.4	0.32	0.39
Al_2O_3	21.28	11.92	16.92	15.48	17.08	16.67	16.63	17.12	17.71	17.19	18.79	17.15	16.65	17.28	17.96	16.85	8.56	7.16	8.04
Fe_2O_3	9.09	5.52	7.53	8.14	6.18	6.55	5.83	6.51	6.40	5.73	6.92	6.49	6.24	4.46	5.18	6.36	4.87	4.55	5.64
MnO	0.06	0.05	0.08	2.31	0.05	0.08	0.08	0.06	0.08	0.09	0.19	0.08	0.08	0.06	0.03	0.06	0.55	0.61	0.66
MgO	3.88	2.06	3.08	3.39	2.29	2.85	2.55	2.87	2.30	2.51	2.33	2.55	2.48	2.16	2.13	2.34	1.54	1.84	1.21
CaO	0.41	0.38	0.51	5.56	0.43	0.62	0.67	0.43	0.47	0.32	0.55	0.62	0.62	0.38	0.48	0.59	14.14	9.32	23.09
Na_2O	1.35	2.19	1.79	1.09	1.57	1.92	1.78	1.62	1.36	1.35	1.48	1.54	1.40	1.37	1.22	1.42	1.58	0.84	1.52
K_2O	4.96	2.03	3.43	3.42	3.61	3.24	3.55	3.58	3.72	3.72	4.12	3.50	3.37	3.68	3.80	3.35	1.12	0.89	1.36
P_2O_5	0.16	0.15	0.13	0.13	0.11	0.13	0.11	0.11	0.11	0.08	0.10	0.11	0.14	0.08	0.09	0.15	0.12	0.94	0.21
N*)	0.11	0.03	0.09	-	0.13	0.11	0.11	0.12	0.14	0.14	0.15	0.15	0.15	0.16	0.16	0.16	-	-	-
TOC*)	0.27	0.19	0.54	-	0.67	0.79	0.73	0.80	0.95	0.68	0.65	1.09	1.13	0.92	0.53	1.48	-	-	-
S	<0.02	<0.02	<0.02	0.76	<0.02	<0.02	0.03	0.03	<0.02	<0.02	<0.02	0.54	0.45	0.10	<0.02	0.44	<0.02	<0.02	0.04
SUM	100.78	97.11	95.01	88.18	94.68	95.23	94.85	95.20	93.63	94.60	93.76	92.82	93.52	94.56	96.25	92.81	86.77	91.08	79.74
LOI	4.98	2.49	4.61	12.88	4.96	4.69	4.49	4.73	5.81	4.83	5.73	6.08	6.02	5.04	5.16	5.96	13.03	8.36	20.00
Nb	18	11	17	62	15	16	15	16	15	17	16	15	16	17	20	15	<5	6	6
Zr	185	138	165	172	184	171	206	164	166	168	162	156	183	180	190	174	136	146	101
Y	30	26	30	40	26	31	35	29	34	34	33	35	41	33	41	37	41	66	31
Sr	54	58	79	261	73	75	92	71	72	65	81	109	91	79	79	83	233	141	320
Rb	232	77	143	160	169	142	161	162	180	179	196	164	162	182	186	163	49	41	57
Pb	25	13	16	34	22	20	22	16	16	23	22	28	21	14	12	30	19	36	13
Ga	32	17	29	22	24	31	26	21	24	15	34	24	23	23	17	26	15	14	13
Zn	155	76	108	167	118	116	102	101	152	134	158	173	188	184	151	235	68	68	56
Ni	56	26	43	62	28	43	28	31	25	26	45	67	49	32	18	55	35	12	23
Co	23	<10	17	28	<10	22	12	15	<10	11	18	22	13	<10	<10	15	15	<10	<10
Cr	126	68	97	84	93	87	70	76	69	67	78	63	70	74	85	67	68	40	65
V	156	84	157	172	151	153	124	146	161	116	136	139	134	132	124	132	73	42	87
Ba	809	422	614	624	638	577	620	657	702	688	784	658	597	686	736	651	289	304	596
Sc	23	10	14	19	13	21	10	12	18	14	16	14	14	15	14	15	11	10	15
Mo	<5	<5	<5	29	<5	<5	<5	<5	<5	<5	<5	<5	<5	<5	<5	<5	<5	<5	<5
Th	21	8	16	15	11	14	18	16	13	13	16	14	13	14	13	11	10	7	8
U	10	<5	<5	11	<5	<5	<5	<5	<5	<5	<5	<5	<5	<5	<5	<5	<5	11	13
Sn	<15	<15	<15	<15	<15	<15	<15	<15	<15	<15	16	<15	<15	<15	<15	<15	<15	<15	<15

Table 3: Geochemical analyses of shale samples from the basal Dwyka Group at Zwartbas. Stratigraphic propagation (upwards in approx. 2 m intervals): S1 (base) to S31 (62 m above base). DA and DB are samples from the Basal Yellow Tillite, DC from the Goats Cliff Diamictite. The values are not normalised.
*) Values from the element analysis (Chapter 7.4); they are not included in SUM.

Anoxic conditions, however, were discovered to have bacterial decay rates similar to oxic conditions. Thus, TOC-spectra of aerobic (TOC <2.5 %), dysaerobic (1 to 10.5 % TOC) and anaerobic (1.5 to 17.6 % TOC) environments overlap widely. In the shales of the Dwyka Group at Zwartbas, concentrations of usually less than 1 % but never more than 1.5 % TOC (Table 3) point to aerobic or

dysaerobic conditions during the deposition of the shale. Wetzel (1991) used TOC contents to determine black shales. Apart from the dark colour, which is due to the presence of finely dispersed iron sulfides, organic matter content in black shales normally exceeds 0.2 to 0.5 wt% (cf. Table 3).

The quite low TOC concentrations at the very base of the succession, however, indicate a well-oxygenated environment, which corresponds to the lithological considerations of subaerial or at least continental sub- and/or proglacial conditions (Figure 24). Increased carbonate deposition at the top of the investigated succession is rejected due to the unchanged concentrations of carbonate cations.

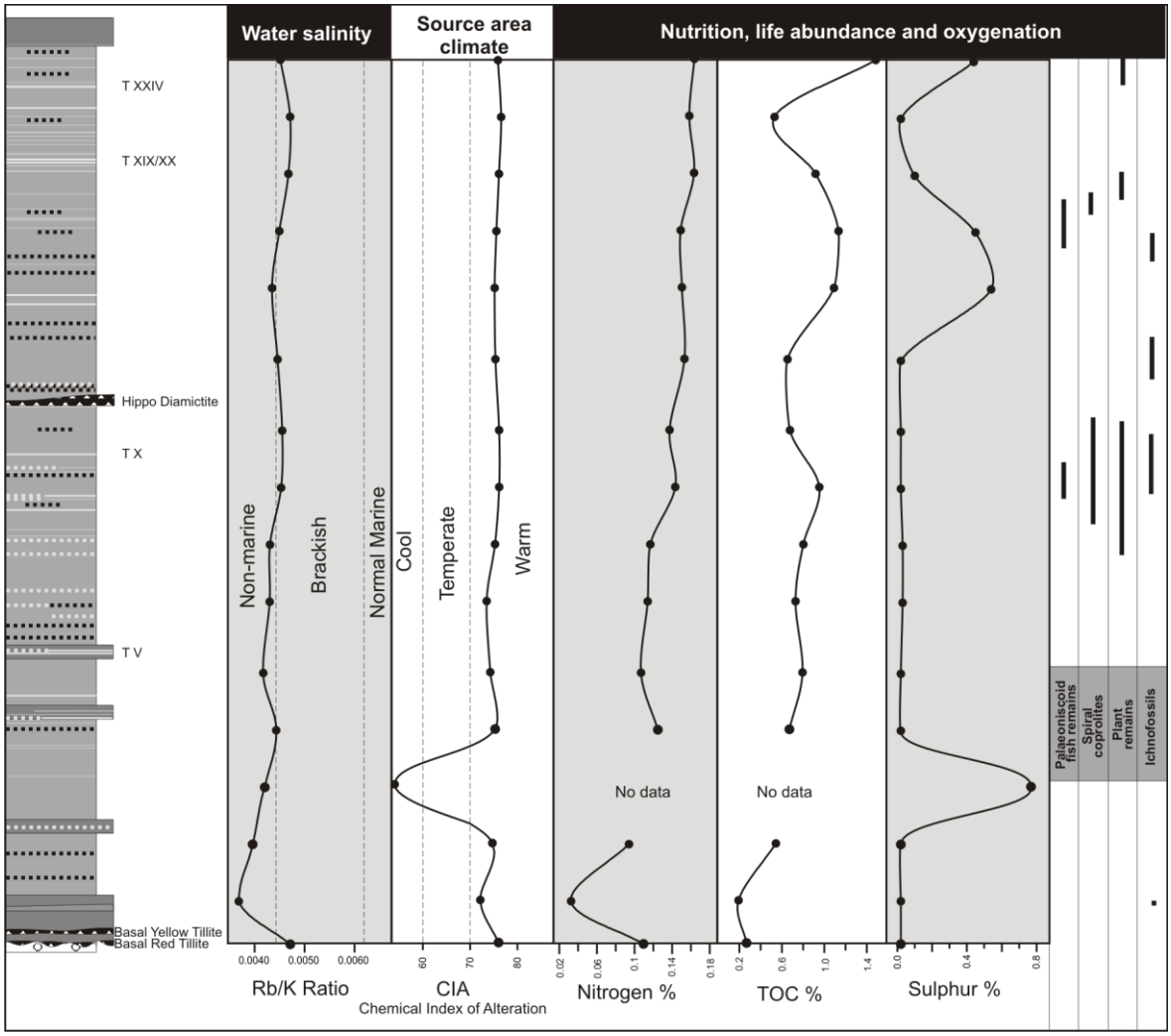

Figure 24: Log of the basal Dwyka at Zwartbas with corresponding geochemical and palaeontological data. Interpretation of the Rb/K ratios after Campbell and Williams (1965), the Chemical Index of Alteration (CIA) of Nesbitt and Young (1982) and fossil range zones from Geiger (1999).

7.4.2 Nitrogen

Nitrogen concentrations of the Dwyka shales at Zwartbas vary from 0.03 to 0.16 % (Table 3). N and TOC values show an almost similar behaviour in the entire examined succession (Figure 24). This confirms the connection of the total N to the organic matter and thus points to a predominant organic origin of the carbon. A correlative course of concentration shows sulphur (Figure 24), which is an additional indicator for eutrophy.

7.5 Chemical implications of geotectonic setting and palaeoenvironment

Geochemical results of the XRF analyses on the shales were used to estimate the tectonic setting of the depository, the provenance of the deposits and the palaeosalinity during the deposition.

An overview of possible applications of geochemical data on sedimentary rocks is listed in Rollinson (1993). These applications mainly discriminate the tectonic setting of the depository and the provenance of the deposited material. Although several attempts were made for a widely applicative discrimination, too many variables must be considered in order to establish an universal method. Nevertheless, there are techniques that use geochemical data to determine the salinity of the water body during the deposition in sufficient precision.

7.5.1 Discrimination diagram for the tectonic setting

The K_2O/Na_2O vs. SiO_2 diagram of Roser and Korsch (1986) distinguishes three tectonic settings: the Passive Continental Margin, the Active Continental Margin and the Oceanic Island-Arc. The discriminative fields are based on chemical analyses of ancient sediments compared with inferred tectonic setting from literature. Figure 25points to a situation at a passive to active continental margin for Zwartbas in Dwyka times.

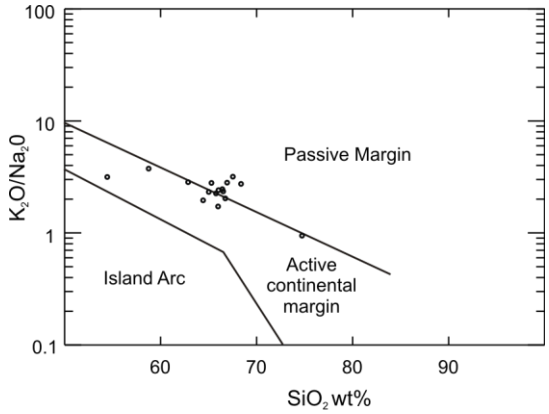

Figure 25: Tectonic setting discrimination of fine-grained sediments according to Roser and Korsch (1986).

Taking into account the lack of a suitable discrimination method for fine-grained sediments, this diagram provides a starting point for the tectonic characterisation of the studied region, but it must be interpreted cautiously. Moreover, the glacial influence might have overprinted the tectonic signature of the source-area/depositional environment. The plot of Figure 25 possibly reflects the transition from an active continental margin into a passive continental margin or at least the tendency of an early break-up (Chapter 2.2).

7.5.2 Determination of the palaeosedimentary environment

In sediments laid down in fresh water, individual element concentration ratios differ from analogous marine sediments. Thus, element analyses can be used to classify sedimentary rocks, source area and palaeosalinity, but they scarcely approach the quality of the one achieved through the use of fossils. Many methods have their weaknesses, including analytical problems, due to a loss of the original composition during diagenesis and the lack of compositional control by a single salinity-dependent process. Further, the application of methods is often limited to specific maximum or minimum ranges of the used elements, and therefore their implementation in certain cases needs discussion.

7.5.2.1 Carbonate precipitation as palaeoenvironmental indicator

Shallow seas become much more easily saline than regions of deep-water. Thus salinity can be used as a criterion to distinguish shallow water platform shales from deepwater pelites. Exceptional amounts of Ca in sample S7 (just below tuff bed I) in the XRF results were confirmed by XRD control analysis. The XRD suggests abundant carbonate (dolomite) within sample S7 (Figure 23). The dolomite formation indicates the carbonate as the primary sediment, which has undergone an early-diagenetic transformation to dolomite (cf. Chapter 7.2). In order to deposit carbonate and to enable

dolomitisation, a significant amount of salinity is required. This implies, along with corresponding Rb/K ratios and increased sulphur content, a temporary change into a higher salinity at the stratigraphic position of sample S7.

7.5.2.2 The Rb/K ratio of Campbell and Lerbekmo (1963)

Through geochemical analyses on continental and marine shales of the Lower Cretaceous Manville Group of central Alberta (Canada), Campbell and Lerbekmo (1963) recognised a correlative behaviour between Rb/K ratios in marine and non-marine sedimentary conditions. A genetic explanation for behaviour of the Rb/K ratio under marine and non-marine conditions was not considered. Visser and Young (1990) proved the applicability of the Rb/K ratio on Karoo mudstones in South Africa by transforming the determined mean ratios of Campbell and Williams (1965) to a discriminative rule. Figure 24 indicates prevailing brackish to freshwater conditions throughout the sampled succession.

7.5.2.3 The Mn/Fe ratio of Frakes and Crowell (1975)

The sedimentary environments of marine and non-marine deposits as well as the glacial impact during their deposition vary considerably and lead to differences in sediment chemistry. Frakes (1985) and Frakes and Crowell (1975) introduced a method to distinguish subglacial from subaqueous glacio-marine sediments and noted the possible application in distinguishing marine from non-marine glacial deposits. Visser (1989) applied this method to Dwyka shales in South Africa and found it sufficiently reliable. The discrimination takes into account that Fe and Mn are easily precipitated from solution in the presence of oxygen, particularly in land-based glacial environments, but depleted in many (glacio-)marine environments due to the absence of oxygen. Oxygen depletion is caused by an excess in productivity of surface microplankton followed by high oxygen consumption during decomposition of the organic matter.

Fundamental for the Mn/Fe method is the assumption that detrital Fe derived by glacial erosion is deposited in a basin in a similar proportion to its abundance in the source area. In glaciated regions, detrital Fe approximates its crustal abundance of about 5.6 % on average. Glacio-marine sediments, however, appear to be depleted in Fe (and Mn) and represent proportions less than crustal abundance. This loss in Fe is caused by unoxidized dissolved Fe, which bypasses shallow marine environments and is transported to the deep ocean. To attain this situation, a deposition of the glacio-marine sediments presumably took place in a proximal (i.e. shelf) setting. A similar result occurs through diagenetic remobilization of Fe (and Mn) in reduced sediment layers.

At Zwartbas, the abundant occurrences of fossilised organic material (see Chapter 5) and pyrite implies a pronounced oxygen deficiency during the deposition of the shale, even though the Fe proportion exceeds the crustal average. However, Mn values relatively low as expected in a glaciomarine environment, whereas in a distal situation Mn and Fe should approximate the crustal concentration. A clear Mn loss in crustal abundance relative to Fe prohibits the conclusion of a distal marine situation. Fe absorption in pyrite formation under saline conditions is improbable because of much too small sulphur concentrations. The high Fe concentrations, furthermore, contradict a diagenetic Fe depletion (Figure 26). The abundant Fe in the Zwartbas shales therefore implies a non-marine environment.

Additional questions arise from the chemistry of the diamictites, which were assumed to be tillites. Both the Basal Tillite (sample DA and DB) and the Goats Cliff Diamictite (sample DC) show a relative loss of Fe but a gain in Mn (Table 2). According to Frakes (1985) these values point to glacio-marine conditions with abnormally high Mn concentrations. These results infer a subglacial glacio-marine environment with a stagnate water body located underneath a floating ice shield. Although the results are contradictory, the deviation in major and trace element concentrations distinguishes clearly the presumed tillites (samples DA, DB and DC) from the glacio-marine shales.

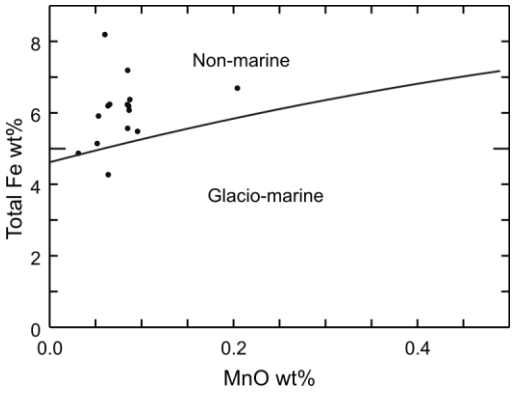

Figure 26: Fe-Mn discrimination diagram of Frakes (1985) and Visser (1989) illustrates the palaeosalinity during the deposition of the Dwyka shales at Zwartbas by distinguishing glacio-marine conditions from non-marine conditions.

7.5.2.4 The C/S ratio of Berner and Raiswell (1984)

Organic-rich sediments deposited in freshwater are lacking in pyrite in comparison to analogous marine sediments. Using this basic assumption together with published chemical analyses, Berner and Raiswell (1984) developed a method to determine whether a sediment was deposited in freshwater or saline sea water. The C/S method for distinguishing freshwater from marine sedimentary rocks is based on the process of sedimentary pyrite formation. At an early stage of diagenesis, pyrite forms from the reaction of H_2S with detrital iron minerals. The H_2S, in turn, is derived from bacterial reduction of dissolved sulphate, contributed from the overlying water. This process is associated with oxidation of organic matter buried in the sediment. Sulphate reduction proceeds only under anoxic conditions, i.e. only below the sediment-water interface in most sediments, and can be described by the reaction: $2CH_2O + SO_4^{2-} \rightarrow H_2S + 2HCO_3^-$. Three major factors limit the amount of pyrite, which can form in a sediment: (1) the deposition of bacterially decomposable organic matter, (2) the sulphate concentration in the overlying water and (3) the availability of iron minerals that can react with H_2S to form pyrite. The more organic matter and dissolved sulphate is present, the more H_2S forms through a decrease in carbon. H_2S eventually reacts with iron to produce sedimentary pyrite. Thus, the main variable controlling the evolution of the C/S ratio is the formation of pyrite. Although only total sulphur analyses were available for this study, they were considered appropriate, because the total sulphur is insignificantly small in comparison to the limit for marine conditions (Figure 27).

Marine sediments provide enough dissolved sulphate so that it is rarely a limiting factor in pyrite formation. Seawater contains 28 mmol/L SO_4^{2-} on average, while fresh water contains less than 1 % of the concentrations found in oceans, simply due to their considerably lower salinity. Consequently, low sulphate concentrations in fresh water sediments limit pyrite formation during the early diagenesis and contemporaneously the decay of organic matter. As a result, freshwater sediments contain abundant organic matter and detrital iron minerals and show much lower sulphur concentrations in pyrite than their high-sulphate marine counterparts.

Although the application of the C/S method demands a minimum C content of 1 wt% to avoid inaccurate interpretation by overlapping marine and non-marine fields at such low quantities, it is used here due to the strong congruency of the C/S method with different methods. Nevertheless, the result should be considered cautiously.

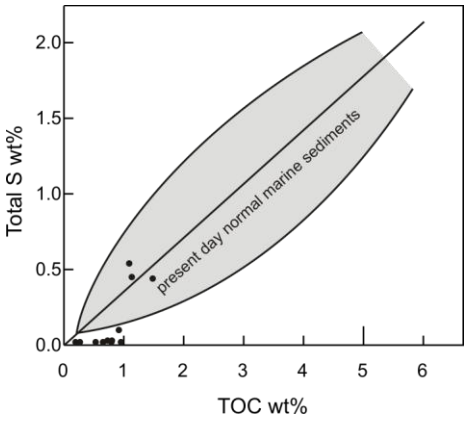

Figure 27: Plot of total sulphur (as an approximation of pyrite sulphur) versus total organic carbon (TOC) for the basal Dwyka shales at Zwartbas. The grey field marks present-day normal marine sediments (from Berner and Raiswell (1984)).

Figure 27 depicts that shale with low sulphur concentrations plots into the non-marine field close to the TOC-axis, whereas some samples from the upper shale succession plot within the central part of the marine field. This infers an increase in salinity with time.

7.5.2.5 Palaeoenvironmental determinations of the hinterland

Rock decomposition is largely dependent on the prevailing climate. A warm and humid weather strongly accelerates the decay of the minerals, whereas the susceptibility to weathering of particular minerals widely differs. Feldspar, for example, and most of the rock forming minerals alter much more easily during weathering than quartz. Clay minerals, formed from these rock forming minerals by alteration, generally have a gain in Al_2O_3, while CaO, Na_2O and K_2O are depleted.

Nesbitt and Young (1982) used the ratio between Al_2O_3 and the sum of Al_2O_3, CaO, Na_2O and K_2O to estimate the quality of alteration and introduced this ratio as **C**hemical **I**ndex of **A**lteration (CIA). Visser and Young (1990) assumed that marine sediments retain the CIA they have obtained at their source. Conclusively, the CIA in sediments reflects the grade of alteration of the source rock and thus the climate in the source area. Taking this into account, Visser and Young (1990) classified CIA ranges to distinct climatic conditions in the source area and found this method suitable, when they applied it to Karoo aged shales in the Main Karoo Basin.

Using Visser and Young's classification to the shale succession at Zwartbas, the CIA of most of the samples surprisingly plots into the field that indicates a warm climate in the source area (Figure 24). This corresponds to observations in Dwyka aged shales in South Africa (Visser and Young, 1990).

Chapter 8 Petrography of the tephrostratigraphic marker beds

Macroscopic inspections of the very fine-grained distal ash tuffs are generally inconclusive. Individual components are too small or too highly altered to be visible to the naked eye. To determine the petrographical composition of the tuffs, microscopic and X-ray diffraction (XRD) studies were carried out. The possibility of taking geochemical measurements (electron microprobe) on glass inclusions in apatite and zircon were rejected after discussion with U. Schüssler (Institut für Mineralogie of the Universität Würzburg) because of the small size and number of the inclusions. General examinations of heavy minerals were carried out on thin-sections and grain mounts. The thin-section analysis of tuff layers was restricted due to the very difficult sampling because of high fissility and small thickness. In only one sample, tuff bed VIIIb, a thin-section could be produced properly to provide textural information. Therefore the following exemplary optical description is based on this tuff bed.

The tuff beds mainly consist of smectite-illite clay minerals, sporadically containing kaolinite booklets caused by an intensive alteration of the primary probably glassy to micro- to cryptocrystalline quartz-feldspar mixture. Nevertheless, their volcanic derivation is still recorded by the presence of juvenile quartz and plagioclase crystal fragments, along with a heavy mineral suite mainly including juvenile zircons and apatites. Platy volcanic glass shards and pumice, which commonly confirm a pyroclastic origin, were not detected. This is consistent with the observations of Bangert et al. (2000) in previous studies on equivalent bentonites in the Aranos Basin. Detrital crystals have apparently not confused the mineral suite, since the heavy minerals are commonly euhedral and without abrasion marks. Moreover, the adjacent shale is devoid of crystals of equivalent size, so that a significant admixture of sedimentary crystals by background sedimentation can be disregarded.

8.1 Textural and structural outlines

Microscopic studies of tuff bed VIIIb show a fragmental texture typical of juvenile ash-fall deposits preserved in the phenocryst relicts, while the surrounding matrix mainly consists of clay minerals derived from altered glassy to micro- to crypto-crystalline primary matrix. The phenocrysts make up approximately less than 15 % of the total rock within the matrix supported bed. Within the phenocrysts about 60 % are quartz crystals and crystal fragments, 35 % are ash particles and less than 5 % are plagioclase (Chapter 8.2.2). Furthermore, less than 1 % of secondary accessory minerals, e.g. kaolinite booklets, opaque minerals and iron hydroxide occur.

The studied bentonites are assumed to constitute a single volcanic event and were deposited in a short time span (cf. Chapter 4.2 and 4.1). Thin-sections of tuff bed VIIIb show a continuously graded bed, about 1.5 cm thick, with a conspicuous upward decrease in the grain size and number. At the base of the bed the largest components are predominantly 60 to 80 µm, fining upward to a maximum of 20 µm.

About 20 to 150 µm thick micro-fractures extend horizontally through the tuff bed, generally parallel but partly oblique to the bedding. These fractures are frequently occupied by secondary mineralisations, commonly gypsum and opaque minerals.

Slight layering within the clay matrix outlines condensed layering above and below enveloped quartz minerals, with expanded layers joining the minerals on both sides. Elongated quartz grains and splinters frequently outline this layering.

8.2 Primary volcanic components

In general, quartz is the most common primary mineral present in tonstein and bentonites respectively (Bohor and Triplehorn, 1993). Other potential felsic juvenile components, such as relicts of glass shards, feldspars, pyroxene, amphibole, heavy minerals and pyroclastic particles (Fischer and Schmincke, 1984), generally immerse into the abundant clay matrix, which mainly consists of a

micro- to cryptocrystalline quartz-feldspar mixture. In this study, exclusively ash, feldspar and heavy minerals were confidentially recognised in addition to the commonly abundant quartz. Heavy minerals were examined in several distinct beds by grain mount studies. Taking into account their correlation significance, they are treated in Chapter 8.3 in more detail.

8.2.1 Microscopy

As mentioned above, only one thin-section of tuff bed VIIIb could be successfully prepared. Due to the uniform facies and similar exposure to weathering of most of the beds, the thin-section of tuff VIIIb provides an exemplary description.

8.2.1.1 Major juvenile minerals

The largest and most abundant juvenile crystals in the examined tuff beds are colourless monocrystalline volcanic quartz grains. They either occur as sharply angular isometric subhedral grains, up to 80 µm in diameter, or as up to 100 µm long but often less than 20 µm thick splinter and thorn-shaped to cuspate crystal fragments. Within the quartz no inclusions were recognised. The triangular shape of some quartz splinters were typically produced during eruptions. Physical strain during eruptions is also responsible for the occasionally slightly undulatory extinction of the grey interference colours under crossed polars (Figure 28). Quartz probably constitutes 1 % of the total mode in the thin-section.

The second most abundant juvenile crystals in the thin-section are feldspars, although they are very rare in relation to the whole rock. The presence of a few marginally corroded, isometric grains of plagioclase with slight polysynthetic twinning is confirmed by XRD (Chapter 8.2.2). Reaction rims with secondary iron hydroxide formation are common. Feldspar, with an estimated modal percentage of less than 0.1 %, can be proportionally equated with the heavy minerals.

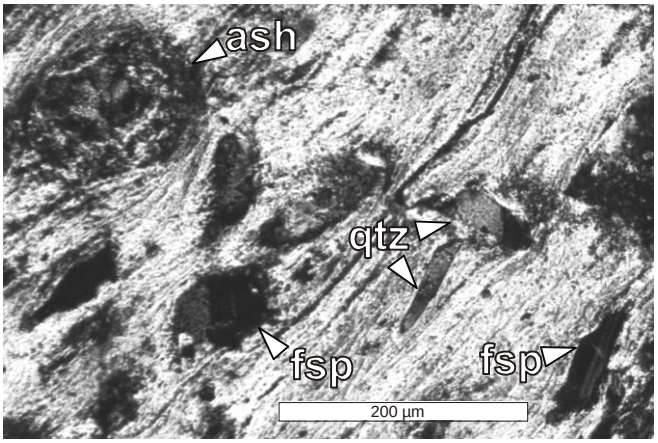

Figure 28: Thin-section microphotograph of tuff bed VIIIb under crossed nicols. Typical quartz splinter (qtz) and feldspar crystal fragments (fsp). Pyroclastic ash accretions of small mineral and glass fragments are common (ash).

8.2.1.2 Pyroclasts

Inconspicuous but common components are spherical pyroclastic mineral and glass accretions, usually 60 to 80 µm and maximum 100 µm, with no internal structure and texture (Figure 28). They probably consist mainly of volcanic glass. The individual clasts are mostly sub-microscopic. Their mode of total rock is less than about 0.1 % of the whole rock.

8.2.2 XRD analysis

XRD diagrams of representative qualitative analyses of distinct tuff beds show varying detection intensities of particular minerals (for an overview see Figure 29). The XRD results suggest that there

is no change of the mineralogical composition throughout the succession, except the suspicious loss of quartz in tuff bed XXIVa-1 and XXXIV. Moreover, albite, as common representative of the plagioclase group, was detected in all tuff beds, except the lowest (IIIb-2) and the highest (XXXIV).

8.3 Heavy minerals

Minerals with a specific gravity higher than 2.90 $g \cdot cm^{-3}$ are commonly denoted as heavy minerals (Boenigk, 1983). Besides their occurrence as accessory constituents in sedimentary rocks, they are common in crystalline source rock, where they cover a wide spectrum (65 to 200 µm). Most abundant heavy minerals, which can be found in acid igneous rocks, are apatite, biotite, brookite, hornblende, monazite, muscovite, rutile, sphene, tourmaline and zircon (Königer, 1999). Basic igneous rocks, in contrast, contain mainly augite, diopsid, hypersthene, olivine, spinell and opaque minerals. Moreover, sediments produced by crystalline rocks typically contain heavy minerals, but transport and alteration commonly lead to rounded minerals and compositional changes due to selective mineral solution as well as to the formation of authigenic minerals. Thus, heavy minerals, especially peculiar varieties and proportions are diagnostic for primary rock types, source area determinations and lithostratigraphic correlation.

For bentonites in particular, the interpretative value of heavy minerals was suggested by Weaver (1963) to determine whether the bentonites were of primary volcanic, secondary (redeposited) volcanic, or non-volcanic origin. He presumed that the heavy mineral suite of most primary bentonites, which are derived from acid to intermediate igneous rocks, are depleted in biotite, zircon, apatite and sometimes sphene. Bohor and Triplehorn (1993), however, outlined doubtful compositional aspects in Weaver's studies. They revised the indicative compositions and found traces of euhedral tourmaline, pink garnet and topaz more useful as distinctive criteria. Opaque heavy minerals are exclusively weathering products of iron-bearing minerals.

In order to use heavy-mineral studies for correlation purposes, the change in mineralogical composition through aeolian fractionation (cf. Chapter 4.1) and contamination must be considered. The assimilation and entrainment of xenocrysts from the country rock in the magma chamber and during the eruption as well as sedimentary admixing of detrital minerals and the formation of authigenic minerals are potential mechanisms of such a contamination.

Bangert et al. (1998), Bangert et al. (1999) and Stollhofen (1999) noted that Carboniferous-Permian ash-fall tuffs in southern Africa mainly comprise juvenile zircon and apatite with minor amounts of monazite, sphene (titanite), rutile and secondary sulphates (e.g. baryte) as non-opaque heavy minerals. Clearly redeposited detrital minerals are rather rare.

At Zwartbas, only three (IIIb-3, XIX and XXIVa-3) in ten sampled tuff beds produced useful grain mounts, while the other seven beds reveal only few or no heavy minerals (VII, VIIIb, X, XIII, XVIIId, XIX, XXIc, XXXIV). At Zwartbas, only zircon, apatite, biotite and monazite were recognised to form the juvenile heavy-mineral suite, along with rare secondary baryte, heavy clay minerals (illite, chlorite) and secondary opaque minerals. The following heavy mineral petrography is based on comparative examinations of the tuff beds IIIb, XIX and XXIVa. Interpretations are based on the comprehensive work of Königer (1999) and references therein unless noted otherwise.

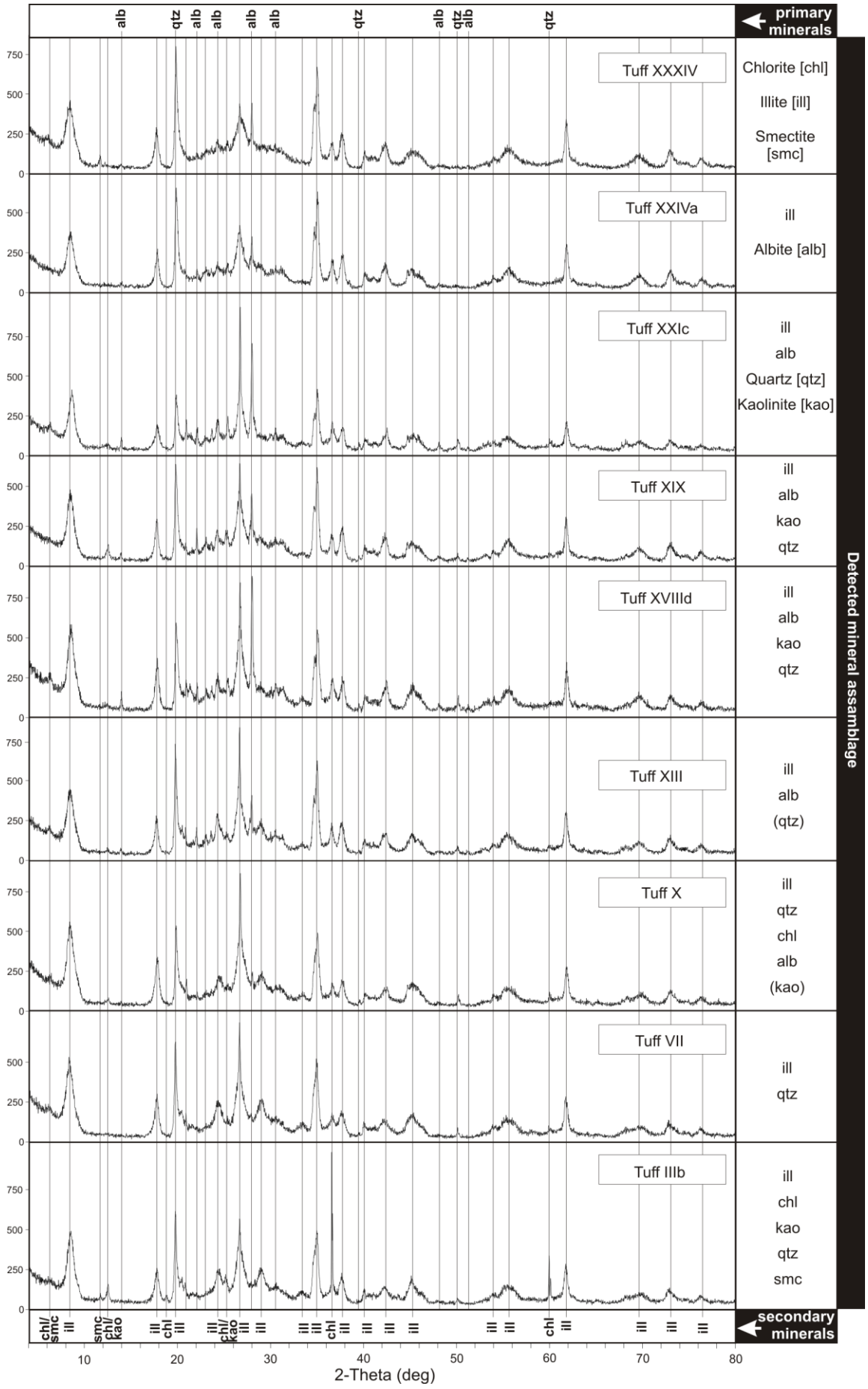

Figure 29: Assemblage of XRD diagrams of distinct tuff beds depicts their different composition. Characteristic primary mineral peaks are indicated in the header, secondary mineral peaks are indicated in the footer.

8.3.1 Heavy mineral suite of tuff beds IIIb, XIX and XXIVa

Modal analyses of the heavy mineral suite in distinct tuff beds show that the composition varies strongly. Especially the proportion of zircon to apatite, the most abundant heavy minerals, are quite varying (Figure 30). Thus, the ratio of zircon to apatite is a distinctive tephrostratigraphic criterion, while monazite and biotite have rather an accessory character. Tuff bed IIIb is well dominated by the minerals apatite (66 % of the transparent heavy minerals) and zircon (29 %). Biotite (5 %) and monazite (<1 %), however, are accessories. In tuff beds XIX and XXIVa the percentage of biotite and monazite does not change much, whereas the percentage of apatite increases to 92 % in tuff bed XIX and decreases to 5 % in tuff bed XXIVa by a comparative loss of zircon to 6 % and a gain to 90 %.

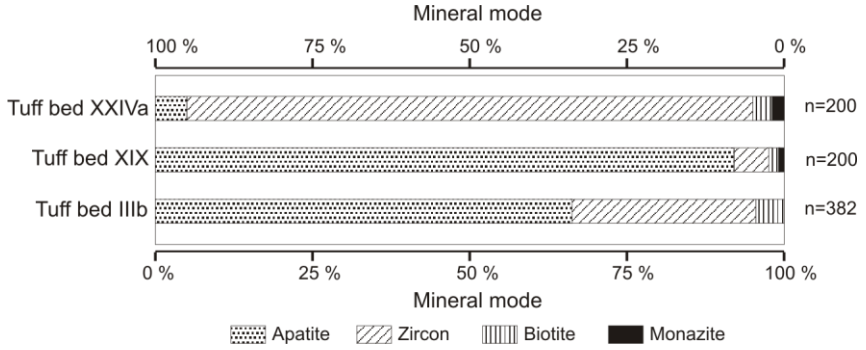

Figure 30: Qualitative contents of transparent primary heavy minerals of tuff beds IIIb, XIX and XXIVa. For particular percentages see text. While monazite and biotite have only an accessory character, a distinctive tephrostratigraphic criterion is the proportion of zircon to apatite. Note: The specific gravity of biotite may fall below 2.90 g·cm^{-3}, and thus its actual proportion may be higher than the separated proportion.

8.3.2 Zircon

An abundant accessory mineral in the tuff beds at Zwartbas is zircon (specific gravity 4.3 to 4.8 g·cm^{-3}), due to its extreme resistance to alteration. Euhedral minerals produced during early crystallisation in the magma indicate a volcanic origin and enable tephrostratigraphic correlation through euhedral zircon population. By contrast, growth obstruction, crystal size, glass inclusions and idiomorphism are not exclusively diagnostic for volcanic rocks as they also occur, though less frequently, in plutonic and metamorphic rocks.

Zircons from the examined tuff horizons are principally clear and colourless, only sporadically with a pale yellow or brown tinge. Micro-inclusions sometimes cause a dull appearance, as commonly found in sample XXIVa. The high relief under plane-polarised and bright high-order interference colours under cross-polarised light is typical of zircon crystals.

Most zircons are euhedral (Figure 32A, D), but some are subhedral minerals or sharp-edged fragments. Individual minerals are stumpy to long-prismatic with a long axis ranging 60 to 215 µm and a short axis of 20 to 90 µm. While sample IIIb contains lath-shaped crystals, up to 215 µm long, crystals in XIX are restricted to a maximum length of 185 µm. Zircons from tuff bed XXIVa are rather stumpy to normal-prismatic. The largest elongation (length-width ratio: longest extent commonly parallel to c-axis) of 6 to 6.5 was found in the XXIVa sample, which also shows an unusual twin peak at 2.0 and 3.0 (Figure 31). An elongation of about 2.0 and slightly more, as in IIIb and XIX, is a usual ratio for granitic igneous rocks, while sedimentary deposits tend to have smaller ratios of 1.0 or less. This implies that the examined tuffs are of volcanic origin and were primarily deposited without secondary transport, which would break these crystals.

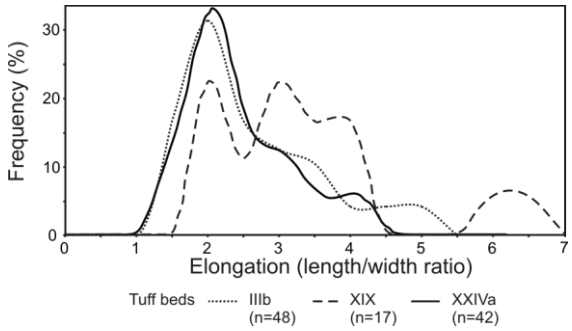

Figure 31: Elongation diagrams of samples IIIb (n=48), XIX (n=17) and XXIVa (n=42) demonstrate the frequency of crystals with a particular length-width ratio (elongation).

Typical cores and zoning in zircon crystals, which are obtained due to temperature dependent growth rate variation, were recognised through colour changes in some larger crystals in samples XXIVa and sporadically in IIIb. Penetration twins or notches, which are typical of volcanic origin, usually observed in sample XXIVa. They form by partial growth hindrance in the melt.

Many zircons contain inclusions of various types. Most common are globular to oval slightly elongated, sometimes tubular, rarely orientated (subparallel to the c-axis) brown inclusions of glass. Sample IIIb is dominated by 15 to 20 µm long and sometimes less than 2 µm thick tubular and lath-shaped fluid inclusions as well as globular glass inclusions (Figure 32B, C, E) of usually 10 to 25, but sometimes more than 45 µm in length. The few zircons in sample XIX show rarely globular, but commonly tubular, up to 40 µm, glass inclusions. The largest spectrum of different inclusion shapes was recognised in the mount of tuff bed XXIVa. Lath-shaped fluid inclusions, only 1 to 2 µm thick and 5 to 10 µm long, are often accompanied by oval to globular glass inclusions with a diameter of 15 to 45 µm. Crystals without zonation seem to have more and preferentially lath-shaped inclusions.

8.3.3 Apatite

Apatite (specific gravity 3.10 to 3.35 $g \cdot cm^{-3}$) is probably the most abundant heavy mineral in the examined tuff beds. Apatite is a prominent constituent of fresh silicic volcanic ash, as its fragments occur as accessories in magmatic rocks and also commonly in bentonites. In bentonites, its appearance is largely restricted due to its susceptibility to acid dissolution. Nevertheless, apatite may occur as euhedral, hexagonal broken prisms with basal cleavage. Although degradation of ash is caused by acid leaching, which would also attack apatite, the abundance of apatite in older bentonite suggests that it is a relatively stable mineral.

Apatite from the tuff beds IIIb and XIX are colourless and clear. In tuff bed XXIVa a slightly greyish colour was observed. Under crossed nicols, the apatites show low-order grey interference colours.

The apatite minerals mostly are euhedral crystals, or angular fragments are common. Individual grains are isometric or prismatic. In sample IIIb the mineral elongation ranges from 30 to 200 µm, in XIX 40 to 140 µm and the longest minerals in XXIVa do not exceed 10 µm. Occasionally, irregular mineral shapes and etching pits on crystal surfaces are caused by corrosive weathering.

Inclusions of brown glass derived from melt trapped during early crystallisation in the magma chamber are frequently found in apatite (Bangert et al., 2000). Apart from the sometimes elongated, irregularly round to oval 20 to 25 µm glass inclusions (Figure 32F), elongated tubular magma filled cavities, usually 20 to 50 µm long, (Figure 32G) also occur, which may extend to almost the entire length of the crystal (up to 100µm). Glass inclusions were preferentially found in IIIb and XXIVa, but were also recognised in the thin-section of VIIIb. Elongated fluid inclusions, however, were found in all examined samples.

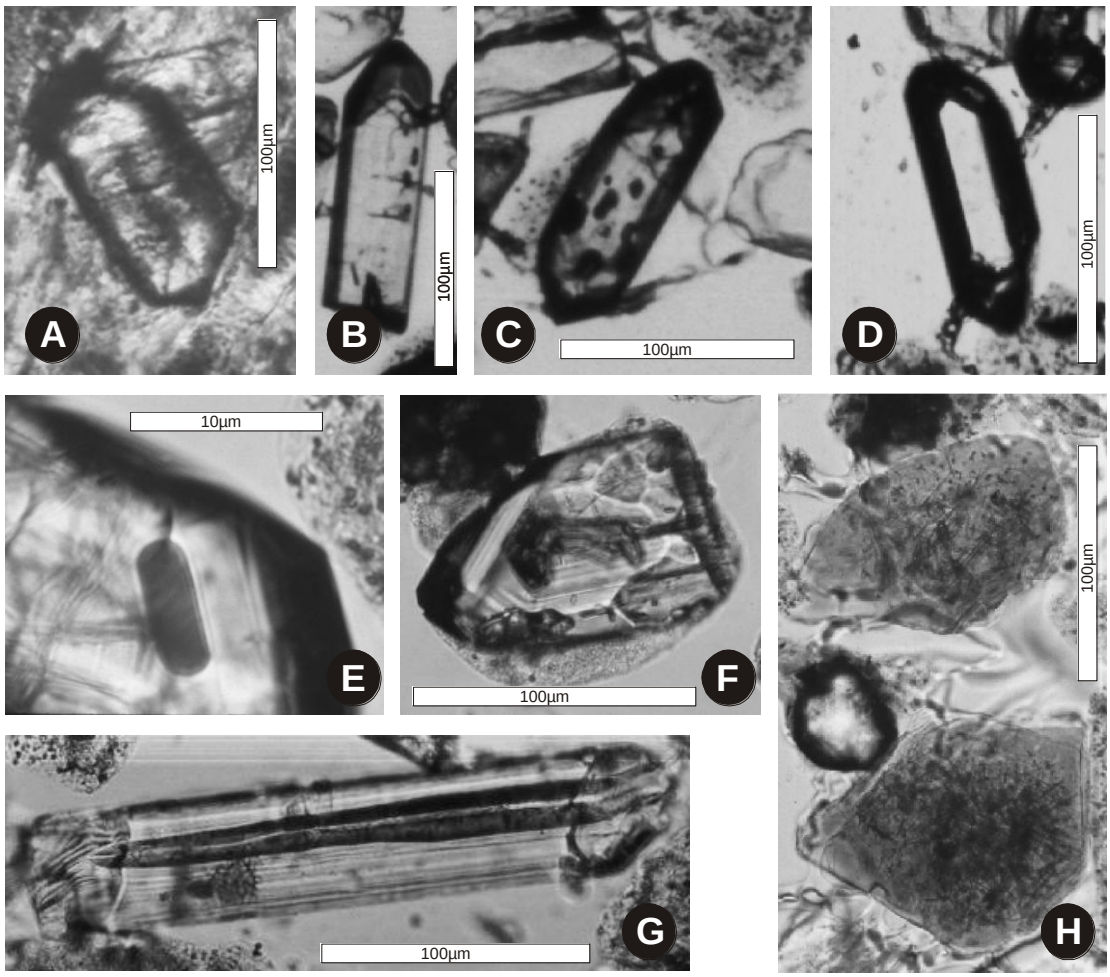

Figure 32: Primary volcanic heavy minerals from selected tuff beds. (A) Normal-prismatic *zircon* within the clay matrix from VIIIb with elongated inclusion parallel to c-axis. (B) Prismatic *zircon* with broken edge at the bottom and tiny globular glass inclusions. (C) Prismatic *zircon* containing numerous globular glass inclusions. (D) Clear *zircon* devoid of inclusions. (E) Elongated globular glass inclusion in a *zircon* without orientation. (F) Irregularly elongated globular glass inclusion in a broken *apatite*. (G) Extremely elongated tubular glass inclusion in a long-prismatic *apatite*. (H) Marginally corroded *biotite* containing a lattice structure of needle-like crystals.

8.3.4 Monazite

Monazite (specific gravity 4.8 to 5.5 g·cm^{-3}) is, along with zircon, a relatively common accessory mineral in granitic rocks, where it forms in early crystallisation. Although monazite is quite resistant to alteration, corroded monazite crystals are characteristic accessories in altered ash tuffs.

The few observed monazites had a pale, resin-like, yellow colour, which distinguished them from zircon, although both show a high relief. Interference colours are high but diffuse, often concentrically arranged and with incomplete extinction.

The recognised minerals are only 30 to 90 µm long and edge-rounded with etching pits, which is typical for juvenile monazites.

Only once (sample XXIVa), pale red, highly irregular globular inclusions were observed. Colourless, needle-like inclusions of probably gas or fluid were found in monazites from IIIb, XIX and XXIVa.

8.3.5 Biotite

Modal examinations of biotite by heavy mineral separation is hampered by the wide range of specific gravity (2.7 to 3.3 g·cm^{-3}), since lighter biotite can not be separated. Although biotite generally was not detected by XRD, the presence of biotite in grain mounts from IIIb, XIX and

XXIVa corresponds with the thin-section analysis of tuff bed VIIIb (Chapter 8.4). Bohor and Triplehorn (1993) considered biotite a common component in acid magmatic ash and outlined its strong susceptibility to weathering processes and alteration to kaolinite, which often forms around distorted biotite wisps (Figure 33B).

The biotites are reddish-brown to dark brown. Frequently they have pale greyish-green marginal transitions due to chloritisation, which characteristically starts at the margins and may lead to authigenic chlorite development (Heim, 1990). Biotite often shows a distinct pleochroism from pale to dark brown and slightly undulatory extinction, because the flakes commonly lie at the base (along main cleavage). In the thin-section of VIIIb the biotite is mainly replaced by barrel-shaped kaolinite booklets, in which sometimes residual biotite floats. XRD results suggest that several tuff layers experienced this kind of alteration.

In the grain mounts pleocroitic flakes usually are about 100 to 150 µm in diameter. The mount of tuff bed IIIb contains less altered, subhedral and pseudohexagonal biotite flakes with numerous needle-like mineral inclusions, possibly sphene, which normally form a lattice structure (Figure 32H). Biotite in XIX and XXIVa are much more altered and have corroded rims or anhedral shapes as well as less frequent mineral inclusions.

8.3.6 Authigenic heavy minerals

Apart from juvenile ash-fall derived heavy minerals, varying amounts of authigenic heavy minerals form through weathering and diagenesis.

Scarcely disseminated 10 µm long, mainly anhedral opaque mineral grains of probably haematite (specific gravity 5.2 $g \cdot cm^{-3}$), which are confined to microfractures, were observed in sample IIIb. Furthermore, almost opaque reaction rims of probably iron hydroxide (goethite, specific gravity 4.0 to 4.4 $g \cdot cm^{-3}$) form semi-translucent, dark brown patchy dendrite-like structures, up to 6 mm long and 2 mm wide, which emanate from the base of the tuff bed or from fractures into the tuff (Figure 33A). The same minerals sporadically form coronas around some grains. The preferred mineral distribution that is confined to micro-fractures and bed boundaries confirms the secondary mineral growth. In particular, the grain mount of tuff bed XXIVa contains a considerable number of up to 100 µm pyrite cubes (specific gravity 4.8 to 5.1 $g \cdot cm^{-3}$). Chlorite (specific gravity 2.6 to 3.3 $g \cdot cm^{-3}$) is an abundant secondary mineral, which forms when biotite and/or other micas, clay minerals and mixed-layer minerals experience chloritisation. The platy irregular chlorite flakes appear pale greenish-brown with micro-granular structure. Baryte (specific gravity 4.5 $g \cdot cm^{-3}$) was recognised with certainty only in IIIb by its sharp-edged form and low interference colours with pale yellow.

8.4 Secondary minerals

After the deposition of volcanic ash, secondary minerals form. Their formation is controlled by the alteration of primary components or precipitation from ground and surface water during diagenesis and weathering (Bohor and Triplehorn, 1993).

8.4.1 Microscopy

The matrix-forming clay minerals are very difficult to describe using optical criteria. Nevertheless, one group, the Kaolinite Group, produces a characteristic grain shapes, the so-called kaolinite booklets. On average these booklets are 80 to 100 µm, yellowish-ocher almost rectangular barrel-shaped grains with a layered wavy internal structure and frequently containing a dark brown central distorted central wisp (approximately 10 by 40 µm). Some of these larger distorted wisps were identified with certainty as biotite (Chapter 8.3.5), due to typical pleochroism from pale to dark brown and high interference colours with birds-eye structure. The orientation of the internal layering often differs from that of the surrounding matrix. Under crossed polars the booklets display high order

interference colours, although the residual biotite appears continuously dark brown (Figure 33A). Spears et al. (1999) recognised similar alteration structures of originally lath-shaped biotite crystals in Carboniferous bentonites in England.

Other angular ocher grains, commonly 40 but up to 200 µm, show neither internal layering nor a central wisp or nucleus. In crossed-polarised light, undulatory, grey interference colours appear. Because of their clear rectangular shape, they were considered to be feldspar pseudomorphs (Figure 33B).

Furthermore, 10 to 15 µm thin and 60 to 80 µm long cuspate minerals occur, which show no trace of a residual mineral. These again display variable interference colours and internal layering. At least their shape suggests that they were derived from altered glass shards.

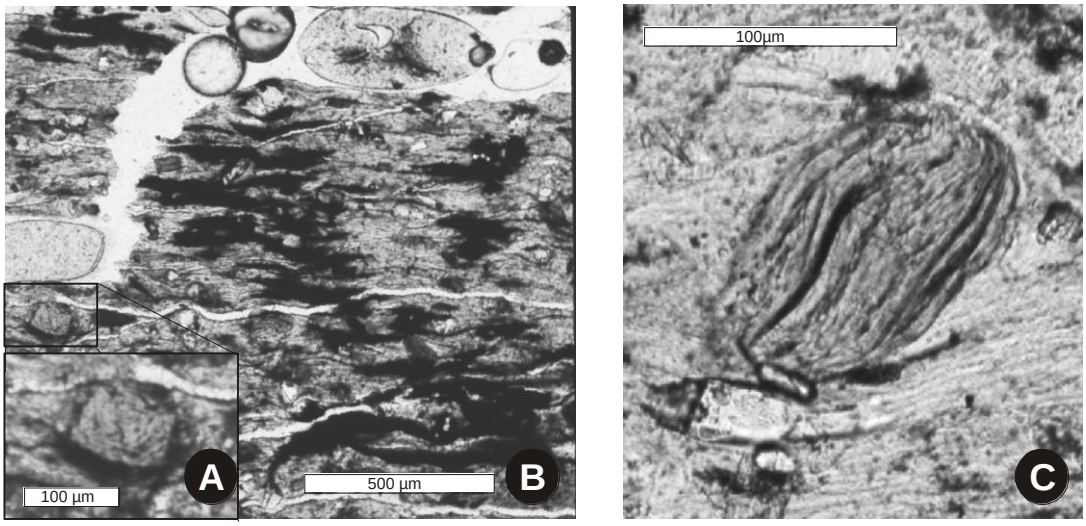

Figure 33: Thin-section microphotograph of tuff bed VIIIb. (A) Rectangular kaolinite booklet represents a feldspar pseudomorph. (B) Iron hydroxide (goethite) forms the dark dendrite to the right-hand side. (C) Layered kaolinite booklets with distorted wisp of residual biotite.

8.4.2 XRD analysis

XRD is usually the only practical technique used to obtain desirable information about the sub-microscopic clay minerals, although it is still a delicate science. Their recognition will be described in the following, widely in reference to Heim (1990).

Based upon the XRD diagrams of the sampled tuff beds (Figure 29), the only omnipresent and most abundant mineral is the non-expanding illite (clay-mica), basically a hydrated microscopic muscovite formed by muscovite degradation. Illite has the general formula $(K,H_3O)Al_2(Si, Al)_4O_{10}(OH)_2$ - xH_2O, in which x represents a variable amount of water. The structure of this **Clay-Mica Group** is similar to the Montmorillonite Group. Illite was easily recognised by its major interference peaks at 8.8 °2θ (001)-reflection, 19.8 °2θ (020), 26.8 °2θ (003)/(022) and 34.9 °2θ (130). At least tuff bed IIIb may contain an accessory proportion of biotite as suggested by the strong double peak at 60 °2θ. Heim (1990) outlines that an authigenic formation of biotite is possible, even at a low-digenetic stage.

The second frequent clay mineral is the non-expanding kaolinite, a member of the so-called **Kaolinite Group**. All the group members are polymorphs with a corresponding chemistry with the formula $Al_2Si_2O_5(OH)_4$. Kaolinite occurs in tuff beds IIIb, X, XVIIId, XIX and XXIc. Characteristic kaolinite peaks are located at 12.4 °2θ (001) and 24.9 °2θ (002)/($1\bar{1}1$).

Moreover, several of the examined tuff beds (IIIb, X and XXXIV) contain minerals of the **Chlorite Group**, a group of non-expanding platy clay minerals, chemically similar to the Vermiculite Group, but having a single hydroxide layer between the sheets in place of the exchangeable cations and water. The general chlorite formula is $X_{4\text{-}6}Y_4O_{10}(OH,O)_8$ with X representing either Al, Fe, Li, Mg, Mn, Ni,

Zn or (more rarely) Cr and Y representing either Al or Si, or (more rarely) B or Fe. Chlorite can generally be discerned by the common (001)-reflection at 6.2 to 6.3 °2θ and a characteristic (060)-reflection between 59.7 and 60.1 °2θ. The (001)-reflection, by contrast, interferes with the broad peak of mixed-layer minerals of chlorite and expandable minerals, most probably smectite (tosudite). Such a chlorite/smectite mixed-layer mineral probably produces the small (004)-reflection at 11.30 °2θ in tuff beds IIIb and XXXIV.

In tuff beds IIIb and XXXIV smectite was also recognised with certainty. The **Montmorillonite/Smectite Group** is composed of several minerals including vermiculite and montmorillonite, which both differ in chemical content. The general formula is (Ca, Na, H)(Al, Mg, Fe, $Zn)_2$(Si, $Al)_4O_{10}(OH)_2$ - xH_2O, and x represents the variable amount of water. Smectite in mixed-layer minerals, together with chlorite, has characteristic interference peaks at 5.6 °2θ (002) and 11.3 °2θ (004).

8.4.3 Inferences on primary constituents

Summarising the obtained compositional information of the tuff beds, typical mineral degradation paths can be used to draw conclusions about the primary mineral composition. Initially, intermediate to acid pyroclastic deposits, especially those with an abundant glass proportion, decompose through the formation of smectite, mainly montmorillonite (Bohor and Triplehorn, 1993). The glass abundance comes from enrichment due to aeolian fractionation (cf. Chapter 4.1). Further reactions are dependent on the K^+-supply and the acidity of the environment (Heim, 1990). Successive degradation produces chlorite or kaolinite, when K^+ is in short supply and under basic conditions. On the other hand, when K^+ is abundant, e.g. from K-feldspar decay, it is fixed into the smectite to produce illite. The illitisation of smectite is facilitated at burial depths of maximum 2 to 3 km and temperatures less than 100 °C, but it has already been observed under surface conditions.

Thus, the presence of chlorite and kaolinite could have resulted either from enhancement reactions, which successively replaced the kaolinite and chlorite with illite during burial, or from a subsequent degradation of kaolinite and chlorite from illite during uplift and erosion. A useful clue comes from the microscopy, where kaolinite occurs frequently as pseudomorphs of feldspar and glass shards, or as kaolinite booklets originated from biotite leaves. This replacement reaction, where primary material or at least primary grain shapes remain, points to an incompleted enhancement reaction.

Chapter 9 Radiometric ages of the tephrostratigraphic beds

Distal ash fall tuffs represent isochronous beds or horizons often extending over large areas and deposited in a short time. Besides their appropriation for correlation, radiometric dating on igneous minerals allows to calibrate tephrochronologically sedimentary sequences. Within the Warmbad Basin radiometric ages have not yet been determined for the Carboniferous-Permian deposits, while several age determinations were carried out on equivalent rocks in the Aranos and Main Karoo Basin. In the Warmbad Basin the current evaluations comprise new correlation potential and a chronostratigraphic calibration for the Dwyka within the southern African Karoo Sequence.

Useful igneous minerals for dating tuffs are plagioclase, sanidine, biotite, zircon, apatite and hornblende (Bohor and Triplehorn, 1993). Integrated K, Rb, or U atoms in distinct isotope concentrations result in specific analytical ratios in reference to their half-life time. This evaluated ratio of radiogenic product vs. radioactive producer provides an apparent age. As a function of time the proportion of the radiogenic product increases by the radioactive disintegration of the radioactive producer. An interpretation of the analytical ratio may give a probable numerical age. Uncertainties for age determination are the suitability and purity of minerals, contamination, and degree, time and nature of alteration (Baadsgaard and Lerbekmo, 1982). Alternative whole-rock ages for tuffs are less meaningful because these were usually formed in open systems with a high element mobility.

The current study used juvenile igneous zircon, which is very stable and, from experience, delivers precise U/Pb ages. The U/Pb zircon dating was carried out by ion microprobe (SHRIMP = Super High Resolution Ion Micro Probe).

To attain a maximum time coverage within the succession at Zwartbas, the tuff beds III b and XXXIV were evaluated because they allowed reasonable sampling. They were expected to be formed by primary ash deposits without secondary reworking or detrital admixing.

9.1 SHRIMP

The analytical procedure of SHRIMP dating was carried out at the laboratory at the Research School of Earth Sciences of the Australian National University at Canberra (executive director: Dr. R. Armstrong). It should be mentioned again that it was only possible to obtain this expensive analysis by expending funds of the Dr. rer. nat. thesis project of B. Bangert, who also incorporated the results in his study (cf. Bangert et al. (2000)).

Zircons were separated as a fraction of the heavy mineral content from the samples by this author (Chapter 6.4). In Canberra, zircon grains of each sample were handpicked from the final concentrate under a binocular microscope and mounted in epoxy together with the zircon standard AS3 and SL13. The grains were polished to approximately half their diameter and photographed. Cathodoluminescence imaging revealed hidden and complex internal structures and improved the selection of the target area for analysis.

The SHRIMP data have been reduced in the style of Compston et al. (1992) and Williams and Cleasson (1987). U/Pb in the unknowns were normalised to a $^{206*}Pb/^{238}U$ value of 0.1859 (equals an age of 1099.1 Ma) for AS3. U and Th concentrations were measured in relation to those in the SL13 standard. Ages were calculated from $^{206*}Pb/^{238}U$ ratios, with a correction for common Pb made using the measured $^{207}Pb/^{206}Pb$ and $^{206}Pb/^{238}U$ values according to Tera and Wasserburg (1972) and Compston et al. (1992).

9.2 Tuff bed III b

Zircons from this sample are light brown, with variable shape from elongated to somewhat squat shapes with dominantly pyramidal faces. Irregular gas bubble inclusions and holes are common.

A total of nineteen analyses were made on nineteen different grains in order to determine their U-Th-Pb isotopic compositions and concentrations. The data are plotted in Figure 34 and are listed in

Table 4. From Figure 34 it can be seen that the data points cluster near the concordia with the majority showing minimal Pb-loss and common Pb contents. Analyses 1.1 and 13.1 have very high common Pb contents and these grounds are excluded from some age calculation. The only other analysis excluded is 8.1 which appears to have suffered Pb-loss and also has a slightly elevated common Pb content. The remaining seventeen analyses are statistically part of a single age-group for which a weighted mean $^{206*}Pb/^{238}U$ age of **302.3 ± 2.1** Ma is calculated (n=17; mean sum of weighted deviates MSWD = 0.56, probability = 0.92). This age is interpreted to be the age of the magmatic event whithin the zircons crystallised and the magma erupted producing the ash.

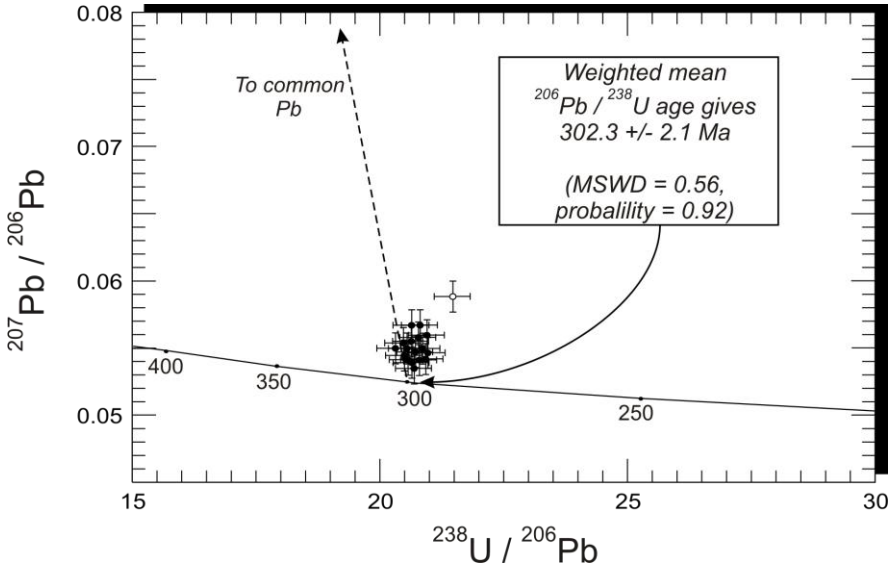

Figure 34: U-Pb concordia plot according to Tera and Wasserburg (1972) of SHRIMP data (uncorrected for common Pb) from zircons separated from the tuff sample III b. The unfilled data point is excluded from the main group for the reasons described above.

							Radiogenic		Age (Ma)	
Grain. Spot	U (ppm)	Th (ppm)	Th/U	Pb* (ppm)	$^{204}Pb/^{206}Pb$	f_{206} (%)	$^{206}Pb/^{238}U$	±	$^{206}Pb/^{238}U$	±
1.1	324	405	1.25	19	0.022534	43.83	0.0490	0.0191	308.3	118.6
2.1	307	270	0.88	17	0.000366	0.25	0.0488	0.0007	307.0	4.6
3.1	125	114	0.91	7	0.000424	0.34	0.0485	0.0007	305.5	4.4
4.1	200	144	0.72	11	0.000037	0.22	0.0482	0.0008	303.5	4.6
5.1	214	313	1.46	13	0.000323	0.48	0.0476	0.0007	299.5	4.5
6.1	267	431	1.62	17	0.000096	0.15	0.0482	0.0006	303.2	3.9
7.1	201	255	1.27	12	0.000010	0.38	0.0478	0.0008	301.2	4.7
8.1	115	128	1.11	6	0.000010	0.75	0.0463	0.0008	292.0	4.7
9.1	134	152	1.13	8	0.000134	0.51	0.0479	0.0008	301.9	4.6
10.1	285	266	0.93	16	0.000126	0.31	0.0489	0.0007	307.8	4.5
11.1	172	145	0.84	9	0.000448	0.42	0.0474	0.0007	298.4	4.2
12.1	107	90	0.84	6	0.000322	0.26	0.0477	0.0008	300.6	4.7
13.1	221	280	1.27	12	0.002856	5.65	0.0468	0.0007	295.0	4.4
14.1	185	225	1.22	11	0.000000	0.27	0.0477	0.0007	300.5	4.2
15.1	294	477	1.62	19	0.000102	0.23	0.0485	0.0007	305.4	4.0
16.1	219	157	0.72	12	0.000010	0.20	0.0484	0.0008	304.7	4.7
17.1	225	167	0.74	12	0.000222	0.18	0.0482	0.0008	303.7	4.7
18.1	380	464	1.22	23	0.000010	0.22	0.0476	0.0007	299.4	4.0
19.1	206	144	0.70	11	0.000360	0.26	0.0480	0.0008	302.4	4.8

Table 4: Summary of SHRIMP U-Th- Pb zircon results for sample IIIb.

9.3 Tuff bed XXXIV

The heavy mineral concentrate provided for this sample was dominated by baryte and Fe-oxides phases. Careful handpicking produced only three zircons or zircon fragments, one of which was too altered to be useful. The other two zircons show well-defined magmatic zoning and no signs of mechanical abrasion.

Only three analyses were done on the two good zircons grains, with the data reported in Table 2 and plotted on a diagram (Figure 35) according to Tera and Wasserburg (1972). The two analyses on Grain #1 are statistically indistinguishable and give a weighted mean $^{206*}Pb/^{238}U$ age of **300.3 ± 6.3 Ma**. A single analysis on the second zircon revealed unexpectedly high Th and U concentrations. The relatively poor precision of the age calculated on the pooled data set is a consequence of the small number of analyses possible, but is statistically within error of the other Dwyka Group ages.

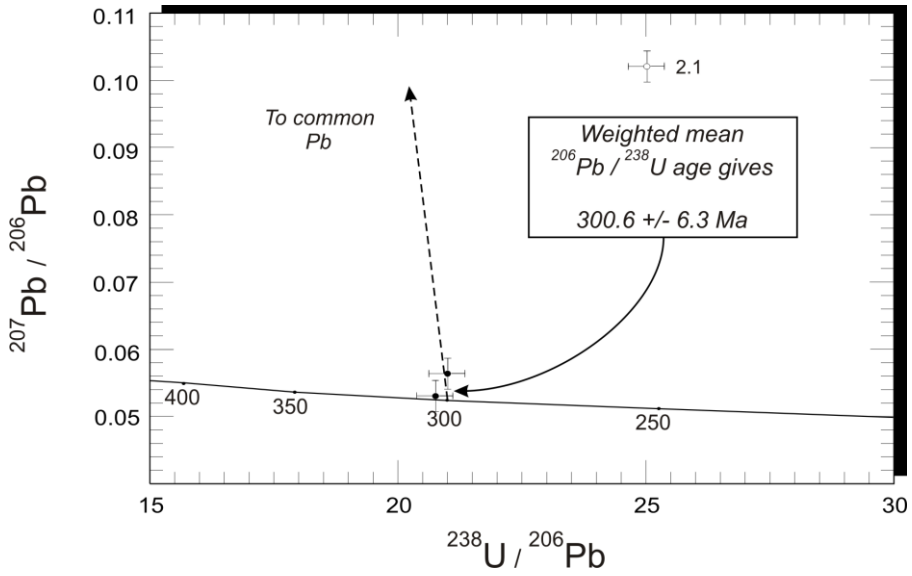

Figure 35: U-Pb concordia plot according to Tera and Wasserburg (1972) of SHRIMP data (uncorrected for common Pb) from zircons separated from the tuff sample XXXIV. The age shown was calculated from the two analyses shown as filled circles.

							Radiogenic		Age (Ma)	
Grain. Spot	U (ppm)	Th (ppm)	Th/U	Pb* (ppm)	$^{204}Pb/^{206}Pb$	f_{206} (%)	$^{206}Pb/^{238}U$	±	$^{206}Pb/^{238}U$	±
1.1	374	220	0.59	19	0.000055	0.07	0.0481	0.0007	302.87	4.31
1.2	135	61	0.45	7	0.000127	0.49	0.0472	0.0008	297.28	4.74
2.1	979	2480	2.53	41	0.003532	6.24	0.0378	0.0005	239.19	3.06

Table 5: Summary of SHRIMP U-Th- Pb zircon results for sample XXXIV.

9.4 Tephrochronological approach

Efforts to establish a tephrochronology for the lower part of the Dwyka were hampered by pure sampling due to the insufficient thickness of the tuff beds and by overlapping age dating results of particular tuffs due to a small analytical resolution. Moreover, the financial reasons limited the number of age determinations.

Including ages from the Main Karoo Basin the radiometrically recorded succession extends from the basal Dwyka Group with oldest ages of about 302 Ma to the basal Prince Albert Formation with ages of about 289 Ma (Bangert et al., 1999). Therefore the deposition of the Dwyka Group took at least more than 10 Ma. This does not preclude the existence of even earlier deposits, which were later removed during the onset of the glaciation. The new ages of this study agree with those recently determined in the basal Dwyka in the Mariental area of the Aranos Basin (Bangert et al., 1999).

Chapter 10 Geochemistry of the bentonite horizons

Chemical analyses are key tools for identification, rock classification, correlation, determination of the original magmatic composition, consequently of their provenance and the geotectonic setting of fallout tephra. In many depositional settings, where tephra layers are preserved, devitrification of the volcanic glass or its alteration to clay minerals obstructs the evaluation of the results, as the chemical signature may have changed substantially. Usually the determination of major element chemistry has little application because the original chemical composition has been changed and new substances have been added, others were leached during weathering and diagenesis of the volcanic ash. Immobile trace and rare-earth elements (REE), however, are commonly used to classify the original magmatic composition and the tectonic setting of the provenance of parent magmas.

Chemical fingerprints of tuff beds have been successfully used in tracing, correlating and distinguishing different horizons, e.g. Huff and Kolata (1990). Furthermore, many methods have been developed so far as to determine the composition of the original ash and therewith the type of source magma by using immobile elements. A comprehensive overview of the interpretation of geochemical data is provided by Rollinson (1993). In combination with studies on biozones and facies pattern, chemical fingerprinting is a powerful correlation tool.

In this study, whole rock analyses (major, traces and rare-earth elements) of individual ash beds within the lower Dwyka Group were performed to obtain perceptions on their chemical character, source melts, volcanic and geotectonic origin, possible correlation and individual distinctions. The proportions of major elements, which were used in discrimination diagrams, are always normalised to 100%.

10.1 Element behaviour and alteration effects

To understand the applicability and significance of classification methods performed on individual samples and their correlation relevance, a comprehensive perception of element locations and behaviours in mineral phases and their mobility during secondary alteration is necessary.

10.1.1 Major elements

Alteration caused by weathering and diagenesis changes the mineralogical composition as well as the content of volatile constituents (e.g. H_2O and SO_2). Loss on ignition (LOI), i.e. volatile contents of about 8 to 9 % on average may, but probably does not, significantly affect analytical results of the studied samples by their dilution effect (Irvine and Baragar, 1971). Commonly SiO_2, K_2O and Na_2O show negative correlation compared to volatile content, while total Fe_2O_3 and CaO correlate positively. In contrast, Mg, Mn, Ti and Al are relatively immobile at any stage. Ti is mainly present in ilmenite, but it also occurs in pyroxene, amphibole and biotite, where it replaces Al. Whereas ilmenite and Ti oxides are very resistant to secondary alteration, Ti-bearing silicates decompose easily, Ti dissolves and transforms to the stable mineral phases of anatase and rutile. The volatile element phosphorus (P), which is mainly concentrated in the heavy minerals apatite and monazite, is soluble in acid environment. The examined tuffs, however, contain high amounts of apatite (Chapter 8.2.1).

During the alteration of acid ashes or the decomposition of rhyolitic glass, Al_2O_3, CaO, total Fe_2O_3 and H_2O are enriched, whereas SiO_2, Na_2O and K_2O are depleted.

10.1.2 Trace and rare-earth elements

The following descriptions of elements were compiled by Arz (1996) with improvements by Königer (1999).

Vanadium (V). Vanadium preferentially enters early-formed magnetite but also mica amphibole and clinopyroxene. During weathering V remains in the residual iron-bearing minerals and/or becomes incorporated in clay minerals.

Chromium (Cr). Chromium is largely removed from magma in early stages of crystallisation as chrome spinel. Its behaviour closely resembles Al^{3+} and Fe^{3+}. Cr is concentrated in magnetite, ilmenite, pyroxene, garnet, amphibole and biotite. During secondary alteration processes Cr behaves similarly to Al^{3+} and Fe^{3+} and is finally concentrated in clays.

Cobalt (Co). Cobalt behaves very similarly to Ni. The major part of Co in the magma is removed in early-formed magnesian minerals like olivine, garnet, pyroxene, amphibole, and also in magnetite and ilmenite. Co is very mobile during weathering and does not form residual silicate minerals, in contrast to Ni.

Nickel (Ni). The ionic radius and charge of Ni are identical with those of Mg. Therefore, Ni bears a very close resemblance to Mg and is predominantly incorporated in early-formed minerals like olivine, pyroxene, magnetite, ilmenite and amphibole. During weathering Ni is easily mobilized but is coprecipitated with Fe and Mn oxides.

Zinc (Zn). The Zn ion replaces ferrous Fe and Mg. In basic rocks Zn is mainly present in magnetite whereas in more acid rocks its abundance is mainly controlled by biotite and/or amphibole occurences. Zn possesses only restricted mobility during weathering, controlled by adsorption of carbonates, hydroxides and phosphates rather than by solubility.

Gallium (Ga). Ga^{3+} is similar to Al^{3+} and to a much lower degree to Fe^{3+}. Therefore, it is preferentially concentrated in feldspar, amphibole, mica and magnetite during late stages of magmatic crystallisation. During weathering there is a tendency for Ga to be concentrated in residual materials. However, Ga is more mobile than Al, resulting in a decreasing Ga/Al ratio in the residual materials during the weathering process.

Rubidium (Rb). Rubidium very closely resembles K, as illustrated by the fact that Rb is always incorporated in K-minerals, especially in biotite and K-feldspar. During weathering Rb is again closely related to K but is held in adsorption position more firmly than K.

Strontium (Sr). The ionic radius of Sr^{2+} is intermediate in size between Ca^{2+} and K^{+}, therefore it may substitute for either Ca or K in minerals. In igneous rocks Sr is mostly incorporated into plagioclases in place of Ca. However, the pyroxene structure does not accommodate the Sr ion. There is a ready substitution of Sr for K in alkali feldspar, but limited incorporation of Sr for Ca in amphibole and Sr for K in mica. Mobilization of Sr during weathering is attributed to decomposition of plagioclase and alkali feldspars because these minerals are the major host minerals of Sr. Sr is rather a mobile element during weathering, although it is less mobile than Ca.

Barium (Ba). The ionic radius of Ba^{2+} is nearly identical to that of K^{+}. Therefore, biotite and K-feldspar are the most important Ba carriers. Substitution of Ba in place of Ca in plagioclase, pyroxene, amphibole and apatite is limited. Ba is a highly mobile element during weathering, especially due to destruction of biotite and K-feldspar.

Lead (Pb). Lead is, similar to Ba, diadochic with K. Therefore, biotite and K-feldspar are the most important Pb-carrying minerals. During weathering loss of Pb is attributed to decomposition of biotite and K-feldspar.

Zirconium (Zr). The relatively large size and high charge of Zr^{4+} ion ensures that Zr does not enter into some of the rock-forming minerals but is present in a separate phase, usually zircon, but can also be incorporated in oxide minerals like xenotime, ilmenite, or rutile. During weathering zircon is almost indestructible.

Niobium (Nb). Host minerals for Nb are biotite, amphibole and Ti minerals. During weathering Nb is either released to solutions due to destruction of those minerals or remains behind within resistant minerals like ilmenite, zircon, sphene, etc.

Thorium (Th). Thorium and **uranium** (U) behave very similarly. In igneous rocks Th is mainly incorporated in allanite, monazite, sphene and zircon. Th is relatively immobile compared to U, because the latter oxidizes to a soluble uranyl ion.

Rare-earth elements (REE) and **Yttrium** (Y). The REE and Y all have very similar chemical and physical properties because they form stable 3^+ ions of similar size. Under oxidizing conditions, cerium (Ce) is oxidized to Ce^{4+} and has a very different behaviour from the trivalent ions. Europium (Eu) may exist in the trivalent or bivalent state, depending on the redox state of the system. The size and charge of the Eu^{2+} ion are almost identical to those of Ca^{2+}. Therefore, Eu substitutes for Ca, especially in feldspar, so Eu at least in part may behave as a compatible element. The bivalent Eu may become mobile and reprecipitate in an oxidizing environment. The other REE and Y are incompatible with respect to feldspar. Garnet and particularly zircon, preferentially incorporate the heavy REE (HREE: Tb-Lu, higher atomic numbers), while monazite and allanite are strongly enriched in the light REE (LREE: La-Gd, lower atomic numbers). In apatite and sphene, light and heavy REE are enriched relatively to the middle REE (intermediate atomic numbers). The presence of amphibole, apatite and/or sphene can contribute to a positive Eu anomaly in the melt. The presence of pyroxene leads to slight enrichment of the LREE compared to the middle or HREE and can also contribute to a positive Eu anomaly. According to Bohor and Triplehorn (1993), a negative Eu anomaly is characteristic of silicic volcanism. In rhyolitic systems, biotite leads to depletion of the LREE. The REE are relatively insoluble under conditions of metamorphism and at the earth‘s surface, although in some cases they are mobile over small distances and redistribute in secondary alteration products.

Whole-rock trace element analyses of altered portions of tuff layers compared with unaltered portions show that immobile elements like Ti, Sc, Zr, Hf and Ta retain their initial concentrations, while more reactive alkaline and calc-alkaline elements (e.g. Rb, Sr and Cs) are usually mobile. Th and U show unconsistent mobility behaviours. LREE – including Eu – are normally immobile, whereas HREE are commonly depleted in alkaline solutions but retain in more dilute pore fluids.

Trace metals (e.g. Pb, Bi, Sb, As, Cu, Ag and Re) are partitioned into the vapour-phase during eruption and devitrification of silicic tuffs, and thus their whole-rock proportion may be modified from their original distribution in the parental magma. Since these metals usually precipitate as mineral coatings in pores, they are available for remobilisation by ground water and hydrothermal fluids. As an exception Pb is preserved in its original concentration.

10.2 Reliability of chemical studies and influences on chemical composition

The acute mobility of major elements precludes them widely for classification and correlation purposes, since the original geochemical composition may have changed excessively (Bohor and Triplehorn, 1993). Reliable determination of volcanic origin, their tectonic setting, classification and correlation of altered tuffs should preferentially be based on immobile trace and rare-earth elements. These studies generally use discrimination plots developed from empirical studies of igneous rocks of a known origin. They provide by no means absolute proof of magmatic origin, but provide important information about magma chemistries and tectonic setting which, in particular cases, can help ambiguous classifications.

Besides the alteration of deposited ash, pre-depositional influences affect the expressivity for discrimination and correlation. Lateral composition changes within individual tuff horizons can be mainly caused by either chemical and mineralogical zonation of magma chambers due to fractional crystallisation or physical fractionation during explosive eruption processes and subaerial transport. Erupting heterogeneous, zoned magma chambers may eject pyroclastic material with chemical variation with time. Furthermore, ejected material may be distributed in different directions because of wind direction changes at different heights. Finally, fractionation by transport takes place. This effect could be well studied at the May 18, 1980 Mount St. Helens' eruption to increase SiO_2, K_2O, Rb and Zr and decrease Al_2O_3, CaO, TiO_2 and Sr downwind (Fischer and Schmincke, 1984). Such a relative SiO_2 enrichment can be explained by the progressive separation of crystals with less silicon (plagioclase, hornblende, pyroxene, apatite and magnetite) from the glass which is transported farther.

Vertical variations in geochemistry as function of time, in which the ash-tuff is deposited, are possible (Hinkley et al., 1987) but have not been recognised in this study due to the small thickness of the individual layers and the problem of vertical sampling therewith.

In addition, lateral composition changes can be found in areas with contemporaneously active volcanoes which may cause overlapping ash lobes (Fischer and Schmincke, 1984). Moreover, post-depositional wind winnowing and secondary reworking of primary ash tuffs as well as admixture with detrital material in fluvial, flood plain and marginal marine environment may influence the composition in reference to the host melt.

In consideration of the assumed distal location of the studied ash tuffs and the quite restricted size of the investigation area, significant lateral changes in geochemical composition were neither expected nor could they be proved. But, admittedly, the statistic uncertainty within the classifications involving major and trace element concentrations are considerably high due to limited control sampling. However, the results of all tuff beds do not show wide deviation, because all individual beds are probably of the same origin. Thus all samples together represent a significant representation of the chemistry of their common source. Reliable discrimination aspects for individual tuff beds are shown only by REE patterns (cf. Chapter 10.7).

10.3 Distinction of pyroclastic beds from epiclastic deposits

Pyroclastic deposits usually retain characteristic geochemical and mineralogical fingerprints from their parental magma, which allows for them to be distinguished from epiclastic sediments (Wray, 1999). Apart from most immobile rare-earth elements (Chapter 10.7), even the mobile major element concentrations in the tuff beds from Zwartbas show an obviuos geochemical discrimination from the shales (Figure 36).

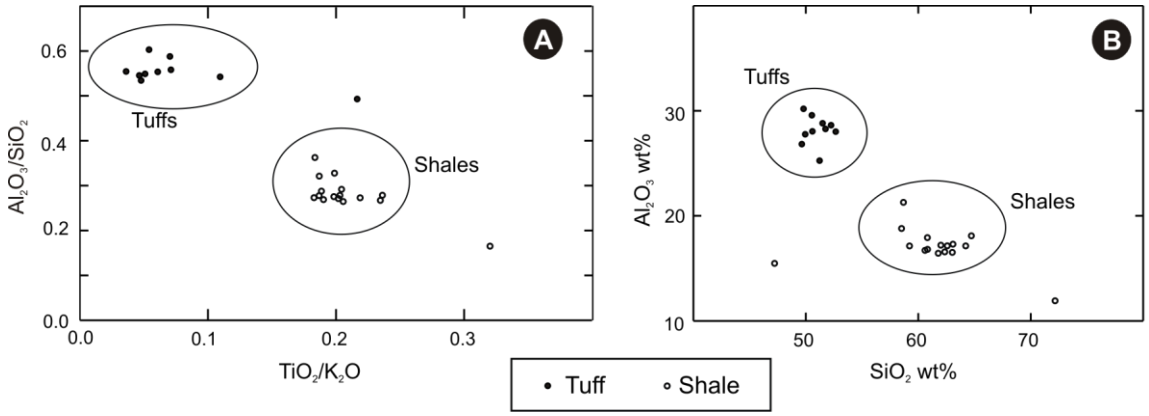

Figure 36: Element concentrations diagrams distinguish tuff beds from shales. (A) Al_2O_3/SiO_2 vs. TiO_2/K_2O. (B) Al_2O_3 vs. SiO_2. Both diagrams show two distinct clusters, one of the shale, the other of the tuff beds.

10.4 Rock classification by major elements

As discussed in Chapter 10.2, major elements are often not indicative for the composition of the original melt. Nevertheless, classifications on major elements within the examined tuff horizons mainly agree with results of tuff layers at other locations and their presumed origin. SiO_2-independent diagrams imply a SiO_2 depletion due to alteration, since the average concentrations of about 50 wt% SiO_2 (Table 6) in the tuffs do not agree with their assumed intermediate to acid source (andesitic, dacitic or rhyolitic magma). Thus SiO_2-dependent classifications for the parental magma were avoided. Likewise Na was depleted, while Al and K were enriched in the course of devitrification, compaction and diagenesis of the volcanic glass. Total LOI of about 6 to 7 wt% indicates that the rocks containing volcanic glass, possibly porous pumice, have been strongly hydrated (Chesner, 1998).

	IIIb-1	IIIb-2	IIIb -2 *)	VII-1	VII-2	X*)	XIII	XVIII*)	XIX	XXIc*)	XXIVa-1*)	XXIVa-2	XXIVa-3	XXXIV
SiO_2	49.70	49.80	50.54	50.80	50.70	52.30	52.60	49.69	51.40	51.22	50.43	50.70	48.70	49.90
TiO_2	0.43	0.43	0.43	0.26	0.26	0.34	0.32	0.68	0.48	1.21	0.51	0.52	0.48	0.39
Al_2O_3	27.60	27.60	28.22	28.20	28.10	28.54	28.10	26.96	28.70	25.25	29.66	29.80	28.50	30.10
Fe_2O_3	2.55	2.48	2.56	2.10	2.29	1.77	1.68	6.26	1.77	7.00	2.92	1.21	3.00	1.50
MnO	0.04	0.03	0.06	0.01	0.02	0.01	0.02	0.09	0.02	0.05	0.01	0.01	0.01	0.01
MgO	2.92	2.27	2.91	2.19	2.18	2.12	1.96	1.71	1.98	1.70	1.82	1.92	1.69	1.77
CaO	0.28	1.11	0.39	0.29	0.21	0.37	0.11	0.28	0.33	0.50	0.13	0.06	0.09	0.51
Na_2O	0.44	0.40	0.39	0.30	0.30	0.32	0.97	1.05	1.05	1.43	0.64	0.60	0.70	0.41
K_2O	7.09	7.04	7.30	7.23	7.18	7.33	6.69	6.21	6.75	5.59	7.25	7.27	6.84	7.22
P_2O_5	0.11	0.11	0.10	0.07	0.07	0.03	0.05	0.11	0.17	0.14	0.05	0.03	0.03	0.04
LOI	6.30	6.66	6.74	6.29	6.34	6.32	6.12	6.64	6.66	6.27	6.61	6.27	7.09	6.55
SUM	91.09	91.19	93.07	91.44	91.30	93.13	92.46	93.04	92.60	94.09	93.45	92.12	89.97	91.87
Nb	7	7	5	12	14	16	7	6	8	11	5	7	5	5
Zr	206	203	206	268	263	273	128	168	204	168	171	155	161	96
Y	28	28	22	50	54	50	28	30	35	36	25	33	25	16
Sr	30	43	41	40	37	33	37	53	49	73	55	35	36	84
Rb	304	368	298	356	365	288	306	225	282	213	157	303	295	312
Pb	7	6	5	11	8	5	2	15	6	36	29	7	40	2
Ga	29	29	29	32	30	32	30	22	28	17	23	28	26	28
Zn	11	14	27	44	101	44	96	230	101	312	124	57	52	1
Cu	13	15	-	0	12	-	0	-	0	-	-	0	12	0
Ni	13	10	5	13	20	5	17	42	22	34	5	18	47	0
Co	5	0	<10	0	0	<10	0	<10	0	11	<10	0	8	0
Cr	14	9	12	13	17	18	19	13	14	26	16	13	13	10
V	57	63	53	30	28	40	61	138	51	119	83	87	102	55
Ba	1133	1318	1100	1253	1251	1034	957	1018	1013	865	929	1134	1116	1069
Sc	10	13	<10	16	11	<10	14	19	11	23	14	15	14	13
Li	24	27	-	17	17	-	20	-	20	-	-	15	13	15
Be	4	5	-	5	3	-	3	-	2	-	-	2	2	3
Y	22	26	-	51	56	-	30	-	34	-	-	31	24	14
Zr	176	208	-	296	297	-	141	-	203	-	-	158	146	98
Nb	9	10	-	17	17	-	9	-	10	-	-	9	7	4
Mo	<1	<1	<5	5	9	<5	<1	<5	2	11	<5	4	37	<1
Cs	16	20	-	18	20	-	17	-	14	-	-	17	19	14
La	9.50	11.80	-	63.10	73.00	-	11.40	-	40.10	-	-	47.90	29.00	1.90
Ce	24.00	30.00	-	179.00	203.00	-	26.00	-	89.00	-	-	143.00	83.00	5.00
Pr	3.00	3.80	-	21.90	25.10	-	3.20	-	9.60	-	-	16.30	9.40	0.60
Nd	11.90	15.50	-	89.10	104.20	-	13.80	-	35.30	-	-	63.90	36.40	2.40
Sm	2.80	3.30	-	18.40	21.90	-	3.90	-	7.20	-	-	13.00	7.50	0.90
Eu	0.72	0.92	-	2.13	2.53	-	1.07	-	1.63	-	-	1.96	1.37	0.53
Gd	3.30	3.80	-	15.40	17.60	-	4.50	-	7.10	-	-	10.60	6.50	1.60
Tb	0.57	0.63	-	1.91	2.14	-	0.77	-	1.02	-	-	1.17	0.78	0.32
Dy	3.80	4.40	-	10.10	11.00	-	5.00	-	5.90	-	-	6.20	4.60	2.60
Ho	0.83	0.97	-	2.02	2.18	-	1.03	-	1.21	-	-	1.19	0.90	0.56
Er	2.56	2.86	-	5.98	6.01	-	3.00	-	3.75	-	-	3.60	2.80	1.76
Tm	0.38	0.45	-	0.84	0.88	-	0.45	-	0.58	-	-	0.53	0.42	0.24
Yb	2.26	2.70	-	5.50	5.67	-	2.86	-	3.61	-	-	3.31	2.59	1.69
Lu	0.35	0.39	-	0.79	0.77	-	0.40	-	0.51	-	-	0.49	0.40	0.24
Hf	4	5	-	6	6	-	4	-	5	-	-	6	5	3
Ta	14	16	-	15	15	-	15	-	11	-	-	6	5	4
W	1	1	-	2	6	-	2	-	3	-	-	3	5	3
Tl	2	2	-	2	2	-	2	-	2	-	-	2	2	2
Bi	<1	<1	-	2	2	-	<1	-	<1	-	-	<1	<1	<1
Th	70	81	71	60	57	59	68	13	55	9	44	58	47	66
U	3	3	<5	13	13	<5	8	<5	9	<5	<5	13	8	4
S	-	-	<0.02	-	-	<0.02	-	<0.02	-	<0.02	<0.02	-	-	-
Sn	-	-	<15	-	-	<15	-	<15	-	<15	<15	-	-	-

Table 6: Geochemical analysis of individual tuff beds from Zwartbas. Highlighted values are single measurements or mean values of multiple measurements. Values are not normalised. Major elements in wt%, trace elements in ppm.
*) Analysis carried out in Würzburg.

10.4.1 Classification by TiO_2/Al_2O_3 ratios

According to Fischer and Schmincke (1984) TiO_2/Al_2O_3 ratios are used for classifying the chemical origin of tuffs. They consider tuffs with ratios >0.02 as acid, 0.02 to 0.14 as intermediate and 0.14 to 0.18 as basic. Since alteration increases the Al_2O_3 content in clay-rich bentonites by the factor 1.5 to

2.0, original data were divided by 2 for determination (Table 7). The average TiO_2/Al_2O_3 ratios of 0.018 to 0.096 in the studied tuffs indicate an acid to intermediate source magma. No trend in chemical variation throughout the succession was recognised.

Tuff bed	IIIb*)	VII*)	X	XIII	XVIIId	XIX	XXIc	XXIVa*)	XXXIV
$TiO_2/½Al_2O_3$	0.031	0.018	0.024	0.022	0.050	0.034	0.096	0.025	0.026
A/NK	3.68	3.75	3.73	3.67	3.71	3.68	3.60	3.76	3.94
A/CNK	3.36	3.63	3.56	3.62	3.58	3.53	3.36	3.59	3.70

Table 7: Average $TiO_2/(½Al_2O_3)$ ratios and A/CNK values of the sampled ash tuffs (see text for explanation).
*) Mean values of multiple measurements (Table 6).

10.4.2 Classification according to Shand (1951)

Average A/CNK values (Shand index = $Al_2O_3/(CaO+Na_2O+K_2O)$) of 3.36 to 3.70 and A/NK values ($Al_2O_3/(Na_2O+K_2O)$) of 3.60 to almost 4.00 (see Table 7) classify all samples as peraluminous. The limiting value to metaluminous and peralkaline rocks is an A/CNK of 1.0. Further, an A/NK below 1.0 distinguishes peralkaline rocks from metaluminous rocks with accordingly higher values (Shand, 1951).

10.5 Rock classification by trace elements

Relatively secure classifications can be obtained by using immobile trace elements, the concentrations of which remain relatively constant during alteration.

10.5.1 Classification by individual elements

Spears and Rice (1973) realised that acid ashes comprise indicatively high concentrations of Th, U, Pb, Sn, Bi, Y, Be and B, but low concentrations of Ti, Cr, V, Ni, Cu and Co. Stöffler (1963) considered Cr contents to be characteristic for the origin of tuffs. While ultrabasic to basic rocks contain Cr up to 1400 ppm, granites and their volcanic equivalents show average concentrations of about 5 ppm and less. Cr concentrations in the investigated tuffs with values of 10 to 26 ppm suggest an acid to intermediate origin.

10.5.2 Classification according to Leat et al. (1986)

The slightly modified Nb-Zr projection from Leat et al. (1986) classifies almost all the analysed tuffs as medium-K respectively calc-alkaline rocks (i.e. rhyolites, rhyodacites, andesites and tholeiites). For most of the tuffs Figure 37 shows an overlap of the calc-alkaline and high-K field, which attributed to more intensive alteration effects (Königer, 1999).

10.5.3 Classification according to Winchester and Floyd (1977)

Classification projections of Winchester and Floyd (1977) largely avoid the use of mobile elements because they are easily affected by alteration and metamorphism. In contrast, immobile elements, e.g. Ti, Zr, Nb, Y, Ga and Ce, were approved to be deficient in secondary enrichment or depletion, and thus serve as more reliable classification variables.

The Zr/TiO_2-Nb/Y projection is suitable to distinguish different magma series. Thereby Nb/Y ratio appears as a degree of alkalinity, because the concentrations do not vary through the differentiation process. This diagram uses a boundary value of 0.67of Nb/Y ratio, where higher values indicate basic, lower values intermediate volcanic deposits. This allows a distinction of alkaline eruptive rocks with high Nb/Y ratios from calc-alkaline rocks with low Nb/Y ratios. In the diagram (Figure 38), the examined tuff horizons show exclusively calc-alkaline nature with rhyolitic to andesitic composition.

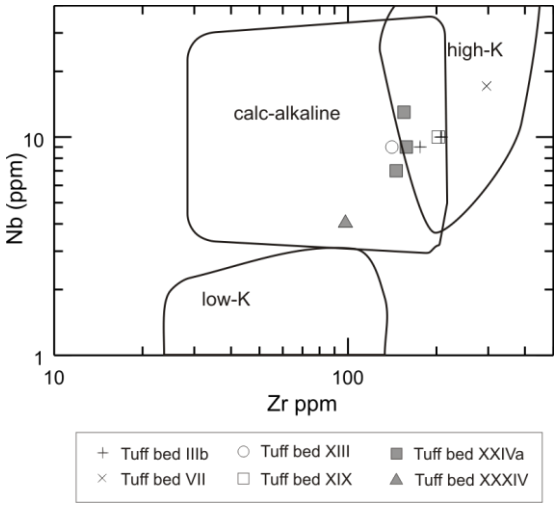

Figure 37: Classification of the studied tuff beds in the slightly modified Nb-Zr diagram of Leat et al. (1986).

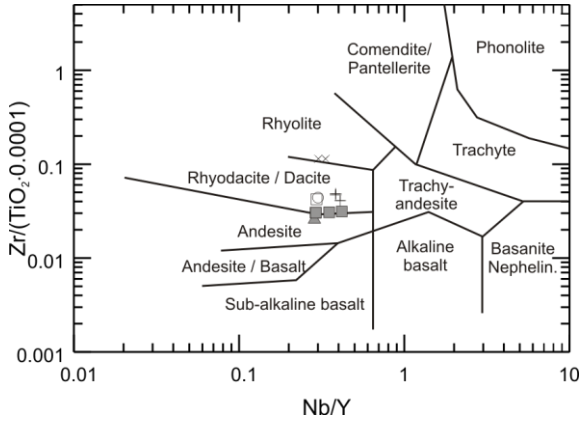

Figure 38: Classification of the examined tuff beds in the Zr/TiO_2-Nb/Y discrimination diagram of Winchester and Floyd (1977). For legend see Figure 37.

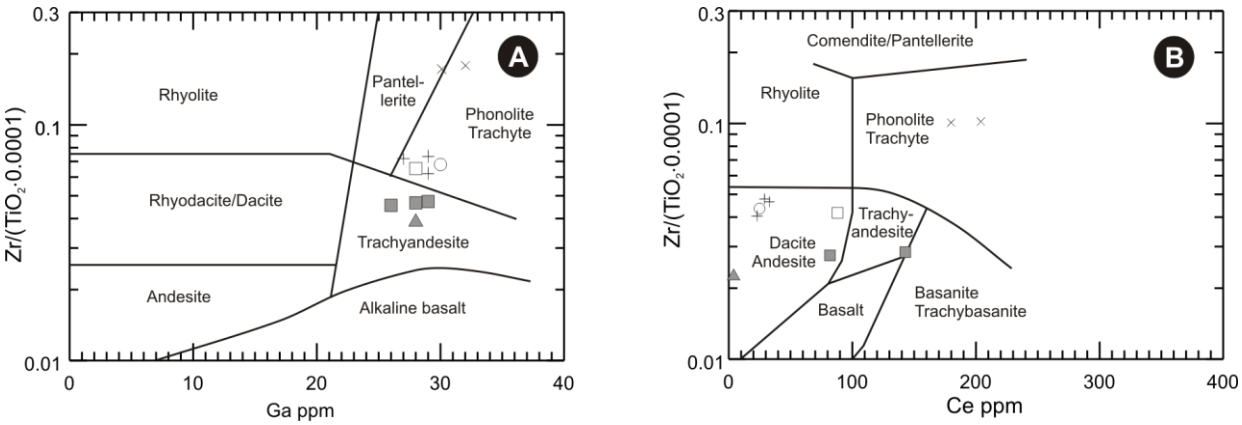

Figure 39: Classification of the examined tuff beds with discrimination diagrams of Winchester and Floyd (1977). (A) Zr/TiO_2-Ga discrimination diagram. (B) Zr/TiO_2-Ce discrimination diagram. For legend see Figure 37.

The Zr/TiO_2-Ga projection uses the fact that in alkaline rocks Ga contents distinctly increase during differentiation, whereas rocks of the calc-alkaline series retain the content of the original magma. The plot, however, differs compositionally from most of the classifications, since the high Ga contents ascribe the tuffs to the trachyandesite, trachyte and phonolite fields of the alkaline series (Figure 39A). A similar behaviour is shown by Ce. Nevertheless, the data scatter widely, since the studied tuff beds

predominantly plot in the calc-alkaline field (Figure 39B). Only tuff IIIb and individual samples of tuff XXIVa plot in consistence with the Zr/TiO_2-Ga projection within the alkaline field.

10.6 Geotectonic origin of the tuff horizons

Immobile trace and rare-earth element concentrations are also characteristic of the tectonic regime indicating magmatic activity. Thus the degree of magma differentiation characterises the tectono-magmatic position of its source. Since the tuffs of the Dwyka Group were dominantly classified as acid to intermediate, tectonic discrimination diagrams of granites were used to determine the tectono-magmatic derivation of the ash tuffs. Granites form by partial melting of the country rock, whose chemical composition is adopted. Since the tectonic setting partly controls the type of source rock at depth, granite composition correlates with tectonic-setting.

Discrimination failures can be explained by either the high complexity and multiphase activity of orogenic settings or compositional changes due to differentiation, mixing, assimilation and alteration before final crystallisation and consolidation. Further discussions about terminology and reliability of tectono-magmatic discriminations are in Königer (1999).

10.6.1 Classification according to Hine et al. (1978)

Besides several classifications using SiO_2 as indicative variable, Hine et al. (1978) introduced the TiO_2-Zr discrimination diagram to distinguish S-type granites (derived from sediments) from I-type granites (derived from igneous rocks). Both I- and S-type granites are orogenic granites. Figure 40 shows that I-type as well as S-type granite affinities occur.

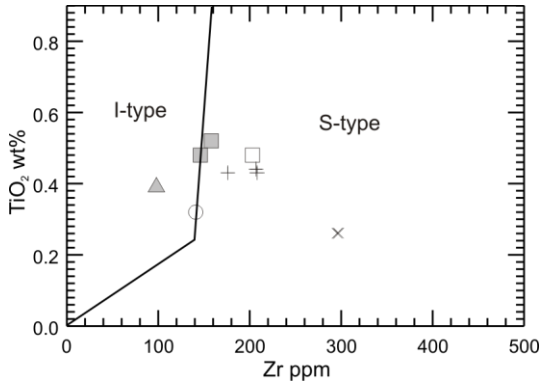

Figure 40: Classification of the examined tuff beds by their magma derivation according to Hine et al. (1978). For legend see Figure 37.

10.6.2 Classification according to Pearce et al. (1984)

The classification of Pearce et al. (1984) divides granites based on their intrusive setting into four groups: ocean ridge granites (ORG), volcanic arc granites (VAG), within-plate granites (WPG) and collision granites (COLG). Suitable discrimination variables are trace elements e.g. Rb, Y and Nb. In the very common Nb-Y projection all tuffs, except tuff VII, plot within the volcanic arc and syn-collision granites field (VAG+Syn-COLG) (Figure 41A). Tuff VII shows an indistinct character. The Rb-(Y+Nb) diagram is less expressive, as the projection may again infer a syn-collision granite origin (Syn-COLG), but the results plot close to the junction of the VAG and WPG fields (Figure 41B).

Additionally, ORG-normalised spider diagrams of particular major and trace elements are suitable to distinguish different tectonic settings (Pearce et al., 1984). Such a spider diagram of the studied tuffs (Figure 42) shows a stronger affinity to syn- and post-collision granites than to volcanic arc granites.

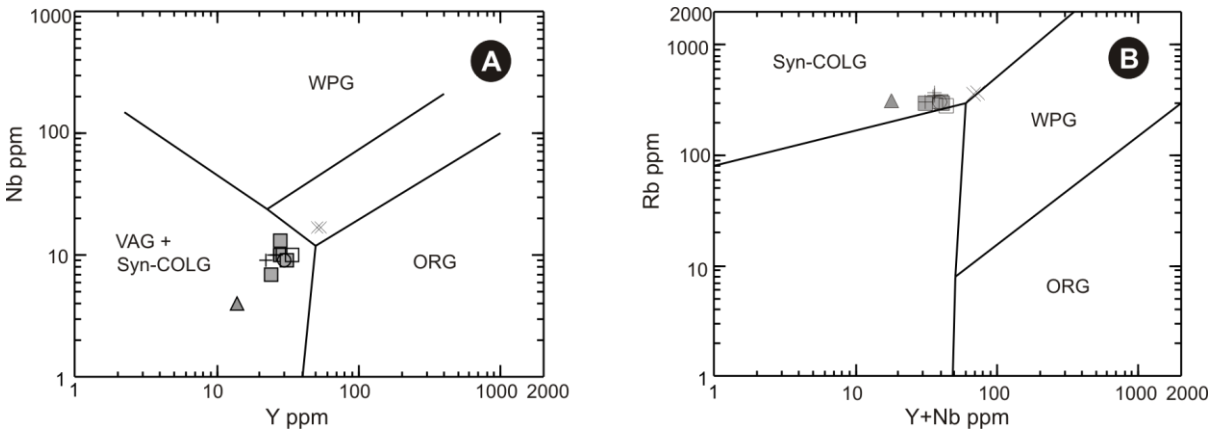

Figure 41: Classifications of the studied tuff beds within tectono-magmatic discrimination diagrams of (Pearce et al., 1984). (A) Nb-Y discrimination diagram. (B) Rb-(Y+Nb) discrimination diagram. For legend see Figure 37. Further explanations are given in the text.

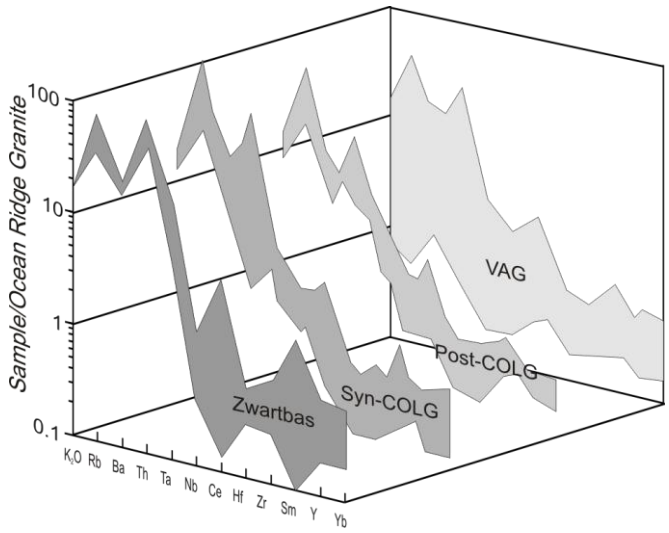

Figure 42: Comparison of ocean ridge granite (ORG) normalised geochemical patterns of the studied tuff beds from Zwartbas with representative analyses of volcanic arc granites (VAG), syn-collision granites (Syn-COLG) and post-collision granites (Post-COLG) according to Pearce et al. (1984).

10.6.3 Classification according to Harris et al. (1986)

The classifications of Harris et al. (1986) are based – in the style of Pearce et al. (1984) – on projections of Rb in relation to Zr, Hf, Ta and/or SiO_2. While the samples predominantly plot in the (Rb/Zr)-SiO_2 diagram (Figure 43A) into the syn-collision granite (Syn-COLG) due to the diagenetic loss of SiO_2, the ternary (Rb/30)-Hf-(Ta·3) diagram (Figure 43B) reflects a stronger affinity of the samples to the post-collision granites (Post-COLG) and the within-plate granites (WPG).

10.7 REE signature

The compatibility of the bivalent Eu in plagioclase and potassium feldspar often leads to a Eu depletion relative to the trivalent REE. Partial melting of a rock in which feldspar is retained or the removal of feldspar from a felsic magma during crystal fractionation contributes the Eu anomaly (Rollinson, 1993). However, Eu depletion can also be caused by its mobilization during diagenesis or loss of feldspar due to weathering. Nevertheless, in respect of the well developed appearance, the negative Eu anomaly in the studied tuff beds (Figure 44), normalised to chondritic values, supports the perception of a felsic magma. In contrast to their general depletion of HREE relative to the LREE, tuff bed XXXIV shows an inverse REE pattern. While LREE are depleted, the HREE are relatively

enriched but show lower values than the others. Since this result has not been confirmed by further analyses of proximal tuff beds, conclusions of changes in the chemistry of the source magma or changes of the source itself are considerable but speculative.

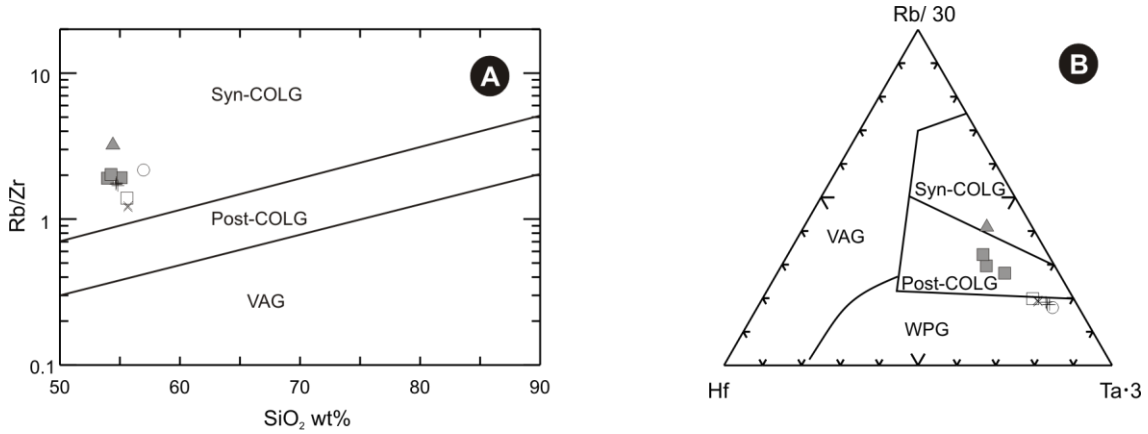

Figure 43: Classification of the examined tuff beds within the tectono-magmatic discrimination diagrams from Harris et al. (1986). (A) (Rb/Zr)-SiO_2 discrimination diagram. (B) Ternary (Rb/30)-Hf-(Ta·3) diagram. For legend see Figure 37. Further explanations are given in the text.

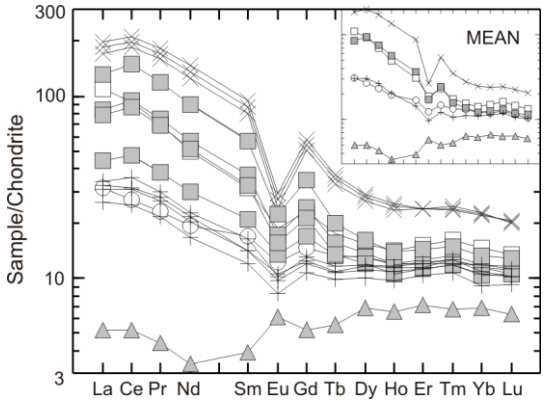

Figure 44: Rare-earth element abundance in the studied tuff beds, normalised to chondritic values, have a characteristic negative Eu anomaly for silicic volcanism. For legend see Figure 37.

REE also provide a valuable guide to distinguish clay-rich volcaniclastic layers from siliciclastic layers. Previous studies demonstrated that the REE patterns produced by shales derived from continental weathering are very similar (Wray, 1995). In the contrary, volcanic ash is typically depleted in Eu and sometimes in Ce relative to normal marine sediments. In the ideal case this anomaly outlasts diagenesis irrespective of chemical changes. Thus the normalisation of the tuff REE to shale standard REE (USGS rock standard SCo-1 (Cody Shale) from Jarvis and Jarvis (1985)) gives a graphic distinction of detrital clays from bentonites. Figure 45illustrates a characteristic depletion of Eu and a general depletion in LREE of the bentonites from Zwartbas relative to the standard shale.

The geochemical analyses have shown a general concordance of the chemical composition of the individual tuff beds. In consideration of major and trace elements, however, individual beds posses lateral variation in chemical composition even over small distances. Thus these elements are not suitable to discriminate individual tuff beds by geochemistry and to provide correlation potential. A more reliable distinctive criterion is the REE pattern. Wray (1999) demonstrated the correlative significance of tuffs in the Cretaceous Lower Saxony of Europe by REE anomalies and REE depletion in normalised REE spider diagrams (cf. Chapter 10.7) over long distances. Lateral samples of individual tuff layers from Zwartbas show the same REE patterns, but the absolute concentrations of

the elements vary (Figure 44). Figure 45 gives mean REE patterns of all analysed individual tuff beds plotted at their stratigraphic position.

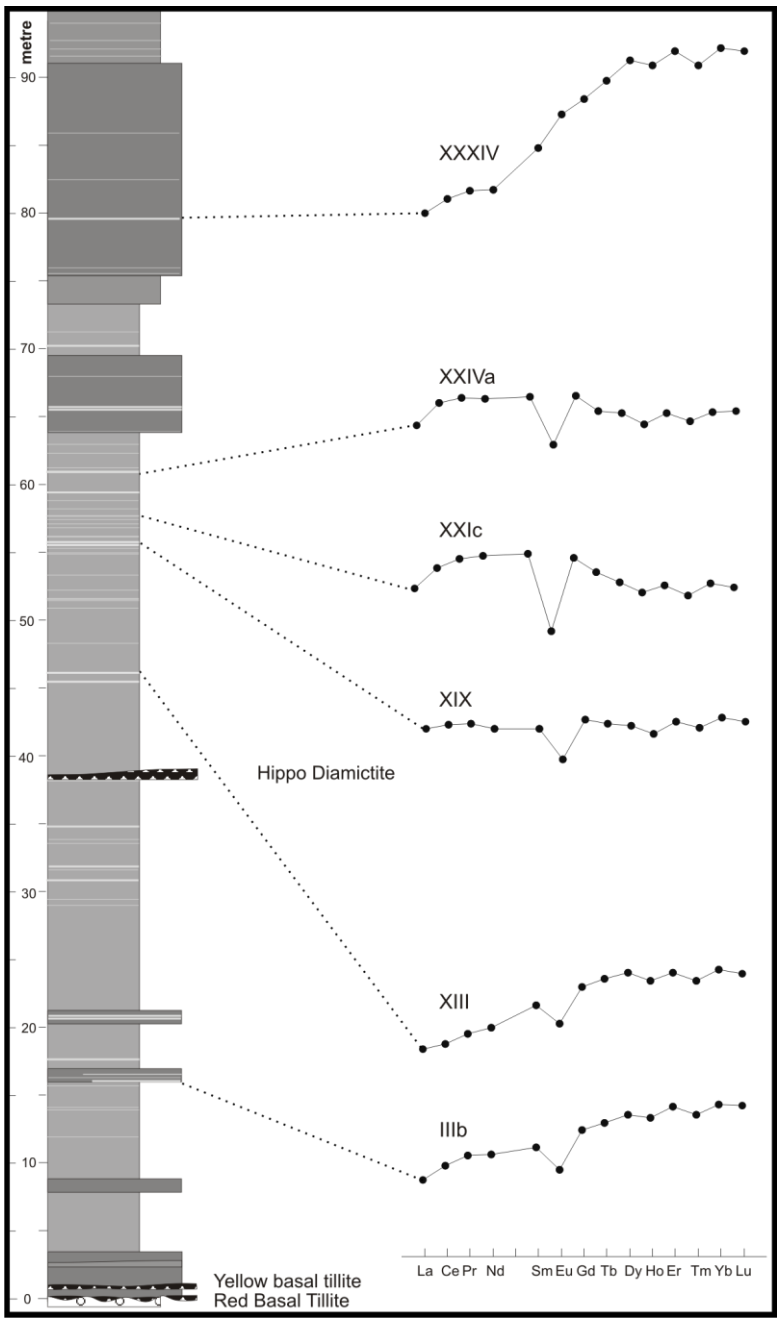

Figure 45: Shale normalised (USGS rock standard SCo-1 (Cody Shale)) REE profiles of principle bentonite beds from Zwartbas plotted stratigraphically. A characteristic negative anomaly of Eu and a general depletion in LREE are suspicious. The patterns suggest a compositional change through the succession.

10.8 Geographical origin

Pyroclastic horizons were reported from the whole lower Karoo sequence in southern Africa (Martini, 1974; Elliot and Watts, 1974; McLachlan and Jonker, 1990; Viljoen, 1990), including the Dwyka Group (Bangert et al., 1999). Although the source of the widespread tuff horizons is unknown, it is probable that the source of the ash-fall tuffs of the Dwyka was situated at the magmatic arc along the Samfrau subduction zone in present-day Patagonia (Miller, 1981). Magmatism of an appropriate age from the Cape Fold Belt, however, is not reported. Nevertheless, Stollhofen et al. (2000) and Bangert et al. (1999) differentiate magmatic sources of some ash tuffs in South Africa and Namibia

due to discrepancies in geochemistry and petrography. Bangert et al. (1999) also believes that contemporaneous proximal volcanic vents coexist with the distal volcanic arc, but the majority of the intermediate to acid pyroclastic layers were produced by the magmatic arc along the southern Gondwana margin. Figure 46 shows the geochemistry of tuff beds from different depositories. It is possible to ascribe the tuffs from the Main Karoo Basin in South Africa to an acid origin, while the southern Namibian tuffs show rather intermediate tendencies. Tuffs of the eastern Main Karoo Basin, however, deviate from the other classifications. Most of the analyses tend to acid and intermediate parental magma.

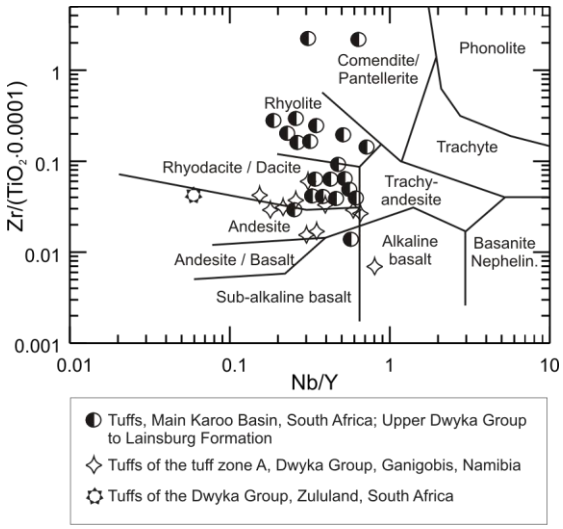

Figure 46: Geochemical classification diagram from Winchester and Floyd (1977) showing several tuff beds from the Main Karoo Basin in South Africa (after Viljoen (1990); Zululand data from Stollhofen (1999)) and the Aranos Basin in Namibia (Bangert et al., 1999). For direct comparison see Figure 38.

Chapter 11 Summary

During the Carboniferous-Permian glaciation of southern Gondwana, the Warmbad Basin formed within the onset of widespread basin formation. The basin formation was induced by glacial erosion and continued by sedimentary overburden and finally by reactivation of older structural basement anisotropies (Daly et al., 1989; Dingle and Scrutton, 1974; Frakes, 1985; Stollhofen, 1999). Marine incursions from the west occupied the subsiding regions.

The basin filling of rocks of the Karoo Supergroup commenced after an initial period of glacial erosion with a subsequent deposition of glacio-marine deposits. Glacial and interglacial lithofacies built up a sequence of four glaciation-deglaciation periods, which are consistent with the typical succession of Early Karoo rocks in southern Gondwana. Subglacial deposits of massive tillite beds overlain by proglacial proximal fluvio-glacial sandstones and distal black shales with various amounts of ice rafted debris constitute the succession at Zwartbas, at the southern margin of the Warmbad Basin. The lithofacies architecture could be correlated to the model of four deglaciation sequences within the Dwyka Group of southern Africa by Theron and Blignault (1975) and Visser (1997). Radiometric analyses on juvenile zircon crystals in distinct tuff beds with ages of 300.3 ± 6.3 Ma and 302.3 ± 2.1 Ma produced suitable time constraints. Along with correlative age determinations from the Aranos Basin and the Karoo Basin (Stollhofen, 1999; de Wit cited in Turner, 1999; Bangert et al., 1999, Holzförster and Stollhofen, 2000), the Dwyka Group can be classified chronostratigraphically to the Late Carboniferous and probably Early Permian lasting at least 10 Ma. Calcareous concretions and large sedimentation rates determined on varvites point to a high terrigenous influx. The disappearance of the concretionary layers and ice rafted debris at the Dwyka-Ecca boundary obviously coincides with the occurrence of a white weathering shale, the White Horizon, which can be correlated to the Pseudo White Band (Visser, 1991) in the Main Karoo Basin.

Geochemical analyses of shale samples from the basal Dwyka Group offer a new insight in the sedimentary environment of the distal Warmbad Basin. Low salinities in the water body that occupied the subsiding basin can be estimated from the Rb/K ratio (Campbell and Lerbekmo, 1963), Mn/Fe ratio (Frakes and Crowell, 1975) and C/S ratio (Berner and Raiswell, 1984), which all point to present day brackish conditions. The Chemical Index of Alteration (CIA) according to Nesbitt and Young (1982) suggests moderate climates in the hinterland. Total Organic Carbon (TOC), N and S concentrations propose an increasing occurrence of life with time. Concrete evidence, however, is hampered by the unsolved 'anoxia versus productivity'-problem. X-ray diffractometry (XRD) analyses of the basal shale succession supply petrographical evidence for a subsequent transition from a glacial into interglacial period.

The fossil record and the abundance of fossils implies a relative oxygen depletion and shallow water conditions, but unambiguous palaeoenvironment estimations are not possible. Several species of trace fossils (*Helmintopsis, Taenidium, Chondrites, Thalassinoides, Tisoa, Skolithos* and *Palaeophycus*), fishes (*Namaichthys schroederi*), coprolites and individual shell-bearing invertebrates build up the marine fossil fauna. Numerous fossilised wood fragments at least indicate a proximal distance to the shoreline, and the growth of plants with trunks, up to several decimetre in diameter, supports the perception of a moderate climate in the hinterland.

Within the siliciclastic deposits volcanic ash-fall derived tephra layers were interbedded. Today they appear as thin lighter-coloured, well confined and lateral continuous layers. Investigation of a cyclicity by performing a Fast Fourier Transformation (FFT) and a simple frequency distribution analysis (histogram) result in a slight cyclicity. Using the sedimentation rate obtained from varves substantiated a dominant sequential appearance of tuff layers at about 50 a. Due to their high grade of alteration and thus predominant composition of clay minerals, they were determined as K-bentonites. Their volcanic origin is preseved in the geochemical and mineralogical composition and suggest an

acid to intermediate parental magma. Since the tuffs are depleted diagenetically in SiO_2, immobile trace elements and rare earth elements (REE) were used in discrimination diagrams, e.g. from Pearce et al. (1984) and Winchester and Floyd (1977). Investigations about their geographical provenance infer their descent from the volcanic arc along the Samfrau subduction zone at the southern margin of Gondwana (Stollhofen, 1999; Bangert et al., 2000). XRD and microscopic recognition of secondary clay minerals (illite, kaolinite, chlorite and montmorillonite/smectite) and kaolinite booklets infer a quick burial history at depth of about 2 to 3 km.

References

Anderson, J.M., 1977. The biostratigraphy of the Permian and the Triassic. Part 3. A review of Gondwana Permian palynology with particular reference to the northern Karoo Basin, South Africa. Memior Botanical Survey South Africa, 41: 1-188.

Arz, C., 1996. Origin and petrogenesis of igneous rocks from the Saar-Nahe-Basin (SW-Germany): Isotope, trace element and mineral chemistry. Dr. rer. nat. Thesis, Julius-Maximilians-Universität, Würzburg, 193 pp.

Baadsgaard, H. and Lerbekmo, J.F., 1982. The dating of bentonite beds. In: G.S. Odin (Editor), Numerical dating in stratigraphy. John Wiley, New York, pp. 423-440.

Bangert, B., Stollhofen, H., Geiger, M. and Lorenz, V., 2000. High resolution tephrostratigraphy, fossil record and age of Carboniferous glaciomarine mudstones, Dwyka Group, southern Namibia. Henno Martin Special Publication, Comm. Geol. Serv. Nam.: in press.

Bangert, B., Stollhofen, H., Lorenz, V. and Armstrong, R., 1998. Bentonitic tuff horizons of the Permo-Carboniferous Dwyka-Group in Southern Africa - Pyroclastic deposits as ideal time marker. J. Afr. Earth Sc., 27(1A): 18-19.

Bangert, B., Stollhofen, H., Lorenz, V. and Armstrong, R., 1999. The geochronology and significance of ash-fall tuffs in the glaciogenic Carboniferous-Permian Dwyka Group of Namibia and South Africa. J. Afr. Earth Sc., 29(1): 33-49.

Berner, R.A. and Raiswell, R., 1984. C/S method for distinguishing freshwater from marine sedimentary rocks. Geology, 12(6): 365-368.

Boenigk, W., 1983. Schwermineralanalyse. Enke, Stuttgart, 152 pp.

Bohor, B.F. and Triplehorn, D.M., 1993. Tonsteins: Altered volcanic ash layers in coal-bearing sequences. Geol. Soc. Am. Spec. Publ., 285, 56 pp.

Bromley, R.G., 1996. Trace Fossils: Biology, taphonomy and applications. Chapman & Hall, London, 361 pp.

Brongniart, A.T., 1823. Observations sur les fucoids. Société d'Histoire Naturelle de Paris, Mémoires, 1: 301-320.

Bucher, K. and Frey, M., 1994. Petrogenesis of Metamorphic Rocks. Springer Verlag, Berlin, 318 pp.

Campbell, F.A. and Lerbekmo, J.F., 1963. Mineralogic and chemical variations between Upper Cretaceous continental Belly River shales and marine Wapiabi shales in western Alberta, Canada. Sedimentology, 2: 215-226.

Campbell, F.A. and Williams, G.D., 1965. Chemical composition of shales of Manville Group (Lower Cretaceous) of central Alberta, Canada. Bull. Am. Assoc. Pet. Geol., 49: 81-87.

Carmichael, R.S., 1989. Practical handbook of physical properties of rocks and minerals. CRC Press, Boca Raton, 741 pp.

Chesner, C.A., 1998. Petrogenesis of the Toba Tuffs, Sumatra, Indonesia. J. Petrol., 39(3): 397-438.

Compston, W., Williams, I.S., Kirschvink, J.L., Zhang, Z. and Ma, G., 1992. Zircon U-Pb ages for the Early Cambrian time-scale. J. Geol. Soc. London, 149: 171-184.

Crowell, J.C. and Frakes, L.A., 1972. Late Paleozoic Glaciation; Part V, Karroo Basin, South Africa. Geological Society of America Bulletin, 83(10): 2887-2912.

Daly, M.C., Chorowicz, J. and Fairhead, J.D., 1989. Rift basin evolution in Africa, the influence of reactivated steep basement shear zones. In: M.A. Cooper and G.D. Williams (Editors), Inversion Tectonics. Spec. Pub. Geol. Soc. London, London, pp. 309-334.

de Wit, M.J.d. and Ransome, I.G.D., 1992. Regional inversion tectonics along the southern margin of Gondwana. In: M.J.d. Wit and I.G.D. Ransome (Editors), Inversion Tectonics of the Cape Fold Belt, Karoo and Cretaceous Basins of Southern Africa. Balkeman, Rotterdam, pp. 15-21.

Dingle, R.V. and Scrutton, R.A., 1974. Continental break-up and the development of Post-Palaeozoic sedimentary basins around Southern Africa. Bull. Geol. Soc. Amer., 85: 1467-1474.

Du Toit, A.L., 1916. Notes on the Karoo System in the southern Kalahari. Trans. Geol. Soc. S. Afr., 10: 1-9.

Einsele, G., 1992. Sedimentary basins: Evolution, facies and sediment budget. Springer, Berlin, 628 pp.

Elliot, D.H. and Watts, D.R., 1974. The nature and origin of volcaniclastic material in some Karoo and Beacon rocks. Trans. Geol. Soc. S. Afr., 77: 109-111.

Fischer, R.V. and Schmincke, H.U., 1984. Pyroclastic Rocks. Springer, Berlin, 472 pp.

Frakes, L.A., 1985. A preliminary model for subaqueous-glacial and post-glacial sedimentation in intra-continental basins. Palgeogr., Palaeoclimatol., Palaeoecol., 51: 347-356.

Frakes, L.A. and Crowell, J.C., 1975. Characteristics of modern glacial marine sediments: Application to Gondwana glacials. In: K.S.W. Campbell (Editor), Gondwana Geology. Aust. Natl. Univ. Press, A. C. T., Canberra, pp. 373-380.

Frommherz, B., 1998. Palaeoecology of Westphalian and Stephanian fluvio-lacustrine strata in the Saar-Nahe Basin (SW Germany): a synthesis of macro- and microflora. Dr. rer. nat. Thesis, Julius-Maximilians-Universität, Würzburg, 309 pp.

Geiger, M., 1999. An Explanation of the Geological Map 1:10 000 of the Namibian borderland along the Orange River at Zwartbas - Warmbad District - Karas Region - Namibia. Diplomkartierung Thesis, Julius-Maximilians-Universität, Würzburg, 80 pp.

Germs, G.J.B., 1995. The Neoproterozoic of southwestern Africa, with emphasis on platform stratigraphy and paleaontology. Precambr. Res., 73: 123-136.

Gresse, P.G. and Germs, G.J.B., 1993. The Nama foreland basin: sedimentation, major unconformaty bounded sequences and multisided active margin advance. Precambr. Res., 63: 247-272.

Gresse, P.G. and Scheepers, R., 1993. Neoproterozoic to Cambrian (Namibian) rocks of South Africa: agechronological and geotectonic review. J. Afr. Earth Sc., 16(4): 375-393.

Grill, H., 1997. The Permo-Carboniferous glacial to marine Karoo record in southern Namibia: sedimetary facies and sequence stratigraphy. Beringeria, 19: 1-98.

Gürich, G., 1923. Acrolepis lotzi und andere Ganoiden aus den Dwyka Schichten von Ganikobis, Südwestafrika. Beiträge zur geologischen Erforschung der Deutschen Schutzgebiete, 19: 26-74.

Harris, N.B.W., Pearce, J.A. and Tindle, A.G., 1986. Geochemical characteristics of collision-zone magmatism. In: M.P. Coward and A.C. Ries (Editors), Collision tectonics. Geol. Soc. London Spec. Publ., pp. 67-81.

Haughton, S.H. and Frommurze, H.F., 1928. The Karoo Beds of the Warmbad District, South West Africa. Trans. Geol. Soc. S. Afr., 30: 133-142.

Haughton, S.H. and Frommurze, H.F., 1936. The geology of the Warmbad District, South West Africa; an explanation of geological sheets Amib (H-33-F), Umeis (H-34-A), and Nakop (H-34-B). Memior No. II - Department of Mines, South West Africa: 64.

Heer, O., 1877. Flora Fossilis Helvetiae. Vorweltliche Flora der Schweiz. J. Wurster & Comp., Zürich, 182 pp.

Heim, D., 1990. Tone und Tonminerale. Enke Verlag, Stuttgart, 157 pp.

Heinrich, R., 1991. Cycles, Rhythms, and Events on High Input and Low Input Glaciated Continental Margins. In: G. Einsele, W. Ricken and A. Seilacher (Editors), Cycles and events in stratigraphy. Springer Verlag, Berlin, pp. 751-772.

Hine, R., Williams, I.S., Chappell, B.W. and White, A.J.R., 1978. Contrasts between I- and S-Type Granitoids of the Kosciusko Batholith. J. Geol. Soc. Australia, 25: 219-234.

Hinkley, T.H., Smith, K.S., Taggart, J.E.J. and Brown, J.T., 1987. Chemical and mineralogical aspects of observed fractionation of ash from the May 18, 1980 eruption of Mount St. Helens. U.S. Geol. Surv. Prof. Pap., 1397-A: 1-22.

Holzförster, F. and Stollhofen, H., 2000. Lower Permian deposits of the Huab area, NW Namibia: a continental to marine transition. Henno Martin Special Publication, Comm. Geol. Serv. Nam.: in press.

Holzförster, F., Stollhofen, H. and Stanistreet, I.G., 1999. Lithostratigraphy and depositional environments in the Waterberg-Erongo area, central Nambia, and correlation with the main Karoo Basin. J. Afr. Earth Sci., 29(1): 105-123.

Huff, W.D., Bergström, S.M. and Kolata, D.R., 1992. Gigantic Ordovician volcanic ash fall in North America and Europe: Biological, tectonomagmatic, and event-stratigraphic significance. Geology, 20(10): 875-878.

Huff, W.D. et al., 1997. A biostratigraphically well-constrained K-bentonite U-Pb zircon age of the lowermost Darriwilian Stage (Middle Ordovician) from the Argentine Precordillera. Episodes, 20(1): 29-32.

Huff, W.D. and Kolata, D.R., 1990. Correlation of the Ordovician Deicke and Millbrig K-bentonites between the Mississippi Valley and the Southern Appalachians. Amer. Assoc. Petrol. Geol. Bull., 74: 1736-1747.

Irvine, T.N. and Baragar, W.R.A., 1971. A guide to the chemical classification of the common volcanic rocks. Canad. J. Earth Sci., 8(523-547).

Jarvis, I. and Jarvis, K.E., 1985. Rare-earth element geochemistry of standard sediments: a study using inductively coupled plasma spectrometry. Chem. Geol., 53: 335-344.

Johnson, M.R., van Vuuren, C.J., Hegenberger, W.F., Key, R. and Shoko, U., 1996. Stratigraphy of the Karoo Supergroup in southern Africa: an overview. J. Earth Sci., 23(1): 3-15.

Kingsley, C.S., 1985. Sedimentological Analysis of the Ecca Sequence in the Kalahari Basin, South West Africa - Namibia. CDM Mineral Surveys: 35.

Kingsley, C.S., 1990. Sedimentological model of the Permian Kalahari Basin, Namibia. 13th International Geological Congress, Nottingham: 274-275.

Königer, S., 1999. Distal ash tuffs in the lowermost Permian of the Saar-Nahe Basin (SW-Germany): Distribution, sedimentology, volcanology, petrography, geochemistry, and zircon ages. Dr. rer. nat Thesis, Julius-Maximilians-Universität, Würzburg, 269 pp.

Leat, P.T., Jackson, S.E., Thorpe, R.S. and Stillman, C.J., 1986. Geochemistry of bimodal basalt-subalkaline/peralkaline rhyolite provinces within the Southern British Caledonides. J. Geol. Soc. London, 143: 147-170.

Ledendecker, S., 1992. Stratigraphie der Karoosedimente der Huabregion (NW-Namibia) und deren Korrelation mit zeitäquivalenten Sedimenten des Paranàbeckens (Südamerika) und des großen Karoobeckens (Südafrika) unter besonderer Berücksichtigung der überregionalen geodynamischen und klimatischen Entwicklung Westgondwanas. Göttinger Arb. Geol. Paläon., 54: 87 pp.

Martin, H., 1981a. The Late Palaeozoic Dwyka Group of the Karasburg Basin, Namibia. In: M.J. Hambrey and W.B. Harland (Editors), Earth's pre-Pleistocene glacial record. Cambridge University Press, New York, pp. 67-70.

Martin, H., 1981b. The Late Palaeozoic Dwyka Group of the South Kalahari Basin in Namibia and Botswana and the subglacial valleys of the Kaokoveld in Namibia. In: M.J. Hambrey and W.B. Harland (Editors), Earth's pre-Pleistocene glacial record. Cambridge University Press, New York, pp. 61-66.

Martin, H., Walliser, O.H. and Wilczewski, N., 1970. A goniatite from the glaciomarine Dwyka beds at Schlip, South West Africa. In: S.H. Haughton (Editor), International Gondwana Symposium 2. Preceding Papers IUGS 2nd Gondwana Symposium (South Africa), Pretoria, pp. 225-232.

Martin, H. and Wilczewsky, N., 1970. Palaeoecology, conditions of deposition and the palaeogeography of the marine Dwyka Beds of South West Africa. In: S.H. Haughton (Editor), International Gondwana Symposium 2 : Trans-Karoo excursion, Pietmaritzburg, pp. 225-232.

Martini, J., E. J., 1974. On the presence of ash beds and volcanic fragments in the greywackes of the Karoo system in the southern Cape Province (South Africa). Trans. Geol. Soc. S. Afr., 77: 113-116.

McLachlan, I.R. and Anderson, A., 1973. A Review of the evidence for marine conditions in Southern Africa during Dwyka times. Palaeontologia Africana, 15: 37-64.

McLachlan, I.R. and Jonker, J.P., 1990. Tuff beds in the north-western part of the Karoo Basin. S. Afr. J. Geol., 93(2): 329-338.

Menning, M., 1997. Geologische Zeitskala der Mark Brandenburg. In: W. Stackebrandt, G. Ehmke and V. Manhenke (Editors), Atlas zur Geologie von Brandenburg. Landesamt für Geologie und Rohstoffe Brandenburg, pp. 74-75.

Menning, M. and Jin, Y.G., 1998. Comment on 'Permo-Triassic magnetostratigraphy in China: the type section near Taiyuan, Shanxi Province, North China' by B. J. J. Embleton, M. W. McElhinny, X. Ma, Z. Zhang and Z. X. Li. Geophys. J. Int., 133: 213-216.

Miller, H., 1981. Pre-Andean orogenies of southern South America in the context of Gondwana. In: M.M. Cresswell and P. Vella (Editors), Gondwana Five. Fith Int. Gondwana Sympos. Balkem, Rotterdam, pp. 237-242.

Miller, R.M., 1992. The stratigraphy of Namibian - Regional Geology Series. Open File Rep. Geol. surv. Namibia, Windhoek, RG 8: 1-34.

Nesbitt, H.W. and Young, G.M., 1982. Early Proterozoic climates and plate motions inferred from major element chemistry of lutites. Nature, 299: 715-717.

Ney, P., 1986. Gesteinsaufbereitung im Labor. Enke Verlag, Stuttgart, 157 pp.

Pearce, J.A., Harris, N.B.W. and Tindle, A.G., 1984. Trace element discrimination diagrams for the tectonic interpretation of granitic rocks. J. Petrol., 25: 956-983.

Pickford, M., 1995. Karoo Supergroup palaeontology of Namibia and brief description of a Thecodont from Omigonde. Palaeont. afr., 32: 51-66.

Ricken, W. and Eder, W., 1991. Diagenetic Modification of Calcareous Beds - an Overview. In: G. Einsele, W. Ricken and A. Seilacher (Editors), Cycles and events in stratigraphy. Springer, Berlin, pp. 430-449.

Ring, U., 1995. Tectonic and lithological constraints on the evolution of the Karoo graben of northern Malawi (East Africa). Geol. Rundschau, 84: 607-625.

Rollinson, H., 1993. Using geochemical data; evaluation, presentation, interpretation. Longman Scientific & Technical. Harlow, United Kingdom, Harlow, 352 pp.

Roser, B.P. and Korsch, R.J., 1986. Determination of tectonic setting of sandstone-mudstone suites using SiO2 content and K2O/Na2O ratio. J. Geol., 94: 635-650.

SACS, S.A.C.f.S., 1980. Stratigraphy of South Africa, Part I (Compiler L. E. Kent). Lithostratigraphy of R.S.A., SWA/Namibia and Rep. of Bophuthatswana, Transkei and Venda. Handbook Geological Survey of South Africa, 8. Government Printer, Pretoria, 690 pp.

Santos, P.R.d., Rocha-Camos, A.C. and Canuto, J.R., 1996. Patterns of late Palaeozoic deglaciation in the Paraná Basin, Brazil. Palaeogeogr., Palaeoclimatol.,Palaeoecol., 125: 165-184.

Schmid, R., 1981. Descriptive nomenclature and classification of pyroclastic deposits and fragments. Geol. Rdschau, 70: 794-799.

Schmid-Röhl, 1999. Hochauflösende geochemische Untersuchungen im Posidonienschiefer (Lias ε) von SW-Deutschland. Tübinger Geowissenschaftliche Arbeiten (TGA), 48(A): 1-189.

Schmincke, H.U. and Bogaard, P.v.d., 1991. Tephra layers and tephra events. In: G. Einsele, W. Ricken and A. Seilacher (Editors), Cycles and events in stratigraphy. Springer Verlag, Berlin, pp. 392-429.

Schönwiese, C., 1985. Praktische Statistik für Meteorologen und Geowissenschaftler. Gebrüder Borntraeger, Berlin, 231 pp.

Schreuder, C.P. and Genis, G., 1974. Die Geologie van die Karasburgse Karookom. Ann. geol. Surv. S. Afr., 10: 7-22.

Schwarzacher, W. and Fischer, A.G., 1982. Limestone-Shale Bedding and Perturbations of the Earth's Orbit. In: G. Einsele and A. Seilacher (Editors), Cyclic and Event Stratification. Springer Verlag, Berlin, pp. 72-95.

Shand, S.J., 1951. Eruptive rocks. John Wiley, New York, 488 pp.

Smith, R.M.H., Eriksson, P.G. and Botha, W.J., 1993. A review of the stratigraphy and sedimentary environments of the Karoo-aged basins of Southern Africa. J. Afr. Earth Sc., 16: 143-169.

Spears, D.A., Kanaris-Sotiriou, R., Riley, N. and Krause, P., 1999. Namurian bentonites in the Pennine Basin, UK - origin and magmatic affinities. Sedimentology, 46(2): 385-401.

Spears, D.A. and Rice, C.M., 1973. An upper Carboniferous limestone of volcanic origin. Sedimentology, 20: 281-294.

Stöffler, D., 1963. Neuere Erkenntnisse in der Tonsteinfrage aufgrund sedimentpetrographischer und geochemischer Untersuchungen im Flöz Wahlschied der Grube Ensdorf (Saar). Beitr. Min. Petrogr., 9: 285-312.

Stollhofen, H., 1999. Karoo Synrift-Sedimentation und ihre tektonische Kontrolle am entstehenden Kontinentalrand Namibias. Z. dt. geol. Ges., 149(4): 519-632.

Stollhofen, H., Stanistreet, I.G., Bangert, B. and Grill, H., 2000. Tuffs, tectonism and glacially related sea-level changes, Carboniferous-Permian, southern Namibia. Palaeogeogr., Palaeoclimatol., Palaeoecol.: in press.

Tera, F. and Wasserburg, G.J., 1972. U-Th-Pb systematics in three Apollo 14 basalts and the problem of initial Pb in lunar rocks. Earth Planet. Sci. Lett., 14: 281-304.

Theron, J.N. and Blignault, H.J., 1975. A model for the sedimentation of the Dwyka glacials in south-western Cape. In: R.S.W. Campbell (Editor), Gondwana Geology. University Press, Canberra, pp. 347-356.

Turner, B., 1999. Tephrostratigraphical development of the Upper Karoo foreland basin: orogenic unloading versus thermally-induced Gondwana rifting. J. Afr. Earth Sc., 28(1): 215-238.

Veevers, J.J., Cole, D.I. and Cowan, E.J., 1994. Southern Africa: Karoo Basin and Cape Fold Belt. In: J.J. Veevers and C.M. Powell (Editors), Permian-Triassic Pangean Basins and Foldbelts Along the Panthalassan Margin of Gondwanaland. Memoir (Geological Society of America). The Geological Society of America, Boulder, pp. 223-279.

Viljoen, J.H.A., 1990. Piroklastiese afsettings van perm V - outerdom in die hoof - Karookom. unpublished PhD Thesis, Univ. Stellenbosch, Stellenbosch, South Africa, 146 pp.

Visser, J.N.J., 1983a. An analysis of the Permo-Carboniferous glaciation in the marine Kalahari Basin, southern Africa. Palaeogeography, Palaeoclimatology, Palaeoecology, 44: 295-315.

Visser, J.N.J., 1983b. Glacial-Marine Sedimentation in the late Palaeozoic Karoo Basin, South Africa. In: B.F. Molnia (Editor), Glacial-Marine Sedimentation. Plenum Press., New York, pp. 667-701.

Visser, J.N.J., 1987. The Palaeogeography of part of southwestern Gondwana during the Permo-Carboniferous Glaciation. Palaeogeog., Palaeocl., Palaeoec., 61: 205-219.

Visser, J.N.J., 1989. The Permo-Carboniferous Dwyka Formation in Southern Africa: Deposition by a predominantly subpolar marine ice sheet. Palaeogeogr., Palaeoclimatol., Palaeoecol., 70: 377-391.

Visser, J.N.J., 1991. Self-destructive collapse of the Permo-Carboniferous marine ice sheet in the Karoo basin: evidence from the southern Karoo. S. Afr. J. Geol., 94: 255-262.

Visser, J.N.J., 1992. Basin Tectonics in southwestern Gondwana during Carboniferous and Permian. In: M.J. de Wit and I.G.D. Ransome (Editors), Inversion Tectonics of the Cape Fold Belt, Karoo and Cretaceous Basins of Southern Africa. Balkema, Rotterdam, pp. 109-116.

Visser, J.N.J., 1997. Deglaciation sequences in the Permo-Carboniferous Karoo and Kalahari basins of Southern Africa; a tool in the analysis of cyclic glaciomarine basin fills. Sedimentology, 44(3): 507-521.

Visser, J.N.J. and Praekelt, H.E., 1996. Subduction, mega-shear systems and Late Palaeozoic basin development in the African segment of Gondwana. Geol. Rdsch., 85: 632-646.

Visser, J.N.J. and Young, G.M., 1990. Major element geochemistry and paleoclimatology of Permo-Carboniferous glacigene Dwyka Formation and postglacial mudrocks in southern Africa. Palaeogeogr., Palaeoclimat., Palaeoecol., 81: 49-57.

von Brunn, B. and Stratten, T., 1981. Late Palaeozoic tillites of the Karoo Basin of South Africa. In: M.J. Humbrey and W.B. Harland (Editors), Earth's pre-Pleistocene glacial record. Cambridge University Press, New York, pp. 71-79.

Wanke, A., Stollhofen, H. and Lorenz, V., 2000. Karoo unconformities in NW-Namibia and their tectonic implications. Henno Martin Special Publication, Comm. Geol. Serv. Nam.: in press.

Weaver, C.E., 1963. Interpretative value of heavy minerals from bentonites. J. Sed. Petrol., 33(2): 343-349.

Wentworth, C.K., 1922. A scale of grade and class terms for clastic sediments. J. Geol., 30: 377-392.

Wetzel, A., 1991. Stratification in Black Shales: Depositional Models and Timing - an Overview. In: G. Einsele, W. Ricken and A. Seilacher (Editors), Cycles and events in stratigraphy. Springer Verlag, Berlin, pp. 508-523.

Williams, I.S. and Cleasson, S., 1987. Isotopic evidence for the Precambrian provenance and Caledonian metamorphism of high grade paragneisses from the Seve Nappes, Scandinavian Caledonides. II. Ion microprobe zircon U-Th-Pb. Contrib. Mineral. Petrol., 97: 205-217.

Winchester, J.A. and Floyd, P.A., 1977. Geochemical discrimination of different magma series and differentiation products using immobile elements. Chem. Geol., 20: 325-343.

Wray, D.S., 1995. Origin of clay-rich beds in Turonian chalks from Lower Saxony, Germany - a rare-earth element study. Chem. Geol., 119: 161-173.

Wray, D.S., 1999. Identification and long-range correlation of bentonites in Turonian - Coniacian (Upper Cretaceous) chalks of northwest Europe. Geol. Mag., 136(4): 361-371.

Zimmerle, W. and Gaida, K.H., 1980. Identification of ancient tuffs and volcanic components in progressively altered ancient agrillaceous sediments; a discussion. In: K.J. Hsue (Editor), International Association of Sedimentologists, first European regional meeting; Abstracts. Int. Assoc. Sedimentol., Bochum, Germany, pp. 251-254.

Figure Index

Table Index

GEOLOGICAL MAP 1 : 25 000 OF THE NAMIBIAN BORDERLAND ALONG THE ORANGE RIVER AT ZWARTBAS

Noordoewer - Warmbad District
Karas Region - Namibia

Heights in metres

1 000 0 1000 2000 metre

MAP LEGEND

Karoo Supergroup

Cretaceous to present day

Kalahari Group and recent deposits

- F — Flood deposits; channel fills
- T — River terraces
- Cac — Calcrete and calcrete-cemented fluvial deposits

Early Permian

Ecca Group

- Ecs — Prince Albert Formation: Shale

Late Carboniferous to early Permian

Dwyka Group

- DwW — White Horizon: White weathering shale
- Dws — Dwyka shale: Shale, partly arenacous; diamictite (dropstones); conglomerate lenses and beds
- Dwt — Basal Yellow or Red Tillite: Diamictite
- Hippo Diamictite
- G — Goats Cliff Diamictite outcrop locality

Nama Group

Late Proterozoic (Vendian)

Schwarzrand Subgroup

- Nco — Nudaus Formation (Vingerbreek Member): Limestone conglomerate and breccia
- Nsc — Nudaus Formation (Niederhagen Member): Quartzitic shale with a diamictitic base and intercalated conglomerate beds

Kuibis Subgroup

- Zal / Zaa — Zaris Formation (Mooifontein Member): Calcisiltite, calcarenite, siltite and silty limestone (Zaa) layered limestone and massive limestone (Zal)
- Zac — Zaris Formation (Kliphoek Member): Red pebbly sandstone and green quartzitic sandstone

Karoo Supergroup

Jurassic / Post-Zaris

Intrusions

- r — Rhyolite dyke
- d — Tandjiesberg Dolerite Complex: Dolerite sill
- q — Quartz vein

- Normal faults: Dotted line: supposed fault; arrow indicates strike-slip direction
- Thrust fault: Dotted line: supposed thrust fault
- Flexure and fold axis (crest / trough)
- Bedding orientation: Long line is strike orientation; small line is dip direction, and angle of dip
- Cross section: Surface line from point A to point B
- # 8 — Locality ID
- Mining Area
- National road, farm road and 4x4 tracks
- Farm buildings and houses
- Cultivated land

Mean magnetic declination 20,7° West of True North

Geographic North / True North

Mapping area

Nama Group

Pre- Gariep and Gariep associated rocks

Karoo Supergroup

Tandjiesberg Dolerite Complex

Dwyka and Ecca Group

Scale 1 : 25 000
Heights are in metres above sea level
contour interval 20 metres
Map source reference:
SOUTH AFRICA 1: 50 000 Sheet 2817 DA NOORDOEWER
Markus Geiger
Institut für Geologie
Universität Würzburg, Germany
1999

NAMIBIA
Warmbad District
Karas Region
RSA
Namaqualand
Northern Cape Province
Tandjieskoppe Mountains
Richtersfeld
Zwartbas
Noordoewer
Orange River

Vertical scale 1:4 000